Stationary and Transient Behaviour of Polymer Electrolyte Fuel Cells

Yan Shi

JÜLICH
Forschungszentrum

Stationary and Transient Behaviour of Polymer Electrolyte Fuel Cells

Yan Shi

Abstract

The Low Temperature Polymer Electrolyte Fuel Cell (LT-PEFC) is a promising alternative power source for automotive applications that offers a relatively simple system level, high efficiency, and completely harmless emissions. Fuel cell operations are complex processes that can be influenced by numerous different operating conditions. This thesis, therefore, focuses on the analysis of the impact of different operating conditions on, both static and dynamic behavior of the LT-PEFC.

An accuracy study is first performed to evaluate the repeatability and reproducibility of the in-house assembled LT-PEFCs employed in the experiments. Four test cells are assembled and tested under the same operating conditions. It is found that the repeatability and reproducibility of the test cells are better when higher stoichiometry ratios and lower current density are applied in the tests. Overall, the LT-PEFCs used in the experiments are characterized by a high level of accuracy.

Various operating parameters are considered in the cell static behavior analysis. With the help of split-plot design, cell orientation, cell temperature, cathodic stoichiometric ratio and backpressure are determined to be the most statistically significant factors for the cell static behavior. Furthermore, the optimal cell performance and corresponding parameter settings are determined via the response surface methodology (RSM).

Voltage overshoot and undershoot behavior are used to characterize the cell dynamic behavior. Using split-plot design, the load change step, cell temperature, cathodic stoichiometric ratio and backpressure are selected as the most significant factors for both the voltage undershoot and overshoot behaviors. Additionally, the effect of load change ramp on voltage undershoot and overshoot is determined. The result suggests that the load change with the ramp can significantly reduce the undershoot and overshoot magnitudes. Moreover, the load change with the ramp has a limited impact on the average pressure drop and the ohmic resistance of the test cell.

Kurzfassung

Die Niedertemperatur-Polymer-Elektrolyt-Brennstoffzelle (NT-PEFC) ist ein vielversprechender alternativer Energiewandler für Automobilanwendungen, die einen hohen Wirkungsgrad, und völlig unbedenkliche Emissionen aufweist. Der Brennstoffzellenbetrieb ist ein komplexer Prozess, der durch zahlreiche unterschiedliche Betriebsbedingungen beeinflusst werden kann. Diese Arbeit konzentriert sich daher auf die Analyse des Einflusses verschiedener Betriebsbedingungen auf das statische und dynamische Verhalten von NT-PEFC.

Zunächst wird eine Genauigkeitsstudie durchgeführt, um die Wiederholbarkeit und Reproduzierbarkeit der in den Experimenten verwendeten hausintern zusammengebauten NT-PEFCs zu bewerten. Vier Testzellen werden zusammengebaut und unter gleichen Betriebsbedingungen getestet . Es zeigt sich, dass Wiederholbarkeit und Reproduzierbarkeit besser sind, wenn in den Tests höhere Stöchiometrieverhältnisse und niedrigere Stromdichten gewählt werden. Insgesamt zeichnen sich die im Test eingesetzten NT-PEFCs durch eine hohe Konsistenz aus.

Bei der Analyse des statischen Verhaltens der Zelle werden verschiedene Betriebsparameter berücksichtigt. Mit Hilfe des Split-Plot Designs werden Zellorientierung, Zelltemperatur, Kathodenstöchiometrie und Gegendruck als die statistisch signifikantesten Parameter für das statische Zellverhalten bestimmt. Darüber hinaus werden die optimale Zellleistung und entsprechende Parametereinstellungen über die Response Surface Methodik (RSM) bestimmt.

Spannungsüber- und -unterschwingverhalten werden verwendet, um das dynamischen Verhalten der NT-PEFC zu charakterisieren. Beim Split-Plot-Designs werden der Laständerungsschritt, die Zelltemperatur, die Kathodenstöchiometrie und der Gegendruck als die wichtigsten Faktoren sowohl für das Spannungsunter- als auch für das überschwingverhalten identifiziert. Außerdem wird die Auswirkung der Laständerungsrampen auf das Spannungsunter- und -überschwingen bestimmt. Das Ergebnis legt nahe, dass die Laständerung mit Rampe das Unter- und Überschwingen deutlich reduzieren kann. Darüber hinaus hat die Laständerung mit Rampe einen begrenzten Einfluss auf den mittleren Druckverlust und den ohmschen Widerstand der Testzelle.

Contents

Contents

Contents

1 Introduction

1.1 Background

Energy, a key technology of human survival and national development, has always been a major concern of the world. Energy supply and demand are directly affected by the world's political and economic development. The consumption rate of energy has risen rapidly due to the rapid advancement of national science and technology, the increasing population, and the increasing demand for daily life. The shortage of energy is now becoming more severe than before [1]. International Energy Agency reported that the world's primary energy total final consumption has increased from 4660Mtoe (megaton of oil equivalent) in the year 1973 to 9938Mtoe in the year 2018 [2]. Figure 1.1 shows the sources shares of primary energy total final consumption in 2018, in which 67% is based on coal (10.0%), oil (40.8%) and natural gas (16.2%). These fossil fuels are non-renewable and with limited resources. The massive use of fossil fuels causes severe environmental issues, including climate change and local pollution in cities, which are seriously threatening the ecosystem and society. In order to overcome the challenges of continuous consumption of non-renewable fossil energy and the challenges of climate change, it is imperative to explore and develop new energy technologies.
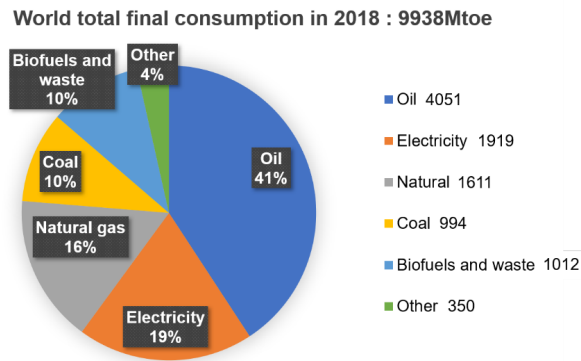
Figure 1.1: Source shares of the world's primary energy total final consumption in 2018. (Redrawn based on the data from [2])

1.1.1 Fuel cell technology

Fuel cell is the device that can electrochemically convert the energy-carrying fuel into electric energy [3], which has attracted significant attention due to its high efficiency and environmentally friendly output [4–6]. The fuel cell's efficiency can achieve around 50%-70% according to different system sizes, which results in a huge development potential to fulfill the requirement of the new energy system today [7–9]. The origin of fuel cells can be traced back to two European scientists, Professor Schönbein and Sir Grove, in the early 19th century. Professor Schönbein, a German-Swiss chemist, proposed fuel cells' underlying principles in 1838 [10]. Later in 1839, Sir William Grove was inspired by water electrolysis experiments, by reversing the water electrolysis process, he invented the world's first fuel cell, called *gas voltaic battery* [11]. However, the lack of mature technology makes fuel cells challenging to enter the practical application field in the next 100 years. In the 1950s, English engineer Bacon developed the porous gas diffusion electrode and also a 5kW alkaline fuel cell stack. Thenceforth the fuel cell technology made significant progress [10]. From 1955 to 1958, through the modification of the electrolyte and the catalyst layer, two chemists Grubb and Niedrach from General Electric Company, developed the prototype of a polymer electrolyte fuel cell (PEFC) [12,13]. Based on their work, in the 1960s, GE developed PEFC technology that was used as the main power source for the spacecraft in the Gemini project [10], which opened the prelude to the practical application of fuel cells.

1.1.2 Fuel cell applications

Fuel cell technologies are primarily implemented in three key areas: portable applications, stationary installations, and transportation [14]. The fuel cells for portable applications are focused on their portability and the convenience of use, such as small auxiliary power units and individual power supply devices. Fuel cells for stationary applications are mainly considered for sustainability and stability to ensure the local power supply, such as combined heat and power system (CHP). Fuel cells for transportation are mainly used for vehicle applications, which include cars, buses and other heavy-duty vehicles. The share of the total capacity of these three application fields over the last ten years (2010-2019) is illustrated in Figure 1.2. It can be observed that the fuel cell's stationary applications were dominated from 2010 to 2015, which is due to the fact that the CHP system has a considerable increase in installed capacity in Japan (Ene-Farm project [15]), North America (SGIP project [15]), and South Korea (large scale stationary fuel cells [16]) for a long time. In 2016, the applications of fuel cells in the transportation field surpassed the stationary field for the first time. Toyota

Mirai and Hyundai NEXO together account for a major part of the fuel cell vehicle market. With the addition of fuel cell buses and trucks, fuel cell for transportation applications has gradually become dominant since 2016.

Megawatts by application 2010-2019

	2010	2011	2012	2013	2014	2015	2016	2017	2018	2019
Portable	0.4	0.4	0.5	0.3	0.4	0.9	0.3	0.6	0.7	0.6
Stationary	35	81.4	124.9	186.9	147.8	183.6	209	222.3	220.6	221.2
Transport	55.8	27.6	41.3	28.1	37.2	113.6	307.2	435.7	584.5	907.8
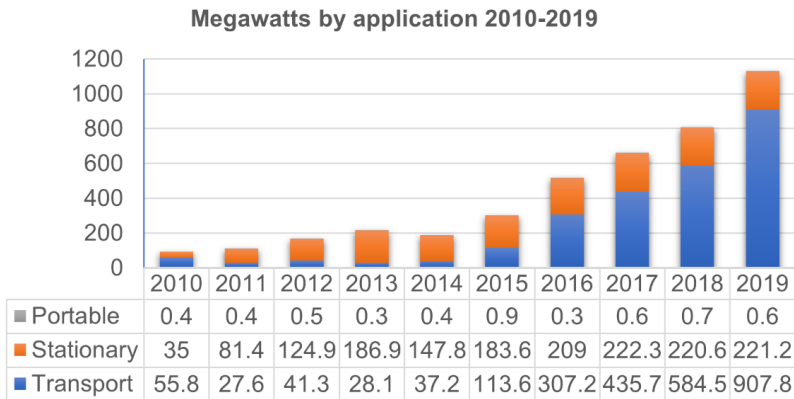
Figure 1.2: Megawatts of installed fuel cell power by application 2010-2019 (Redraw based on the data from [16,17]).

1.1.3 Fuel cell types

The basic structure of a fuel cell (single cell) includes an anode electrode, a cathode electrode, and an electrolyte between them. According to the different types of electrolytes and working temperature, fuel cells can be classified into six major types, which are Alkaline fuel cell (AFC), Low-temperature polymer electrolyte membrane fuel cell (PEFC), Phosphoric acid fuel cell (PAFC), Molten carbonate fuel cell (MCFC), Solid oxide fuel cell (SOFC), and Direct methanol fuel cell (DMFC) [18]. The comparison of the different types of fuel cells with their properties is illustrated in Table 1.1. It can be found that almost all fuel cells can use hydrogen or hydrocarbons as fuel. Hydrogen or hydrocarbons can be extracted using water electrolysis, natural gas reforming, petroleum cracking, crop fermentation, and many other methods. In today's energy scarcity situation, this diversified fuel acquisition method is one of the huge advantages of fuel cells. At present, hydrogen energy-related industries are gradually developing, and scientists worldwide are stepping up their work to prepare for the hydrogen energy era.

1 Introduction

Table 1.1: Comparison of fuel cells

Type	Electrolyte	Fuel	Working Temperature	Electrical Efficiency	Applications
Alkaline (AFC)	Potassium hydroxide (KOH)	H_2	60-220°C [19]	~50% [19]	Portable (Military, Space)
Direct Methanol (DMFC)	Polymer membrane (ionomer)	Methanol	Ambient-110°C [9]	35-60% [9]	Portable
Polymer Electrolyte Membrane (PEFC)	Polymer membrane (ionomer)	H_2 Reformate	60-80°C (Nafion) [20] 110-180°C (PBI) [9]	40-60% [9] 35-40% [21]	Transport Stationary
Phosphoric Acid (PAFC)	Molten phosphoric acid (H_3PO_4)	H_2	160-200°C [9]	36-45% [9]	Stationary
Molten Carbonate (MCFC)	Molten alkaline carbonate	Natural gas, Biogas	~650°C [19]	45-55% [19]	Stationary
Solid Oxide (SOFC)	Y_2O_3-stabilized ZrO_2 (YSZ)	Natural gas, Biogas	800-1000°C [9]	55-65% [9]	Stationary

Figure 1.3 illustrates the share of the total capacity by different fuel cell types over the last ten years (2010-2019). It can be observed that the capacity of PEFC has increased significantly, and it gradually dominates from the year 2015, which is due to the rapid development of commercial and passenger vehicles (notably Toyota and Hyundai) in the transportation field. PAFC and SOFC are the other two major fuel cells, which are mainly applied in CHP systems. The capacity of the MCFC has declined in recent years. The capacities of AFC and DMFC are so small that they are not visible in the figure.

Megawatts by fuel cell type 2010-2019

	2010	2011	2012	2013	2014	2015	2016	2017	2018	2019
■ AFC	0.1	0.1	0	0.3	0	0.2	0.5	0.6	0.1	0
■ MCFC	7.7	44.5	62	91.9	70.5	68.6	55.7	24.7	25.8	10.2
■ SOFC	6.7	10.6	26.9	47	38.2	53.3	62.9	85.2	84.1	78.1
■ PAFC	7.9	4.6	9.2	7.9	3.8	24	56.2	81	86.3	106.7
■ DMFC	1.1	0.4	0.3	0.2	0.2	0.2	0.2	0.3	0.4	0.4
■ PEFC	67.7	49.2	68.3	68	72.7	151.8	341	466.7	609	934.2
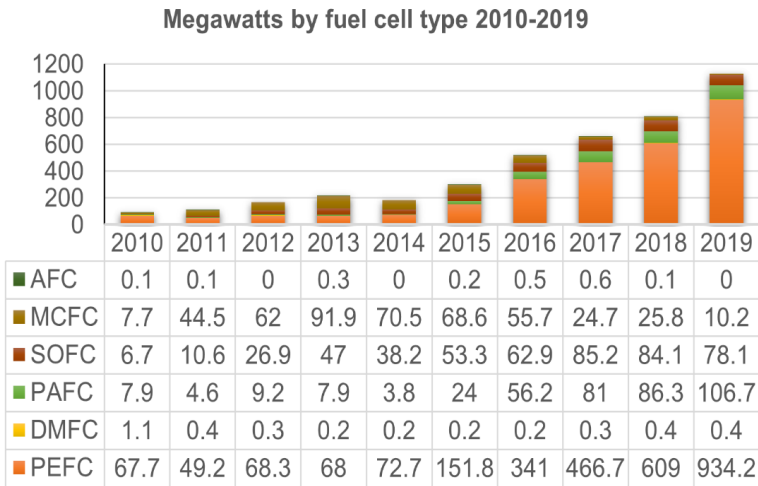
Figure 1.3: Megawatts of installed fuel cell power by fuel cell type 2010-2019 (redrawn based on the data from [16,17]).

1.2 PEM fuel cell

1.2.1 Fundamentals

Polymer electrolyte fuel cells (PEFCs), among many different fuel cell types, are regarded as promising power sources for automotive applications because they are characterized by relatively low operating temperatures, high efficiency, high power density, quick start-up times, and 100 percent environmentally friendly output [22]. Figure 1.4 illustrates the basic working principle of a PEFC during its operation process. The electrochemical reactions are taking place at the interface between porous carbon support, Pt catalyst particles and the proton exchange membrane (PEM), namely the triple phase boundary (TPB). The humidified hydrogen, which is fed at the anode side, is oxidized electrochemically and the protons (H^+) and electrons (e^-) are released during this process. The protons flow through PEM with several water molecules to the cathode side. At the same time, the electrons transfer to the cathode side through the external load. The reaction process at the anode side is the so-called hydrogen oxidation reaction, which can be expressed by the equation:

$$H_2 \rightarrow 2H^+ + 2e^-$$
1.1

The supplied air (oxygen) is reduced electrochemically with the transferred protons and electrons at the cathode side. Water and heat are generated during this process. Both of them should be released out to ensure a proper working environment of the fuel cell. The reaction process at the cathode side is the so-called oxygen reduction reaction, which can be expressed by the equation:

$$1/2O_2 + 2e^- + 2H^+ \rightarrow H_2O \qquad\qquad 1.2$$

The overall reaction, namely the Redox reaction, can be expressed by [23]:

$$H_2 + 1/2O_2 \rightarrow H_2O + Heat \qquad\qquad 1.3$$
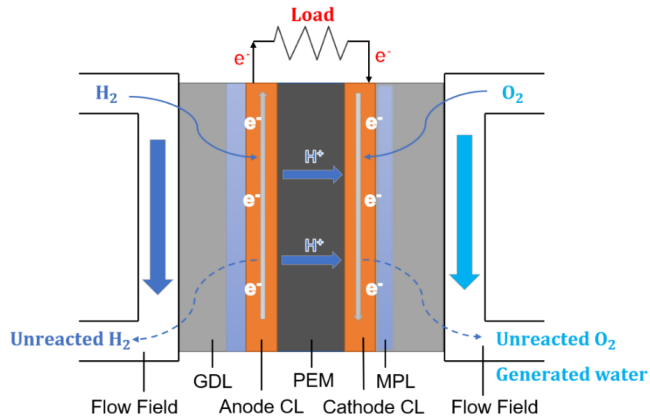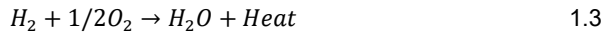
Figure 1.4: The basic working principle of a PEFC.

Thermodynamically, if all heat or enthalpy of the reaction could be converted into electrical energy, the fuel cell potential would be calculated by the following equations [19]:

$$E = \frac{-\Delta h_f^{\,0}}{nF} \qquad\qquad 1.4$$

$$\Delta h_f^{\,0} = \Delta h_{f,H_2O}^{\,0} - \Delta h_{f,H_2}^{\,0} - 1/2\Delta h_{f,O_2}^{\,0} \qquad\qquad 1.5$$

Where:

$\Delta h_f{}^0$ = change in enthalpy of the reaction (kJ mol⁻¹) under STP,

n = moles of transferred electrons, here equal to 2, and

F = Faraday's constant, 96485C mol⁻¹.

At the standard temperature and pressure condition (STP) (298.15 K and 1atm), when water vapor is produced, the value of $\Delta h_f{}^0$ is equal to -241.98 kJ mol⁻¹, namely lower heating value (LHV) of hydrogen; the value of $\Delta h_f{}^0$ related to liquid water production is equal to -286.02 kJ mol⁻¹, namely lower heating value (LHV) of hydrogen. The cell potential is then calculated to be 1.482 V (HHV), or 1.254 V (LHV). However, entropy is produced during each chemical reaction resulting in only part of the reaction enthalpy, which is called Gibbs free energy, can be converted into electric energy. Thus, the theoretical cell potential can be given by the following equations [19]:

$$E_0 = \frac{-\Delta g_f{}^0}{2F} \qquad\qquad 1.6$$

$$\Delta g_f{}^0 = \Delta h_f{}^0 - T\Delta s^0 \qquad\qquad 1.7$$

Where:

E_0 = theoretical cell potential (V),

$\Delta g_f{}^0$ = change in Gibbs free energy of the reaction (kJ mol⁻¹) under STP,

Δs^0 = change in entropy of the reaction (kJ mol⁻¹K⁻¹) under STP,

T = reaction temperature (K),

$\Delta g_f{}^0$ is equal to -228.74 kJ mol⁻¹ (LHV) or -237.34 kJ mol⁻¹ (HHV). Correspondingly, the cell potential is then calculated to be 1.185 V (LHV) or 1.230 V (HHV). However, PEFCs are rarely operated under STP conditions. The fuel cell potential at a given pressure and temperature can be displayed by Nernst Equation [19]:

$$E = E^0 - \frac{RT}{2F}\ln\frac{a_{H_2O}}{a_{H_2}a_{O_2}^{0.5}} \qquad\qquad 1.8$$

Where:

E = Nernst fuel cell potential (V),

R = universal gas constant (8.314 J mol⁻¹K⁻¹),

T =   reaction temperature (K),

a_i =   activity of each reactant or product, which is defined as $a_i = \frac{P_i}{P^0}$, where P_i is the partial pressure of each reactant or product (kPa), P^0 is atmospheric pressure (101.325 kPa). When the product water is in the liquid phase, the a_{H_2O} is set to 1.

In practice, the actual fuel cell potential is lower than the Nernst potential due to a number of irreversible losses. These losses can be identified in the plot of the polarization curve. A polarization curve or *i*-V curve depicts the relationship between the voltage and current at the steady-state condition, which is widely used to evaluate the fuel cell [24]. Figure 1.5 illustrates a typical polarization curve and four types of losses: gas crossover losses, ohmic losses, mass transport losses, and activation losses. Each of them is dominated at corresponding current densities.
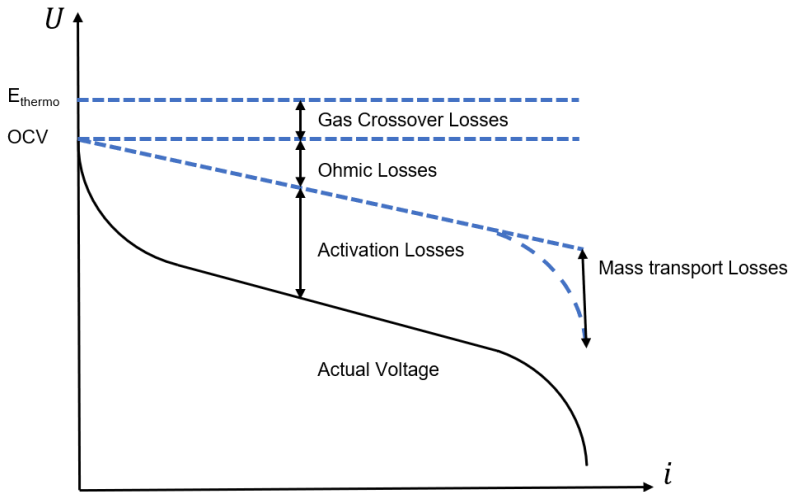
Figure 1.5: The typical polarization curve indicated with main voltage losses.

Gas crossover losses are mainly caused by the hydrogen molecules diffusion from the anode side to the cathode side. At the same time, a small number of electrons are directly transferred through the electrolyte membrane resulting in the internal short-circuit current. Both, the gas crossover and internal short-circuit current lead to a decrease in the open-circuit voltage (OCV) [25,26]. Activation losses are dominant at the low current densities area. The cell voltage decreases rapidly with the increase of the current density, which is caused by the higher charge transfer resistance during

the oxygen reduction reaction process at the fuel cell cathode side. Ohmic losses are dominant at the intermediate current densities area, mainly caused by the resistances of protons transferring through the electrolyte membrane and electrons pass through the cell components and their contact surfaces. The polarization curve shows linearity in this area. Mass transport losses are encountered at the high current densities area. The diffusion of the reactants to the reaction site is slower than the electrochemical reaction speed, resulting in a decrease of the local reactants concentration and the decrease of the cell voltage.

1.2.2   Critical technical barriers for fuel cell commercialization

PEFCs have huge market potential as a power source for automotive applications. However, there are still some technical barriers, such as cost and durability, that need to be overcome before full commercialization [27]. The costs (100,000 units per year) of the fuel cell system in 2020 are about $50/kW, which has decreased by 35% compared to 2010 [28]. It still needs a 40% reduction to meet the ultimate target of $30/kW. The durability of the fuel cell system for the light-duty automotive application in 2020 is about 4130 h, which still needs a 94% increment to meet the ultimate target of 8,000h. Compared to 20,000h for commercial vehicles such as buses or heavy-duty trucks [29] and 40,000 h for stationary applications [30], the durability target of 8,000 h for automotive applications is relatively short. However, the severe operating conditions such as frequent start and stop, cold start-up, and dynamic load cycling make it a great challenge to achieve this goal. To increase the fuel cell performance, stability and durability, one effective way is to optimize the fuel cell operating conditions, which are related to the water management of the fuel cell [31].

1.3   Water management of PEFCs

Water management issues are one of the key limiting factors and extremely vital to PEFC commercialization. A proper water management strategy can help the fuel cell to achieve a high-performance level and long durability. The amount of liquid water should be maintained in PEM to ensure good ionic conductivity and thus a good performance. However, excessive liquid water will cause flooding at electrodes, GDLs and flow fields, which will negatively influence fuel cell's performance and durability. A subtle water balance should be maintained during a fuel cell operation. The water transport mechanisms, water fault diagnosis method and state-of-art water management studies are reviewed in this section.

1.3.1 Water transport mechanism

The water transport mechanism in a typical PEFC is shown in Figure 1.6. The humidified reactants are fed into the fuel cell. At the anode side, protons are migrating in the form of H_3O^+ and associated with the mobility of one or more water molecules to the cathode side under the electro-motive forces, this transport process is called 'Electro-osmotic drag (EOD)' [32,33]. At the cathode side, the water carried by the humidified air and also that generated by the oxygen reduction reaction process is resulting in a water accumulation. Hence a water concentration gradient across the PEM will force the water at the cathode to diffuse to the anode side. This process is called 'Back diffusion (BD)' [34]. The temperature gradient in the direction perpendicular to the PEM also can drive the water from the cathode to the anode side, this process is called 'thermal-osmotic drag (TOD)' [35].
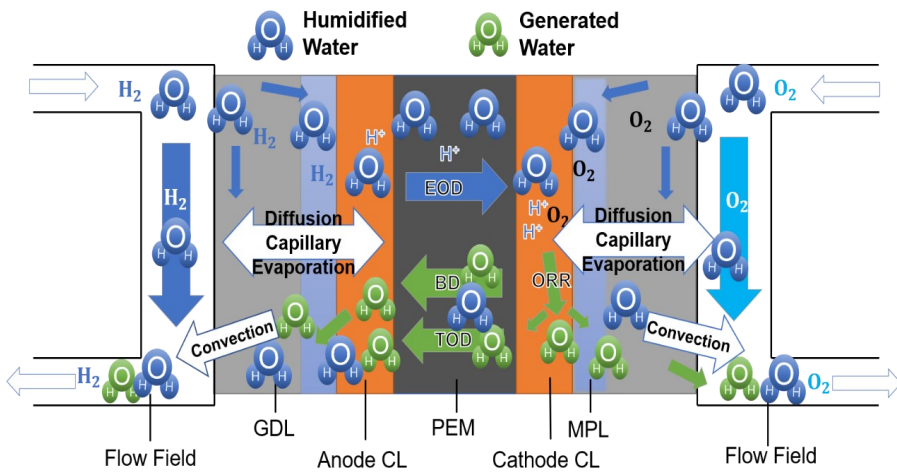
Figure 1.6: Water transport mechanisms in PEFC.

Apart from the water movement across the membrane that is driven by EOD, BD and TOD, the excessive water in the catalyst layer is also transferred through the microporous layer (MPL) and gas diffusion layer (GDL) via capillary motion, water evaporation, diffusion and convection [36,37]. The capillary motion refers to the movement of liquid water and gas that is driven by the pressure in small pores. This pressure is also known as capillary pressure, which is essentially influenced by surface tension and the wettability of the pore structure. Diffusion refers to the movement of species being driven by concentration gradients. Convection refers to the movement of species being driven by pressure gradients.

The capillary pressure is dominant in the MPL because it has a smaller pore size than the GDL [38]. According to the descriptions of Jiao and Li [37], the main driving forces in the GDL are strongly dependent on the flow field structure, which can be dominated by diffusion (parallel flow field design), or convection (interdigitated flow field design), or mixing of two forces (serpentine flow field design), as shown in Figure 1.7.
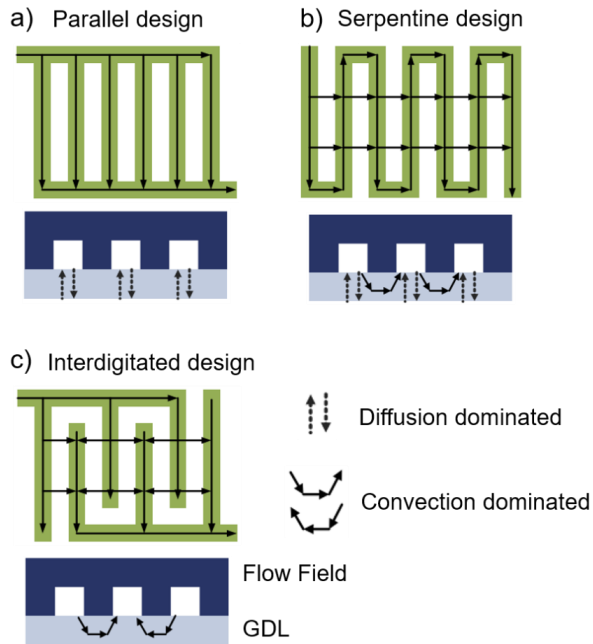
Figure 1.7: The main driving forces in GDL with different flow fields: a) Parallel design, b) Serpentine design, and c) Interdigitated design. (Redrawn based on [37], Copyright License Number: 4991631194278)

For the GDLs fabricated by carbon paper, the generated water is transported in a series of small capillaries from the catalyst layer (CL) and then merged into a large capillary and finally reach the flow channel [39]. As shown in Figure 1.8, it can be observed that water is transported in the way of 'fingering'. When these fingers are breaking through to the flow channels, the water transport process in the adjacent finger may recede, resulting in 'dead ends' [40]. The liquid water is preferably accumulated under the flow field ribs rather than flow channels [41]. Eventually, the cumulated water erupts into the flow channel and then is flushed out by gas flow.
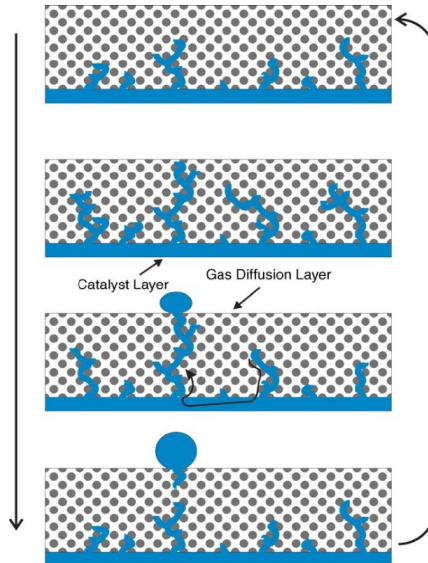
Figure 1.8: Schematic of the water transport mechanism in non-woven GDL [40]. (Copyright License Number: 4983210520614)

1.3.2 Water fault issues in PEFCs

The impropriate water management in PEFCs can lead to water fault issues, which can be classified into two cases: membrane drying and liquid water flooding. A long-term operation of PEFCs under the water fault situation could lead to a severe performance decrease and may also cause irreversible damage to fuel cell components.

1.3.2.1 Membrane drying issue

Membrane drying could lead to a decrease of ionic conductivity and an increase of the ohmic resistance of the membrane, resulting in substantial losses of the output power [42]. The drying area on the membrane will be enlarged progressively when the fuel cell was operated under dehydration conditions. Sanchez and Garcia-Ybarra [43] experimentally investigated the membrane dehydration behavior of a single fuel cell under zero external humidification conditions. The fuel cell has a 25cm^2 active area and is connected with serpentine flow fields on both sides. They found that membrane dehydration begins at the inlet port of the cathode side. A drying transition boundary was observed, which separates the membrane into two zones - wet zone and dry zone. The dry zone was enlarged with the propagation of the drying transition boundary along the membrane, resulting in a decrease in the cell potential. The voltage drop that is caused by the membrane drying issue in a short period of time can usually be restored

by humidification. However, if the fuel cell is operated under severe drying conditions over a long time, the membrane will become more brittle and thus some irreversible mechanical failures, such as pinholes and cracks, may be developed on the membrane. Then, the voltage drop is unlikely to be restored under this condition [29].

1.3.2.2 Liquid water flooding issue

Water production rate exceeding the water removal rate during the fuel cell operations can lead to excess water accumulation. The resulting liquid water flooding can occur in the CLs, GDLs, and flow channels on both the anode and cathode sides [44]. Hussaini and Wang [45] illustrated the formation and distribution of liquid water in the flow channel (see Figure 1.9). At the beginning of a fuel cell operation, only stray droplets exist on the surface of the GDL. As the fuel cell continued to operate, more water droplets are emerged and remained on the surface of the GDL by surface tension forces. The flow pattern is shifted from single-phase flow to droplet flow. As time passed, more water is produced and transported through the GDL to the flow channel. More stable droplets are emerging with each other and attached to the channel walls. A liquid water film is then generated. In the phase of film flow, the airflow stream will continuously sweep the water droplets before coalescing into the liquid film. As more water is produced and the liquid film grows, a water slug appears in the channel. The film flow is shifted to the slug flow. At this stage, big water slug blocks the flow channel and flooding occurs. These four types of flow patterns were then supported by Song et al. [46] with their flooding experiments at anode flow channel. The blocking of reactants transport passages results in an increase of the mass transport loss, and thus a decrease in the cell performance. Increased local pressure caused by the blocked pathways can help to flush out the excess water and thereby restore the cell performance. However, a severe flooding issue causes unstable output power and leads to the degradation of the CLs and the corrosion of the GDLs due to local gas starvation, which dramatically influences the durability of the fuel cell [47].
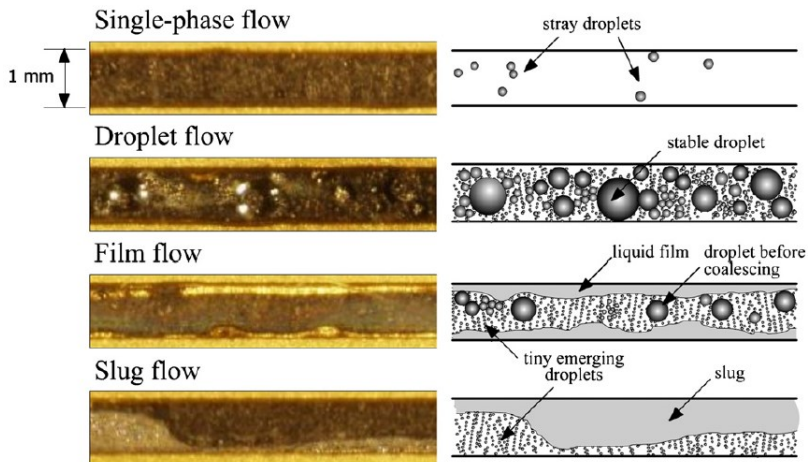
Figure 1.9: Demonstration of the formation and the distribution of liquid water in the flow channel [45]. (Copyright License Number: 4999451259345).

1.3.3 Experimental diagnostic methods for the water faults

Parameters that are influenced by the water state inside the fuel cell can be applied to diagnose water faults. Monitoring the cell voltage is widely used for fuel cell performance characterization. The water fault issues can lead to losses of the cell voltage. However, it is difficult to distinguish between liquid water flooding and membrane drying, clearly based on the analysis of the cell voltage. Besides the cell voltage, some properties of a fuel cell also can be influenced by flooding and drying issues. For example, water scarcity can lead to an increase in membrane resistance; or too much accumulation of water in the GDL and flow channel will cause an increase in the gas flow resistance and thus a rise of the pressure drop between the inlet and outlet of the fuel cell. Therefore, measuring these physical indicators can be used as an effective method to diagnose water faults [44].

High Frequency Resistance (HFR) is mainly referring to the ohmic resistance of the membrane, and the ohmic resistance is significantly increased when the membrane is in a state of dehydration. Hence, the HFR is widely used for indicating the membrane drying issue [37]. Liu et al. [48] investigated the voltage and HFR response on a single cell with different current densities and stoichiometric ratios. They found the optimum stoichiometric ratio at the cathode side and also concluded that the drying and flooding issue could exist simultaneously on the membrane at different locations. General Motors [49] obtained the optimum relative humidity level through the monitoring of the

HFR. However, for the water flooding issue, the HFR is not an effective tool for perceiving [50]. Ren et al. [51] applied the HFR to detecting the membrane dehydration state and Low-frequency resistance (LFR) to monitor the water flooding. The optimum frequency of the LFR is around 0.57 Hz. Although the LFR can be used to detect cell flooding, the frequency should be carefully selected, which decreases the flooding detecting efficiency and is hard to apply for the online diagnosis.

Pressure drop between the inlet and outlet port on both the anode and cathode side increases with the accumulation of liquid water in the flow channels, and it decreases rapidly with the flush out of the excess water content [52]. He et al. [53] experimentally investigated the correlation of the cell performance and water flooding level under various operating conditions. The pressure drop at the cathode side was applied as a diagnostic tool to reflect the flooding level. They concluded that pressure drop could provide real-time flooding information during the cell operation, and also confirmed that cell temperature and air flow rate play a significant role in liquid water removal. Jiao et al. [54] studied the effects of the thickness of the GDLs and the flow rate of gas on liquid water removal on a fuel cell with serpentine flow fields. A time-dependent pressure drop was applied to characterize the water removal rate. They conclude that water removal rates in GDL are highly influenced by the GDL thickness and gas flow rate. When the gas flow rate is low, the water removal rate is the lowest for a lower GDL thickness due to the small permeability. When the gas flow rate is high, the time for water removal is greatly reduced at different GDL thicknesses. A higher gas flow rate is preferable for water removal. In general, pressure drop has the advantages of being reliable, easy to perform and can be used for online diagnosis, making it a good indicator for water flooding detection [55]. However, the pressure drop cannot perceive the membrane drying out situation, which is because the pressure drop remains almost constant in drying conditions [55,56]. Barbir et al. [57] applied both the HFR and pressure drop jointly to detect the water state in a three-cell stack. They concluded that the drying and flooding issues could be relieved by adjusting the temperature and the humidification levels.

1.4   The studies on water management

Generally speaking, proper water management strategies can be grouped into two types: during-design and post-design strategies.

1.4.1 During-design water management strategies

The during-design strategies are mainly referred to achieve the proper water balance and hence better cell performance by designing the new flow field structures and applying new materials to PEMs and GDLs.

PEM, acting as a separation between the anode and the cathode side, can transfer protons, insulate electrons and reactants to transfer from one side to another. Good PEM should be characterized by strong proton conductivity, good mechanical properties, and high electrochemical stability. Dang et al. [58] proposed a porous Nafion membrane (P-Nafion), in which the porous layer is located on the cathode side, and its thickness is approximately 3-5µm. This P-Nafion can enhance the water back diffusion process, which is beneficial to the fuel cell's self-humidification and can also help reduce the risk of delamination issues between the PEM and catalyst layer.

Freire and Gonzalez [59] quantitatively investigated the effects of the membrane thickness and temperature variability on cell performance. The results indicated that thinner membranes and higher temperatures were associated with improved cell performance. In addition to the normal PEMs, self-humidifying PEMs are also investigated by many researchers [60]. Some additional additives such as hygroscopic metal oxides [61] and heteropolyacids [62] are added to the membrane to increase the water retention capability and the proton conductivity so that the cell can maintain an adequate performance with the dry or less-humidified reactants.

The GDL in PEFC has functions such as CL support, reactant transmission, water drainage, etc., especially playing a significant role in water management. It is generally composed of a gas diffusion medium (GDM) with large pores and a microporous layer (MPL) with small pores. The porosity of the GDL can effectively influence the water and gas permeability and also electrical conductivity. Mo et al. [63] reported a GDL with the gradient design for the porosity. This type of GDL has a higher water retention capacity and can effectively increase the cell performance under dry conditions (RH 12.66% at 65°C). Kandlikar et al. [64] studied the influence of the MPL on water transport across the GDLs. The results revealed that the MPL could limit the water breakthrough location from the GDL to the channels, which coincides with the findings from Spernjak et al. [65]. Shi et al. [66] experimentally estimated that both the optimum PTFE loading and the thickness of the MPL are 35 wt% and 90 µm, respectively. With

this MPL, the cell performance was improved at the dry condition, and the cell stability was also enhanced at the well-hydrated condition.

Besides the GDLs and PEMs, adequate flow field design is considered as the most successful strategy for water management issues [67,68]. Yan et al. [69] experimentally investigated the effects of two types of flow fields: conventional type (parallel, Z-type and serpentine) and interdigitated type (parallel-baffle and Z-type-baffle) with different operating conditions. The results suggest that the interdigitated flow fields have the advantage of lower fuel consumption rates at the same fuel cell performance level. Heidary et al. [70] configured the blockage in the parallel flow channels. Compared to the case without any blockage, the cell performance was increased by 18% when the in-line-blockage was implemented and was increased by 28% with the staggered-blockage. Jo et al. [71] numerically studied the metal foam flow field under low-humidity operating conditions. The results show that using highly porous metal foam can help to enhance the distribution uniformity of the current density. Lim et al. [72] numerically studied the impact of the 3D flow field, serpentine flow field and metal foam flow field on cell performance. They concluded that the 3D flow field is superior to the other two flow fields regarding water removal capacity and current density distribution uniformity.

1.4.2 Post-design water management strategies

The post-design strategies are mainly concerned with adjusting and modifying the operating conditions to achieve the proper water balance and thus improve cell performance. It is a promising water management strategy and is also widely used in laboratory and industry areas [73]. Various parameters are included in the typical operating conditions, namely stoichiometric ratio, relative humidity, operating pressure, and operating temperature of the fuel cell. Manipulation of these factors can effectively affect fuel cell performance, for example:

(1) Increasing the stoichiometric ratio of the reactant gas, especially on the cathode side, can effectively improve the performance of the fuel cell owing to the higher rate of gas flow resulting in a higher concentration of the reactant at the active site, and can also improve the ability to remove liquid water out of the cell [31,74–76]. Natarajan and Nguyen [77] experimentally investigated the effect of the cathodic gas (oxygen) flow rate on the performance of a single cell with one straight channel. They observed that reducing the cathode flow rate will result in an uneven current density distribution along the flow channel. The flooding area was observed close to the outlet part. By contrast,

increasing the gas flow rate can delay the flooding event time to almost 25 minutes. However, it will also result in decreased current density near the inlet area. The higher flow rate also has a higher dehydration effect, which drying the membrane at the inlet part and thus increases the internal resistance of the membrane. Migliardini et al. [78] utilized the strategies of hydrogen purge with specific frequencies and increasing the air flow rate to maintain a good cell performance.

(2) Appropriate relative humidity can keep the membrane in a high hydration state and contribute to water balance between the anode and the cathode side. Increasing the relative humidity of the reactant gas can improve the membrane's hydration level, which can ensure a lower ohmic resistance [79]. Natarajan et al. [77] found that increasing the relative humidity on the anode side can cause a decrease in the current density distribution homogeneity. Increased relative humidity introduces more water to the anode side, lowering the water gradient between the anode and cathode side, thereby reducing the water back diffusion rate. Then, the cathode water removal rate will decrease and consequently lead to a decrease in the current density distribution homogeneity. Yan et al. [80] investigated the influence of both anode and cathode side relative humidity on cell performance. They revealed that compared to the anode side, the cathodic relative humidity is more sensitive to cell performance at lower values.

(3) Increasing the operating temperature can help to improve the performance of the fuel cell. A higher temperature can lead to a higher electrochemical reaction rate during the fuel cell operation[81] and lead to a higher diffusion speed of reactants to the catalyst site and the discharge speed of the generated water [82]. He et al. [53] proved that a rapid temperature increase from 40°C to 50°C could alleviate the flooding in the test cell. Barbir et al. [57] proposed a similar method that increases the temperature can decrease the voltage fluctuation when flooding occurs, and also decrease the cathodic pressure drop. However, an extreme temperature (exceeding 80°C) will have a negative effect on the fuel cell performance, owning to that it will make the membrane at a dehydrated state, and cracks will be generated in the membrane at some extreme conditions [4].

(4) Increasing the operating pressure can help to improve the performance of the fuel cell. Increased operating pressure can improve the partial pressure of the reactants and facilitate the diffusion of the reactants to the catalyst layer, thereby reducing mass transport resistance. It was also found that adjusting the pressure on the anode side at lower values than on the cathode side can help to increase the test cell performance,

owning to the fact that the generated pressure gradient will enhance the water back diffusion from the cathode side to the anode side [83]. The same method was also applied by Mughal and Li [84] in their later works. However, the operating pressure at the two sides was normally set to equal values, which can not only reduce reactants crossover but also decrease the risk of membrane failure.

(5) In addition to these normal operating parameters, the fuel cell's orientation can also affect water management to some extent, especially when the fuel cell is used for transport applications. Kimball et al. [85] performed the experiment on a single-channel fuel cell to investigate the effect of cell orientations on liquid water motion. They conclude that the flooding issue in PEFC is gravity-dependent and the motion of the water slug is strongly influenced by the flow channel orientations. Chen and Wu [86] experimentally investigated the effect of the cell position on the discharge of the liquid water within a PEFC. They conclude that the cell position of the anode-upward is beneficial for the liquid water discharge compared to the position of the cathode-upward. Guo et al. [87] investigated the impact of flow channel orientations on cell performance under terrestrial gravity conditions, and also employed the experiments under microgravity conditions to simulate the PEFC for space applications. They found that liquid water flooding is prone to occur by vertical orientation compared to the horizontal orientation of flow channels. When gravity was shifted from terrestrial gravity to microgravity, the flooding issue in the vertical flow channel is alleviated. However, for the horizontal flow channel, the liquid water is hard to be removed under the microgravity condition due to the increased surface tension of the water droplets. Ashrafi and Shams [88] numerically investigated the effects of gas flow direction and cell orientation on the two-phase flow in the fuel cell, which were characterized by the water coverage ratios and pressure drop. The result shows that the lowest pressure drop was observed when the cell was positioned vertically, the flow channel was positioned horizontally, and the inlet port was in the top area. The highest pressure drop was observed when both the cell and flow channel were positioned vertically, and the inlet port was in the bottom area. The highest water coverage ratio on the GDL surface was observed when the cell was positioned horizontally and the cathode side was above the anode side. This is undesirable for proper water management in the cell.

1.5   Transient behavior study of PEFCs

Most of the studies reviewed in the last section mainly focus on the steady-state performance of the PEFC single cell or stack at different operating conditions and different modified fuel cell components, such as newly designed flow field structures or GDL materials. However, regarding the utilization of the PEFC systems in real life, especially for transport applications that include a large number of load variable conditions, the fuel cell should be capable of fast response during the start-up, stop, acceleration processes. Furthermore, sudden load change will also increase the difficulty of water management inside the fuel cell, which can eventually lead to a huge influence on cell performance and durability. Thus, thorough research on the PEFC transient response is essential. (Part of this section has been published in [89])

Um et al. [90] proposed a transient model that takes the electrochemical reaction kinetics, multi-substance transport, and current density distributions into consideration. The current overshoot behavior was observed with the change of the voltage from 0.6 V to 0.55 V. This is because mass transport rate is much slower than electrochemical reaction rate, which the concentration of the reactant gas on reaction sites needs to take more time to reach equilibrium. This leads to transient behavior. Yan et al. [91] numerically analyzed the effects of flow channel width and catalyst layer overpotential on the mass transport transient behavior. The results showed that a higher value of the channel width and catalyst layer overpotential might cause a faster dynamic response behavior during the start-up phase.

Hamelin et al. [92] experimentally studied the Ballard Mk5-E fuel cells' transient behavior and observed rapid voltage transient behavior, which was determined to be overshoot and undershoot behavior. Kim et al. [93] experimentally studied the effects of voltage change and stoichiometric ratio on the current density overshoot and undershoot behavior of a PEFC with a 25 cm² triple serpentine flow field. The results showed that an increase in the stoichiometric ratio causes a decrease in current overshoot amplitude. It proved the experimental results from Hamelin et al. [92] and the numerical simulation results from Um et al. [90]. Shen et al. [94] investigated the effect of an air stoichiometric ratio on voltage undershoot behavior and found that increasing the stoichiometric ratio will reduce the voltage undershoot tendency. This is because an increased stoichiometric ratio leads to reduced water accumulation in the gas diffusion layer and the flow channel, which consequently increases the reactant concentration on the reaction site and improves the reactant distribution.

Yan et al. [95] experimentally studied the transient behavior of single cell during cyclic load changes and different operating conditions, including inlet gas temperature, operating temperature, stoichiometric ratio and inlet gas pressure. They found that a higher cathodic reactant humidity causes a lower voltage undershoot amplitude. Also, a higher stoichiometric ratio and higher pressure could reduce the transient behavior of the cell. Liu and Case [96] investigated the long-term durability of PEFCs under different current cycles to simulate the real driving conditions for vehicular applications. Cell polarization curves, electrochemical impedance spectra, as well as hydrogen crossover rates were used to characterize the MEAs. They found that the hydrogen crossover rate was kept nearly stable during the constant current operation. However, under cyclic current conditions, a pinhole was formed on the MEA after 500 h of operation, which led to dramatically increased hydrogen crossover. Lin et al. [97] investigated the degradation of PEFC performance under cyclic load operating conditions. It was noticed that after 280 hours of operation, the cell performance starts to decrease. Furthermore, the gaps and cracks were formed on the catalyst layer after 370 hours of operation. In their later work [98], Lin et al. studied the influences of dynamic load changes on the durability of a segmented cell. Their results showed that the performance of the cell decreased dramatically after 200 cycles of operation. Moreover, the current density decreased much faster at the inlet and outlet region than in other positions. By analyzing the impedance spectroscopy, they found that the ohmic resistance increases after 200 cycles, especially on the cathode side.

Banerjee and Kandlikar [99] confirmed that apart from the electrochemical transients, the PEFCs' transient behavior also includes the thermal and two-phase flow transients. They studied the effects of temperatures and load changes on cathodic pressure drops and observed the pressure drop overshoot and undershoot behavior [100]. During their later work [101,102], the pressure drop overshoot behavior could only be observed at lower temperatures due to the generated liquid water presented in the flow channels. In comparison, the overshoot behavior became insignificant at higher temperatures because of a higher water vapor fraction. They also found that the current change amplitude has more effects on the overshoot behavior of pressure drop compared to the current change ramps.

In general, the transient behavior of PEFCs compromises many different timescale processes, including electrochemical dynamic process, membrane hydration process, and liquid-vapor two-phase change process. The timescale for the electrochemical dynamics change is less than 0.1 s. It is more than 1 s for the membrane hydration

change process and the two-phase change process, which depends on the specific fuel cell operating conditions [103]. As a result, these different timescale processes lead to the overshoot or undershoot behavior of the fuel cell voltage/current outputs [104].

1.6   Motivation and Thesis Layout

1.6.1 Motivation

As discussed in the previous sections, LT-PEFC is a complex system that incorporates electrochemical reactions, two-phase flow processes, thermal and mechanical issues, etc. These phenomena are influenced by numerous physical parameters and directly influence the fuel cell's performance and stability. This thesis aims to fully understand the impact of different operating parameters and their mutual influences on in-house-assembled LT-PEFC's performance. To do so, the statistical experimental methods are implemented during the test. The steady-state behavior and dynamic behavior are investigated in a single cell operation. The effects of each selected operation parameter on cell performance and underlying mechanisms are identified, and further, the optimum operating conditions are determined.

1.6.2 Thesis Layout

Seven chapters support this thesis.

- Chapter 1 introduces the background, fundamental principles of LT-PEFC, a literature review of related research, motivation, and objectives of this thesis.
- Chapter 2 describes the knowledge of the statistical experimental methods implemented in the experiments.
- Chapter 3 presents detailed information on the experimental hardware.
- Chapter 4 investigated the accuracy of the in-house-assembled LT-PEFC.
- Chapter 5 and Chapter 6 statistically studied the static behavior and dynamic behavior of the in-house assembled LT-PEFC under various operating conditions.
- Chapter 7 and Chapter 8 provide a comprehensive discussion and present the conclusions.

2 Experimental Methods

This chapter introduces the concept of the Design of Experiments (DoE) method that was applied in this thesis, and also presents a literature review regarding the DoE application in the PEFC field.

2.1 Introduction

PEFC is a complex technology that comprises various fields of knowledge, such as electrochemistry, fluid mechanics, heat transfer and mechanical engineering, etc. A large number of input variables are involved in the experimental studies of the PEFCs. The strategy that commonly is employed to conduct these experiments is called OFAT, which means the 'One-Factor-at-A-Time' method [105]. This method implies that only one factor (or variable) can be changed at a time while the others remain fixed. It is easier to simply focus on one variable during each test by using the OFAT method, and it also allows experimenters to have a good intuition about the problem. OFAT is an option for tests that involve a small number of variables. When faced with a growing number of variables, however, OFAT leads to a huge effort in experimental work and a huge number of test results that are difficult to exploit. In addition, strong interactions may exist between the studied variables, which OFAT is not able to determine. Ignoring the interactions may lead to misinterpretation of the obtained results. These challenges motivate the development of effective testing strategies such as the Design of Experiments (DoE) methods [106]. The most applied DoE methods can be classified into factorial design and response surface methodology (RSM).

In 1920s, Ronald Fischer discovered and first applied the factorial design in the agriculture field, where the impact of factors such as water, fertilizer and other variables were studied simultaneously to determine the maximum crop yield of potatoes [107][108]. Based on the structure of the factorial design, Box and Wilson [109] developed the response surface methodology (RSM) in the 1950s, and it was applied in the chemical field and later in other fields [110]. Generally speaking, DoE is a statistical experimental method that is capable of investigating system characterization and optimization. The specific terminologies in DoE include response, factor, main effect, and factor interaction.

- Response: the outputs of the experiments in DoE, which can be quantitively measured to determine the effects of the factors on the studied systems.

- Factor: the independent variable that may influence the response. The types of factors in DoE can be classified into numeric factors or categorical factors. The numeric factors refer to quantitative variables that can be quantified by measurement, such as the values of temperatures. The categorical factors refer to qualitative variables that are expressed in a literal form, such as material types.
- Main effect: the effect of each factor that has a significant influence on the response.
- Factor interaction: when the effect of one factor on the response depends on the value of another factor (or more factors), we say there is an interaction between these factors.

The DoE is able to establish the relationships between the responses and the factors, as well as the factor interactions. Compared to the OFAT method, the benefits of the DoE become more apparent when dealing with more operating variables [111]. The number of runs is 2^k for a two-level factorial design, where k is the number of factors. The OFAT requires totaling runs of $(k+1)2^{k-1}$ to achieve the same precision for the factor effect estimation. It, therefore, requires a higher experimental effort of $(k+1)/2$ compared to the factorial design in DoE [112]. The DoE method can also estimate the interactions of various factors, which often reveal the key information in a system. In summary, the DoE methodology brings efficiency and accuracy to the experiment, enabling maximum information to be obtained at minimal costs. DoE can be treated as a tool package that includes different tools that can be chosen according to the aim of the investigation. The goal of this thesis is first to screen out the significant factors and to quantify the effects of these factors on the selected responses. Second, optimize the PEFC working process within the selected range of the factors.

2.2 The general procedures for conducting a DoE approach

The typical procedures for conducting a DoE can be broken into the following steps:

Step 1: Select the responses and factors.
The first step for conducting a DoE approach is to define the responses and to identify the factors of interest as well as their ranges. For a new system that experimenters have no prior knowledge of, one principal for the factor selection is that of selecting a large set of factors rather than a small set, in case some important factors may be missing [113]. The low and high levels of each factor are coded by the symbols (-1) and (+1). For numerical factors, it makes sense to assign the symbol (-1) to the lower values and the symbol (+1) to the higher values. For categorical factors, the symbols

of (-1) and (+1) will be assigned arbitrarily for each factor. Finally, the treatment combinations of these factors are presented in a table known as the design matrix. which will be discussed in the following sections.

Step 2: Define the experiment goals.

The second step is to define the goals of the work. These goals are normally to gain knowledge of the characteristics of a new system or optimization of a production process [114].

Step 3: Select experimental design.

According to the objectives of the work, various types of DoE can be applied to the experiment. The factorial design can be applied to screen out the important factors of the system. The response surface methodology (RSM) can be used to optimize the system working process. Furthermore, depending on the number and type of the factors involved in the experiment, additional methods such as fractional factorial design or split-plot design can be applied in conjunction with the factorial design or RSM to improve the accuracy and efficiency of the experiments.

Step 4: Build a regression model.

Once the experiments are finished with the guidance of the design matrix, the next step is to propose a regression model to describe the system. The coefficients of the main effect of each factor and the interaction effect between factors are calculated during this step. The terms that pass the significance test (ANOVA, Analysis of Variance [115]) can be added to the regression model.

Step 5: Regression model validation.

An experimental residual is the difference between the observed value and the fitted model value. The validation of the regression model is based on the assumptions of the experimental residuals that are: 1) the residuals have a constant variance for all levels of factors; 2) the residuals are normally distributed; 3) each residual is independent of each other. If no violations are present, a regression model can be used to analyze the system. Otherwise, it is necessary to check if there are any outliers in the data.

2.3 Factorial design

Factorial design is one type of screening technique that is widely used to screen out the important factors from a pool of factors and is also capable of quantifying the effect of these factors and their interactions on the selected responses. The most widely used case of factorial design is called a 2^k factorial design, where k means factor number, and 2 means each factor has only two levels. 2^k factorial design is quite effective at the early stages of the investigation experiments.

2.3.1 Full factorial design

Full factorial design means to conduct the complete 2^k runs of the experiment, which can have the highest precision in estimating the effect of each factor. It is widely used when the number of factors is low. However, it will take a huge experimental effort to complete the experiment when the number of factors is relatively high.

Table 2.1 illustrates the design matrix for a case of the 2^2 full factorial design. The factors are coded into (-1) for low levels and (+1) for high levels. The first column in Table 2.1 represents the standard operation order of each run, which is also referred to as the Yates order [116]. The level of each factor varies from run to run. In Yates order, the change of the levels in the first factor (factor A) is the fastest, and the last factor (factor B) is the slowest. The second column represents the actual run order of the experiments, which is in random order. It is important to note that each run of the experiment must be performed in a random order to eliminate any uncontrolled system disturbances, otherwise misleading results can be obtained [116].

Table 2.1: Design matrix for 2-level 2-factor full factorial design.

Std.	Run	Factor A	Factor B	Responses
1	2	-1	-1	y_1
2	4	+1	-1	y_2
3	3	-1	+1	y_3
4	1	+1	+1	y_4

The linear regression model of a factorial design can be described by the following equation:

$$y = b_0 + b_A x_A + b_B x_B + b_{AB} x_A x_B + e \tag{2.1}$$

where x_A and x_B are the coded variables of each factor, e is the experimental residual, b_0 is the constant term, b_A, b_B and b_{AB} are the coefficients of the coded variable of each factor and their interactions, respectively. Equation 2.1 can also be written in matrix form as shown in Equation 2.2:

$$y = Xb + e \qquad\qquad 2.2$$

where y is the vector of responses, X is called design matrix, b is the vector of coefficients and e is the vector of residuals. Inserting each term into Equation 2.2 can get as follows:

$$
\begin{bmatrix} y_1 \\ y_2 \\ y_3 \\ y_4 \end{bmatrix} =
\begin{bmatrix}
1 & x_{A-} & x_{B-} & x_{A-}x_{B-} \\
1 & x_{A+} & x_{B-} & x_{A+}x_{B-} \\
1 & x_{A-} & x_{B+} & x_{A-}x_{B+} \\
1 & x_{A+} & x_{B+} & x_{A+}x_{B+}
\end{bmatrix}
\begin{bmatrix} b_0 \\ b_A \\ b_B \\ b_{AB} \end{bmatrix} +
\begin{bmatrix} e_1 \\ e_2 \\ e_3 \\ e_4 \end{bmatrix}
$$

where x_i is the coded variable of each factor, so:

$$
\begin{bmatrix} y_1 \\ y_2 \\ y_3 \\ y_4 \end{bmatrix} =
\begin{bmatrix}
1 & -1 & -1 & +1 \\
1 & +1 & -1 & -1 \\
1 & -1 & +1 & -1 \\
1 & +1 & +1 & +1
\end{bmatrix}
\begin{bmatrix} b_0 \\ b_A \\ b_B \\ b_{AB} \end{bmatrix} +
\begin{bmatrix} e_1 \\ e_2 \\ e_3 \\ e_4 \end{bmatrix}
$$

Finally, the regression coefficients b can be calculated by the following equation:

$$b = (X^T X)^{-1} X^T y \qquad\qquad 2.3$$

Once the coefficients are determined, the next step is to use ANOVA (analysis of variance) to screen out the terms that are statistically significant which can be added into the regression model. Besides ANOVA, visual methods such as normal probability plots and Pareto charts are also widely used to assess the importance of each term [110].

The factorial design has been widely applied by many researchers in the field of PEFCs. Atanassova et al. [117] optimized the MEA structure through DoE and found that using 20% Pt-alloy as the catalyst at the cathode side can significantly improve cell performance. Lee et al. [118] investigated the influence of land width, channel width, channel depth and land corner radius on the moldability of a graphite composite bipolar

plate. They found that the factors of land width and flow channel depth have a significant influence on moldability. Torchio et al. [119] have studied the significance of the inlet gas temperatures, inlet relative humidities and stoichiometry ratios on the electric and thermal power of the stack at different current densities through the factorial design method. The results show that the anode inlet temperature and the cathode relative humidity are not significant factors at all levels of current density. The cathode inlet temperature and stoichiometry ratio have a strong positive effect on the electric power of the fuel cell stack.

2.3.2 Fractional factorial design

Fractional factorial design means that only half or a quarter fraction (or less) of the full set of experiments will be run, which causes only the main factor effects and the low-order interactions can be estimated. Since only a fraction of the experiments were performed, the high-order interactions cannot be estimated and are confounded with other factors. However, the high-order interactions often lack practical significance for many real systems. Thus, it is reasonable to lose some estimation power and gain more efficiency by using fractional factorial design [110].

A half fraction of the k factor factorial design means that 2^{k-1} runs should be performed. In the example of the 2^{3-1} fractional factorial design, the experiment is limited to 4 runs instead of 8 runs. Therefore, the 2^{3-1} fractional factorial design can be treated as a 2^2 full factorial design, the third factor C can be produced by the factor A and B, C=AB. The design matrix is illustrated in Table 2.2.

Table 2.2: Design matrix for 2-level 3-factor half fractional factorial design.

Std.	Run	Factor A	Factor B	Factor C =AB	Responses
1	2	-1	-1	+1	y_1
2	4	+1	-1	-1	y_2
3	3	-1	+1	-1	y_3
4	1	+1	+1	+1	y_4

A regression model for a 2^3 full factorial design would be:

$$y = b_0 + b_A x_A + b_B x_B + b_C x_C + b_{AB} x_A x_B + b_{AC} x_A x_C + b_{BC} x_B x_C + b_{ABC} x_A x_B x_C + e \qquad 2.4$$

Then, the matrix form of Equation 2.4 according to Table 2.2 is:

$$
\begin{bmatrix} y_1 \\ y_2 \\ y_3 \\ y_4 \end{bmatrix} = \begin{bmatrix} 1 & -1 & -1 & +1 & +1 & -1 & -1 & +1 \\ 1 & +1 & -1 & -1 & -1 & -1 & +1 & +1 \\ 1 & -1 & +1 & -1 & -1 & +1 & -1 & +1 \\ 1 & +1 & +1 & +1 & +1 & +1 & +1 & +1 \end{bmatrix} \begin{bmatrix} b_0 \\ b_A \\ b_B \\ b_C \\ b_{AB} \\ b_{AC} \\ b_{BC} \\ b_{ABC} \end{bmatrix} + \begin{bmatrix} e_1 \\ e_2 \\ e_3 \\ e_4 \end{bmatrix} \qquad 2.5
$$

It is observed that the four columns are identical to the other four in the X matrix, and this equation is unsolvable because the number of unknowns is greater than the number of equations. By grouping the identical columns, Equation 2.4 is transformed into a solvable equation:

$$
\begin{bmatrix} y_1 \\ y_2 \\ y_3 \\ y_4 \end{bmatrix} = \begin{bmatrix} 1 & -1 & -1 & +1 \\ 1 & +1 & -1 & -1 \\ 1 & -1 & +1 & -1 \\ 1 & +1 & +1 & +1 \end{bmatrix} \begin{bmatrix} b_0 + b_{ABC} \\ b_A + b_{BC} \\ b_B + b_{AC} \\ b_C + b_{AB} \end{bmatrix} + \begin{bmatrix} e_1 \\ e_2 \\ e_3 \\ e_4 \end{bmatrix} \qquad 2.6
$$

It is clearly shown that intercept (b_0) is confounded with the three-factor interaction (b_{ABC}), and the main effects (b_A, b_B and b_C) are confounded with the two-factor interaction (b_{BC}, b_{AC} and b_{AB}). There are no ways to separate these confounding factors apart. However, when there are a large number of factors in the system, the main effects will be confounded with other high-order interaction effects. According to the sparsity of effects principle [110], the most high-order interactions can be negligible in most systems. Therefore, it is safe to perform a fractional factorial design at the early stage of the experiments.

In the fuel cell field, Dante et al. [120] studied the influences of inlet pressures and flow rates at both anode/cathode sides on the output power of the PEFC through a 2^{4-1} fractional factorial design. The results show that the hydrogen inlet pressure and oxygen inlet flow rates are significant factors compared to others. Yu et al. [82] applied a 2^{6-2} fractional factorial design to screen the significant factors from the pool of factors. Then they determined the optimum operating conditions of these significant factors through the Taguchi method. The results indicated that the operating pressure has the most significant effect on cell performance. Wahdame et al. [121] studied the effects of the hydrogen/air pressure/flow rate on fuel cell's power and efficiency through both

full and fractional factorial design. The same conclusions were obtained through these two methods that the hydrogen/air inlet flow rate plays an important role regarding the output power and efficiency.

2.4 Split-plot design

Split-plot designs are normally applied to the experiment that contains the factors which are hard to be changed from run to run. Given the existence of these hard-to-change factors, applying a completely randomized design will result in high cost, low test efficiency, and may lead to incorrect results. A split-plot factorial design can be treated as a blocked experiment, in which the hard-to-change factors are served as blocks to the experiment. Correspondingly, there are two types of experimental units, namely whole plots and split plots, that exist in a split-plot design experiment. The whole plots are referred to as a set of hard-to-change factors, and the split plots are referred to as a set of easy-to-change factors. Therefore, two levels of randomization exist for the two types of experimental units, randomization at the whole plots level and randomization at the split plots level [122].

A case for the 2^4 factorial split-plot design is proposed and the design matrix is illustrated in Table 2.3. In this case, factor a is the whole plot factor, and factors B and C are the split-plot factors. The whole plot group in Table 2.3 can be treated as the blocks of the experiments. The whole plot factor is completely randomized between each whole plot group. Within each whole plot group, the split-plot factors are also randomized.

Table 2.3: Design matrix for 2^3 factorial split-plot design.

| | | | whole plot | split-plot | |
Std.	Run	whole plot group	a	B	C
3	1	1	-1	-1	+1
2	2		-1	+1	-1
5	3	2	+1	-1	-1
8	4		+1	+1	+1
6	5	3	+1	+1	-1
7	6		+1	-1	+1
1	7	4	-1	-1	-1
4	8		-1	+1	+1

As two types of randomizations are present in the split-plot design, so two types of experimental errors also exist in the regression model, one for the whole plot error, and the other for the split-plot error. Equation 2.7 represents the regression model for the 2^4 factorial split-plot design.

$$y = b_0 + b_a x_a + \eta + b_B x_B + b_C x_C + b_{aB} x_a x_B + b_{aC} x_a x_C + b_{BC} x_B x_C$$
$$+ b_{aBC} x_a x_B x_C + e$$

2.7

where η is the whole plot error and e is the split-plot error.

Although the split-plot design has been successfully applied in the industrial area, it remains underutilized in the area of fuel cells. Flick et al. [123] studied the influence of the type of GDL, cell temperature, cell operating pressure and inlet stoichiometry ratio on cell voltage and cathodic pressure drop through a 2-level factorial split-plot design. The results indicate that none of the factors at the anode side have statistical significance on the voltage of the cell. The type of GDL, cell temperature and their interactions are the most relevant factors for cell voltage. The GDL coated with MPL can substantially improve water management capacity and cell performance.

2.5 Response surface methodology

The aforementioned factorial design is intended to screen out the significant factors in a system, from which the main effects and the interaction effects of each factor can be estimated. While the response surface methodology (RSM) can be used to estimate not only the main effects and interaction effects but also the quadratic effects of each factor. The RSMs are widely used to optimize the selected responses [106]. Central composite design (CCD), face-centered central composite design, and Box Behnken design (BBD) are the three most common approaches used in RSM. Figure 2.1 illustrates the design structure of these design approaches in the case of 2-factor experiments. The CCD can be treated as a combination of the factorial design with star-points and center points. In Figure 2.1a), circles represent the factorial design combinations. Squares are known as star-points, which are used to calculate quadratic terms in the model. Diamonds are the replicated center-points that are used to estimate the true replicate error. The symbol α represents the distance from center-points to star-points. The value of α is usually set to 1 or $\sqrt[4]{2^k}$, which is usually determined by practical problems [124]. When the α is equal to 1, the CCD becomes the face-centered central composite design. Figure 2.1b) shows that the BBD is a three-level

design that only consists of the star-points and the center-points. The BBD is quite applicable when the factor level combinations of the factorial design are too extreme or hard to test due to some physical constraints [124].
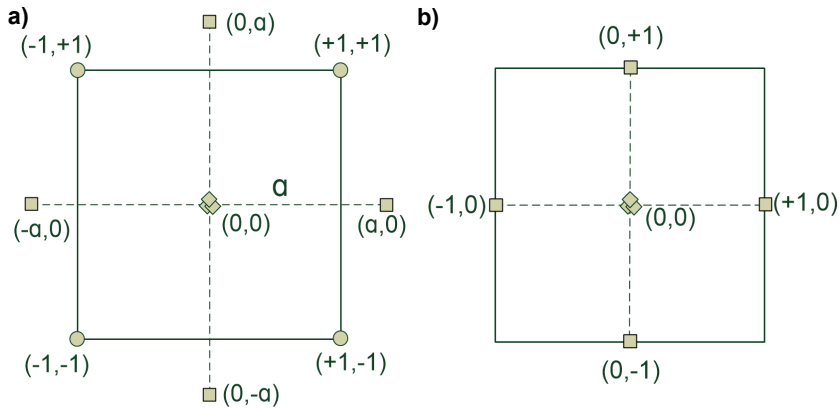

Figure 2.1: The design structure of, a) central composite design with star-point distance α, b) Box Behnken design, when the factor number k=2.

Table 2.4 illustrates the design matrix of the 2-level 2-factor CCD. Experiments 1-4 are the factorial design part, experiments 5-8 are the star-points part and experiments 9-11 are the center-points part.

Table 2.4: Design matrix for 2-level 2-factor CCD.

Std.	Factor A	Factor B	Responses
1	-1	-1	y_1
2	+1	-1	y_2
3	-1	+1	y_3
4	+1	+1	y_4
5	-1	0	y_5
6	+1	0	y_6
7	0	-1	y_7
8	0	+1	y_8
9	0	0	y_9
10	0	0	y_{10}
11	0	0	y_{11}

The linear regression model of the 2-level 2-factor CCD can be described by the following equation:

$$y = b_0 + b_A x_A + b_B x_B + b_{AB} x_A x_B + b_{AA} x_A{}^2 + b_{BB} x_B{}^2 + e \qquad\qquad 2.8$$

where e is the experimental residual, b_0 is the constant term, b_A and b_B are the first-order coefficients, b_{AB} is the interaction coefficient and the b_{AA} and b_{BB} are the quadratic coefficients.

The RSM has been successfully applied in the fuel cell field by a number of researchers. Garton and Olabi [125] applied the Box Behnken design to study the effect of different flow plates on cell performance at different operating conditions. The results show that the serpentine flow plate has a better performance compared to the parallel or maze flow plate design. The optimized operating conditions were carried out through the BBD approach. Kahveci and Taymaz [126] investigated the water and heat management of the PEFC through central composite design. Four parameters, namely cell temperature, hydrogen/oxygen flow rate and inlet relative humidity, are selected as input factors and power density is selected as the response. It was found that the effects of the cell temperature and relative humidity on power density are higher than that of the hydrogen and oxygen flow rates. The values of four factors were optimized and the maximum power density of 241.977 mW/cm^2 was achieved. Hasheminasab et al. [127] applied the CCD to water management investigations on a transparent PEFC. The effects of inlet temperature, anodic and cathodic stoichiometry were analyzed on the responses of the cell power, GDL water coverage ratio (WCR) and two-phase pressure drop coefficient (Φ). Quadratic regression models were constructed and favorable WCR bandwidth ($3 \leq WCR \leq 4$) was obtained, based on which a water management strategy was carried out and values of the three factors could be retrieved.

2.6 Summary

An overview of the Design of Experiment (DoE) method for the PEFCs was introduced in this chapter. The corresponding terminology and the general procedures of the DoE were presented at the beginning. Then the detailed information about the different types of the DoE, namely full/fractional factorial design, split-plot design, and response surface methodology, was discussed in the following sections. The factorial design is normally used in the early stages of an investigation about a new system. It can screen out significant factors and can also quantitively analyze the effect of each factor on the selected responses. When the number of the selected factors is high, then the

fractional factorial design is recommended to improve experimental efficiency. The split-plot design can be applied when some hard-to-change factors exist in the system, which will greatly improve the experiment efficiency and accuracy. At last, the RSM can be used to optimize the process of a system. All these designs were applied in a combination way in this thesis.

3 Experimental setup and procedures

This chapter presents the structure of the used test cell, the modification of its components, the test station, and the equipment of EIS measurements as well as its detailed parameter settings. Part of this chapter has been published in [89].

3.1 Test cell

3.1.1 Test cell components

The test cells used in the experiment are developed, manufactured and assembled at Forschungszentrum Jülich. The test cell components are illustrated in Figure 3.1

Figure 3.1a) shows the Gore PRIMEA catalyst-coated membrane (CCM), which active area is 17.64 cm^2. The thickness of this CCM is around 42 µm, including 18 µm for the membrane and 12 µm for each catalyst layer [128]. The Pt loading of each side is equal to 0.1 (anode) / 0.4 (cathode) mg/cm^2 [129].

Figure 3.1b) presents the Freudenberg H23C2 non-woven carbon fiber Gas Diffusion Layer (GDL) which was placed on top of both electrodes. It has a thickness of 215 µm at 1 MPa. The GDL is coated with an MPL on the side which is oriented towards the electrode, because it provides better fuel cell performance compared to the uncoated GDL. There is 40% PTFE loading in MPL and 0% in GDL basic material.

Figure 3.1c) shows the Sigraflex graphite sealing gaskets from SGL CARBON COMPANY, which are placed between the flow field plate and endplate for sealing and also for excellent electric conductivity.

Figure 3.1d) shows the perfluoroalkoxy alkanes (PFA) gasket, flow field plate and metal endplate. The PFA gasket additionally serves as a hard stop for the GDL compression, and also can electrically isolate the anode side and the cathode side from each other. The thickness of the PFA gasket is 200 µm. This value can result in the compression rates of GDL to 20-25%, which can minimize the contact resistance between the GDL and other components [130][131], and also can increase the water transportability in both GDL and MPL [132].

The in-house-designed monopolar plate applied in the present work was fabricated from a graphite composite. The detailed drawing of the monopolar plate is shown in

Figure 3.2, where the flow field is also presented. The flow field consists of three parallel serpentine channels, each of which has a quadratic cross-section with 1 mm width and 1 mm depth, and a land width that is also 1 mm. The flow fields at both monopolar plates have symmetrical designs. The endplate was also used as the current collector plate and was fabricated from stainless steel type 1.4571 (316 Ti). It also has special holes for the cartridge heaters and thermocouples which were used to control and monitor the cell temperature. In addition, the reaction and product gases are supplied and removed via the endplate.
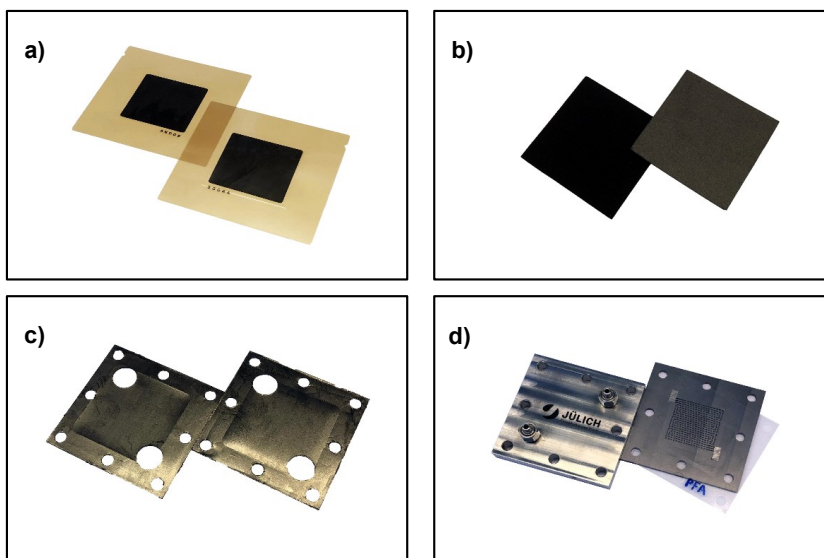
Figure 3.1: a) Gore PRIMEA catalyst-coated membrane b) Freudenberg H23C2 Gas diffusion layer c) Sigraflex graphite sealing gaskets d) PFA gasket, the in-house-designed monopolar plate with flow field and stainless steel endplate.
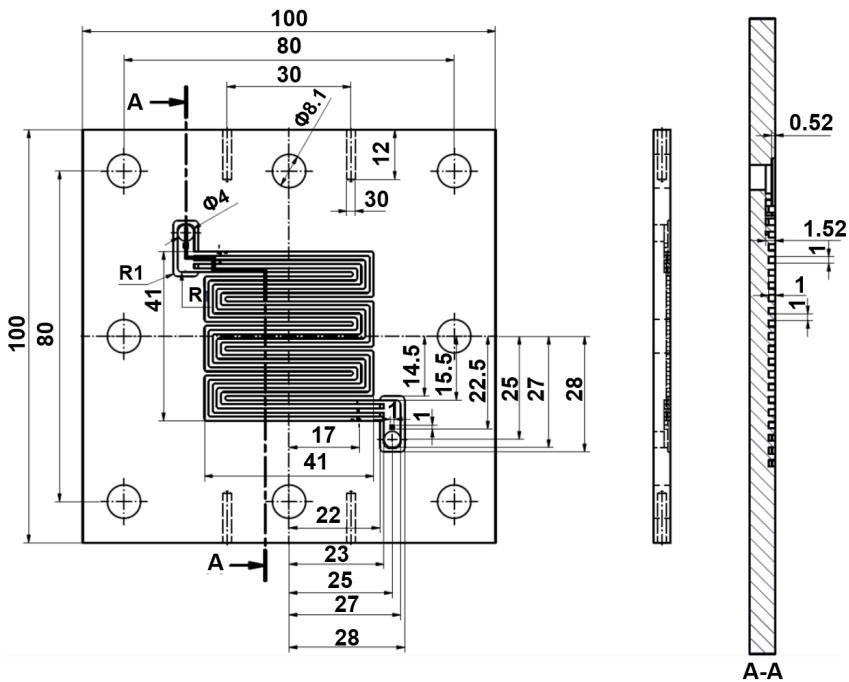
Figure 3.2: Detailed drawings of the monopolar plate and the flow field.[89]

3.1.2 Test cell assembly and leak testing

Figure 3.3 provides a detailed assembly procedure for a test cell.

a) The eight screws were passed through the holes in the cathode endplate, which was placed in a plastic device to prevent slipping. Each screw was to be provided with a washer and a long isolating ring to prevent crosswise movement and also to avoid shortcuts between the anode side and cathode side. A Sigraflex sealing gasket was then placed on the cathode endplate to ensure gas tightness between the endplate and flow field plate.

b) The correct location should be noticed during placing the cathode flow field plate, which means that the holes for the voltage measurement on the flow field plate must be at the top side. The next step is to place the PFA gasket and GDL on the flow field plate. The PFA gasket must be cleaned with isopropanol. The grey side of the GDL (without MPL) should be attached to the flow channel.

c) The Gore CCM was cut to an area of 7 cm x 7 cm, any area smaller than this may cause an inner leakage issue. One important point is that the anode side of the CCM should be placed on the upper part. Then place the anode side PFA gasket and GDL on the CCM. The black side (MPL) of GDL should be attached to the CCM.

d) The anode flow field was then placed on the CCM with the holes facing upwards and the flow channel lying horizontally. The second Sigraflex seal was placed on the anode flow field plate and the anode endplate was placed on the Sigraflex seal gasket.

e) During the screw connection process, the cell bolts should be torqued in a diagonal pattern [133]. The recommended torque applied to each bolt is 6 Nm. The torque was set incrementally on each bolt by 2 Nm increments until the final target torque is reached. Figure 3.3f) Shows a successfully assembled test cell.
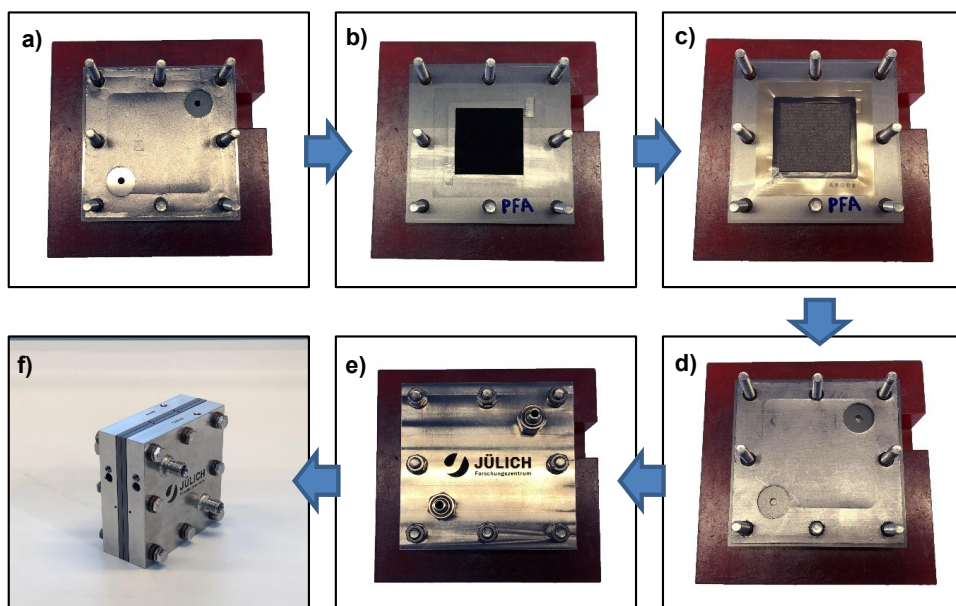
Figure 3.3: Assembly process of the test cell. a) cathode side endplate and Sigraflex gasket, b) cathode side flow field plate, PFA gasket and GDL, c) CCM, anode side GDL and PFA gasket, d) anode side flow field plate and Sigraflex gasket, e) anode side endplate, f) assembled test cell.

The leak checking procedure should be performed after the test cell was successfully assembled. Connect the test cell to the leak checking device, as shown in Figure 3.4.

Nuts seal the outlet port on the anode and cathode sides. Close the gas outlet valve on the leak checking device. Nitrogen was supplied to both inlet ports of the test cell, wait until the pressure inside the test cell has reached around 0.4 bar. Then the inlet valves were closed and the pressure was measured over one minute. If the pressure value did not decrease more than 0.04 bar in one minute, the test cell could be assumed technically tight enough. Release the pressure at one side and close the outlet valve. If the pressure on the other side does not decrease, there is no transverse leak between the anode side and the cathode side. Otherwise, the PFA gaskets, GDL and CCM inside this test cell should be cleaned or replaced if necessary. After the tightness of the cell has been ensured, it can be installed in the test station. A pressure test should be carried out again on the test station in order to check the tightness of the test stand and the connection between the test station and the test cell. The maximum value for the pressure drop within one minute is also 0.04 bar.
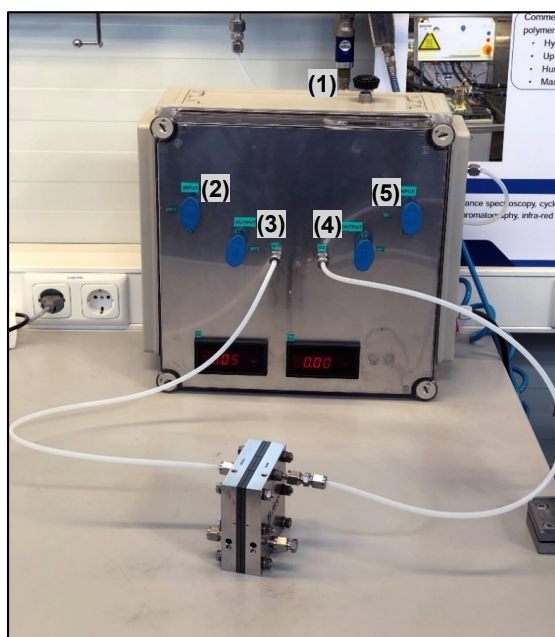
Figure 3.4: Leak checking device, (1) Flow control valve, (2) and (3) Gas input valve, (4) and (5) Gas output valve

3.1.3 Test cell break-in and reconditioning procedure

In order to maintain the stable performance of the test cell for subsequent application, a repeatable break-in procedure needed to be performed for the newly assembled test

cell [133,134]. The detailed break-in procedure is shown in Table 3.1. During the break-in procedure, the test cell was heated up to 70°C, with fully saturated (relative humidity (R.H.) = 100%) hydrogen at 1.2 stoichiometric ratio and fully saturated air at 2.5 stoichiometric ratio. The current was increased until the cell voltage reached 0.6 V. Then, the test cell was operated under the potentiostatic mode, the cell voltage was cycled between 0.6 V (30 min), 0.4 V (30 min), and OCV (1 min) approximately 6–8 times until there was no further increase in cell performance [135]. The reconditioning procedure was performed before each test in order to set the equal start condition. During the reconditioning process, the test cell temperature was set at 70°C, with fully saturated hydrogen at a stoichiometric ratio of 1.2, and fully saturated air at 2.5. The cell voltage was set to 0.6 V for 30 min of operation. This step was used to make sure that the membrane was fully hydrated and that the test cell has the same historic situation before each test. It should also be noted that the stoichiometric ratio was set to 0.2 A/cm^2. If the current density was below 0.2 A/cm^2, the flow rate of the reactants was set constantly according to 0.2 A/cm^2.

Table 3.1: Test cell break-in procedure

	Temperature	Gas	Relative Humidity	Stoichiometry ratio	Load	Time
Heat up	25℃	N_2	100%	1.2/2.5	OCV	15 min
	25℃	H_2 and air	100%	1.2/2.5	OCV	5 min
	40℃	H_2 and air	100%	1.2/2.5	0.6V or 0.05 A/cm^2	5 min
	50℃	H_2 and air	100%	1.2/2.5	0.6V or 0.1 A/cm^2	5 min
	60℃	H_2 and air	100%	1.2/2.5	0.6V or 0.5 A/cm^2	5 min
	70℃	H_2 and air	100%	1.2/2.5	0.6V or 0.7 A/cm^2	5 min
Cycling	70℃	H_2 and air	100%	1.2/2.5	0.6V or 0.7 A/cm^2	30 min
	70℃	H_2 and air	100%	1.2/2.5	0.6V or 1.2 A/cm^2	30 min
	70℃	H_2 and air	100%	1.2/2.5	OCV	1 min

3.1.4 Test cell modification

Figure 3.5 presents the mechanical failures of the CCM, such as the cracks along the inside edge of the PFA gasket and the holes at the gas inlet region, which were observed at the early period of the experiment. It caused rapid gas crossover and then the failure of the test.
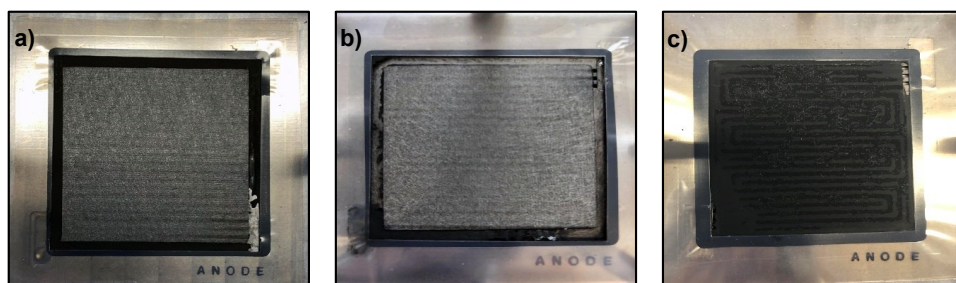
Figure 3.5: Mechanical failures of CCM, a) and b) are the cracks along the inside edge of the PFA gasket, c) is the hole at the gas inlet region.

It seems that all of these failures occurred in the areas which were not protected by the GDL or PFA gasket. Some research explained these phenomena from a mechanical perspective [136]. Qiu et al. [137] numerically studied the stress evaluation along with the CCM frame at different operating conditions. They concluded that the gas filling process is the main factor that causes the mechanical failure of the membrane in the edge area. Bograchev et al. [138] studied with a two-dimensional model the evolution of the membrane stress in an operating fuel cell. They found that the peak stress occurred in the membrane's edge, and the plastic deformation would also be started from this area. Consistent findings regarding the edge stress were also founded by Solasi et al. [136] and Huang et al. [139]. Several factors probably cause this damage to the membrane's edge: 1) The compression between GDL and hard stop PFA gasket may cause the bending of the membrane which leads to the increase of the mechanical stress; 2) The reactant gases directly crash on the membrane especially on the inlet region, and the pressure difference between the anode side and cathode side at higher gas volume flows. 3) The heat generated by the electrochemical reaction in this GDL-CCM-PFA gasket joint area could not be removed effectively, which caused a hot spot and consequently increased the degradation of the membrane [138]. Some researchers used an additional protection layer to prevent the failure of the weak joint area [140]. Figure 3.6 shows the solution in our case. The inside dimension of the PFA gasket was reduced so that it can cover most parts of the joint

area, especially the inlet and outlet region. It can prevent the shock of the gas directly working on the CCM, and also decreases the chance to generate a hot spot in the CCM edge area.
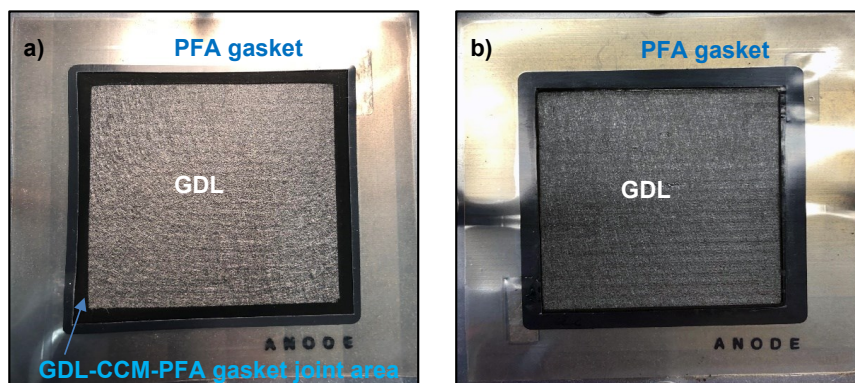
PFA inside dimension: 4.5 x 4.5 cm^2 PFA inside dimension: 4.2 x 4.2 cm^2

Figure 3.6: The comparison between the, a) original PFA gasket, and b) modified PFA gasket.

3.2   Test station

The experimental operating conditions were controlled by Greenlight Technology's G40 test station from Greenlight Innovation Corporation. The test station is composed of the reactant gas supply system, load system, data acquisition system, safety system, and other subsystems, which are integrated into the test station's body (Figure 3.7(1)). The test station can be operated in either current mode or voltage mode. The range of the current is from 0 A to 80 A, and the range of the voltage is from 0.0 V to 50 V, but it is limited by the software to 5 V. The maximum data recording rate is 100 Hz. The test station is capable of shutting down automatically if the monitored voltage (or current) drops below a pre-defined critical value or shutting down manually by pressing the emergency button (e-stop button). Consequently, a nitrogen purge process will be started at the same time. The Emerald control and automation software, which is shown in Figure 3.7(2), is used to monitor and control the reactant gas flow rate, temperature and relative humidity based on the experimental requirements. With the automation script, the test station can be operated entirely unattended 24 hours per day. Figure 3.7(3) shows the test station working space where the test cell is mounted in the test station. The detailed configuration is shown in Figure 3.8. The voltage test ports are inserted into the monopolar plate to record the cell voltage. Two cartridge

heaters are inserted into the endplates to control the cell temperature. Two thermocouples are inserted into each endplate to measure the cell temperature. A manometer is used to measure the two-phase flow pressure drop on the cathode side. Detailed information on the Greenlight test station and its capabilities can be found in the Instruction Manual [141].
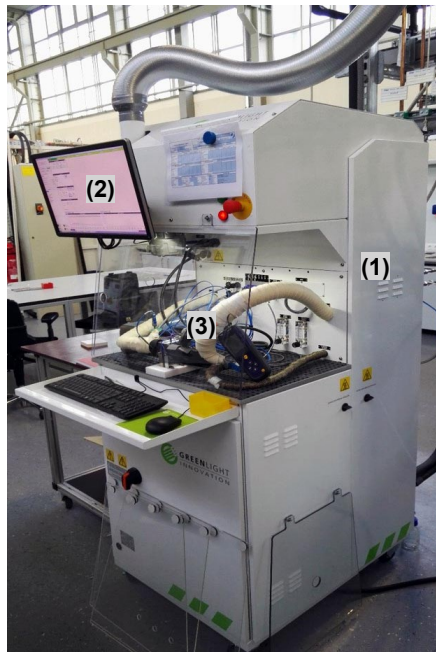
Figure 3.7: Greenlight G40 Test station, (1) Test station's body, (2) Computer control unit, (3) Test station working space.
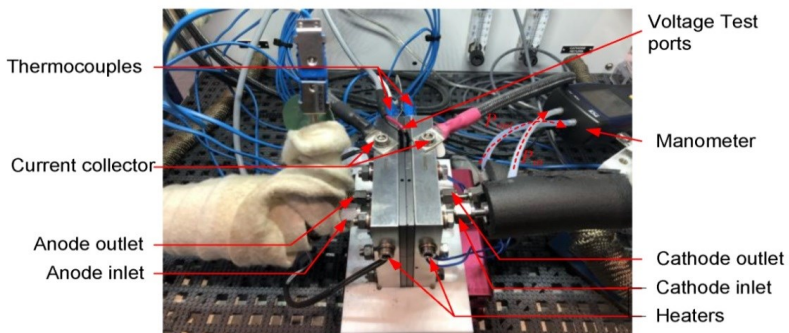
Figure 3.8: Picture of test cell connected to the test stand [89].

3 Experimental setup and procedures

A brief description of the reactant gas supply system configuration is shown in Figure 3.9. The reactant gas supply system supplies fuel, oxidant, and inert gas to the test cell. It consists of three gas paths, namely hydrogen path, air path and nitrogen purge path. In the hydrogen path, the flow rate and the humidity of the reactants are regulated by the mass flow controller and the anode humidifier, the temperature of the reactants is controlled by the heating pipe between the humidifier and the test cell. Then the humidified reactants are introduced into the test cell. Another option is that hydrogen flows through the bypass to stay dry, which is needed in some specific experiment design. The pressure and the temperature are measured in the inlet and outlet part of the test cell. A backpressure regulator located in the exhaust part allows the regulation of the pressure in the system. Finally, the exhausted hydrogen passes through the condenser and is then pooled into the exhaust system. The configuration of the air path is just the same as that of the hydrogen path.
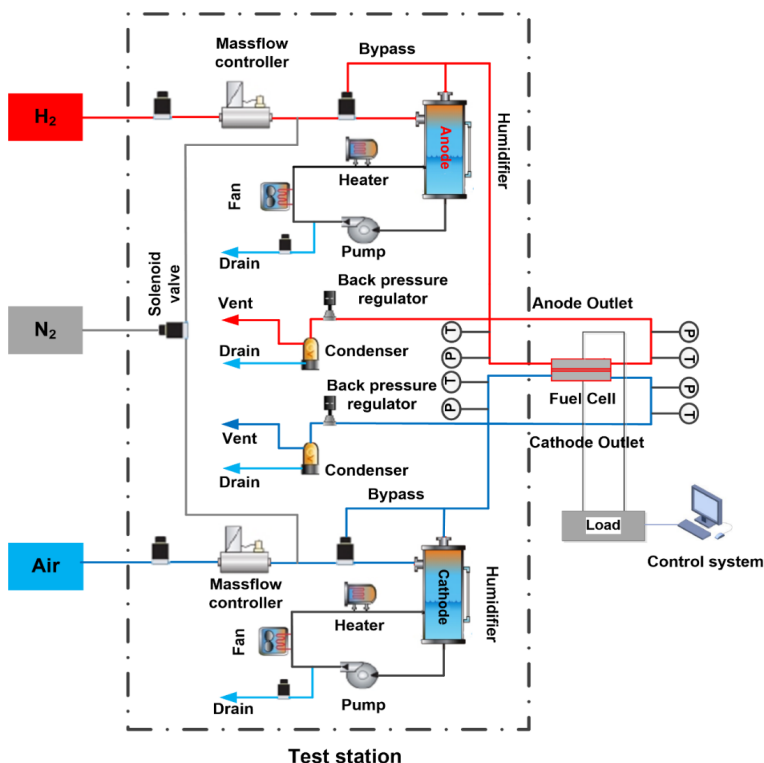
Figure 3.9: Schematic of Gas supply system configuration (Redraw on the basis of [134][141]).

3.3   Ohmic resistance measurement

The ohmic resistance measurement of the test cell was performed by an EIS electrochemical workstation from ZAHNER-Elektrik GmbH & Co. KG. This workstation includes two parts, namely the Zahner Zennium and Zahner PP241 power potentiostat, which are shown in Figure 3.10. Zahner Zenium can perform the EIS measurements and the PP241 potentiostat can supply the additional power in the case of the high current measurements. Table 3.2 presents the detailed specifications of the EIS electrochemical workstation.

Figure 3.10: EIS electrochemical workstation, (1) Zahner PP241 power potentiostat, (2) Zahner Zennium device.

The AC impedance spectroscopy can reflect the water content inside the fuel cell. However, the full frequency range scan takes a long time (generally around 10 minutes), which limits its application in some specific experiment designs. Therefore, many researchers only make measurements in the high-frequency region. Barbir et al. [141] used a commercial milliohm meter 4338B with a fixed frequency of

1 kHz for the high-frequency impedance testing and used this impedance as the fuel cell ohmic resistance. Actually, when the imaginary part is 0 or the phase angle is 0° at the high-frequency region, the impedance value is equal to the ohmic resistance. However, after setting a specific frequency value, a fluctuation of the phase angle was observed during the test. In this case, the data was only recorded when the phase angle falls between the range of -5° to +5°, as shown in Figure 3.11.

Table 3.2: Detailed specifications of the EIS electrochemical workstation.

	Characteristic	Value	Accuracy
PP241 potentiostat	Current range	0 A to ±40 A	±0.25% / ±1 mA
	Potential range	±5 V	±0.1% / ±1 mV
	Output Power	200 W	/
	Frequency range	10 µHz - 200 kHz	/
	Impedance range	1 µΩ - 1 kΩ	/
Zahner Zennium	Current range	±100 nA to ±2.5 A	±1% of the set value
	Potential range	±4 V	±250 µV (0.025%)
	Frequency range	10 µHz to 4 MHz	<0.0025%
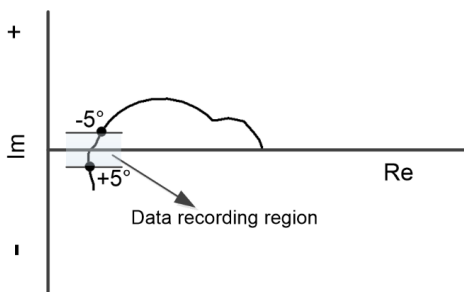
Figure 3.11: Data recording region.

3.4   Summary

This chapter presents the information of the test cell and the test apparatus used in the experiment. Test cell components, assembly procedures and its structure modifications were discussed and also to the detailed specifications of the test station, EIS electrochemical workstation.

3 Experimental setup and procedures

4 Accuracy study of the test cell performance

This chapter presents the accuracy studies for the in-house-assembled LT-PEFC with the aim to evaluate the accuracy of the LT-PEFC's performance. Due to the unavoidable random errors caused by a variety of factors, which are comprised of: (a) test samples, (b) test equipment, (c) test procedures, (d) test operators and (e) test environment which includes ambient temperature, humidity, pressure, etc., the identical results can be hardly obtained even if the tests were conducted under the presumably identical test conditions. The variation caused by different operators (or different equipment) will usually be more significant than that of the single operator who is working on the same equipment. The longer duration between the measurements may also lead to additional oscillations in the test results, because longer time periods may lead to changes in the environmental factors. In order to determine the uncertainties of the test results and to get consistent data, an accuracy test was performed with four identical test cells which were tested sequentially on the same test station. These test cells were assembled by the same operator using four sets of components (including endplates, flow field plates, GDLs and CCMs) which are from the same batch. Finally, the repeatability and reproducibility of the test results were determined via the analysis of Mandel's k statistics and h statistics. The structure of the accuracy study is shown in Figure 4.1.

4.1 Definitions

The accuracy study was designed based on the international standard ISO 5725, which defines a standard method for analyzing the accuracy of the measurement results. There are six parts included in the ISO 5725, of which part 1 [142] (*ISO 5725 Accuracy (trueness and precision) of measurements methods and results - Part 1: General principles and definitions.*) gives the detailed principles and definitions of the standard measurement. Some important terms associated with the accuracy study are listed below.

Accuracy: A concept that describes the trueness and precision of the test method, test result, or test system. According to ISO 5725 part 1, a demonstration of the trueness, precision and accuracy is shown in Figure 4.2.

Trueness: A concept that describes the closeness between the mean value of the obtained test results and the acceptable "true" value (or theoretical value based on the scientific principles).

Precision: A concept that describes the closeness between the repeated test results. The precision is typically expressed in two terms, which are repeatability and reproducibility. In this accuracy study, the precision of the test cell was determined through a standard procedure based on the ISO 5725 part 2 [143] *Basic method for the determination of repeatability and reproducibility of a standard measurement method.*

Repeatability: A concept that refers to the variability of the repeated test results obtained under the repeatability conditions, where the factors from (a) to (e) are assumed constant. It is usually expressed by the repeatability standard deviation or repeatability limit.

Repeatability standard deviation (S_r): A term that can be used to express the repeatability quantitatively, typically represented by S_r. It shows the dispersion of measurement results under repeatability conditions.

Repeatability limit (*r*): An alternative term that expresses the repeatability, typically represented by *r*. It represents that under a given repeatability condition, there is a 95% probability that the difference between any two test results will not exceed this limit *r*. As a rule of thumb, it can be expressed by the following equation [144][145]:

$$r = 2.8 s_r \qquad\qquad 4.1$$

Reproducibility: A concept that refers to the variability of the repeated test results obtained under the reproducibility conditions, where the factors from (a) to (e) are assumed changed. In order to study the precision of our in-house-assembled test cell, the reproducibility condition in this accuracy study refers to that factor (a) is changed and the factors (b) to (e) are assumed constant.

Reproducibility standard deviation (S_R): A term that can be used to express the reproducibility quantitatively, typically represented by S_R. It shows the dispersion of measurement results under reproducibility conditions.

Reproducibility limit (*R*): An alternative term that expresses the reproducibility, typically represented by *R*. It represents that under a given reproducibility condition, there is a 95% probability that the difference between any two test results will not

exceed this limit *R*. As a rule of thumb, it can be expressed by the following equation [144][145]:

$$R = 2.8s_R \qquad\qquad 4.2$$

Outlier: A term that describes a group/single value in the data which is significantly different from others.
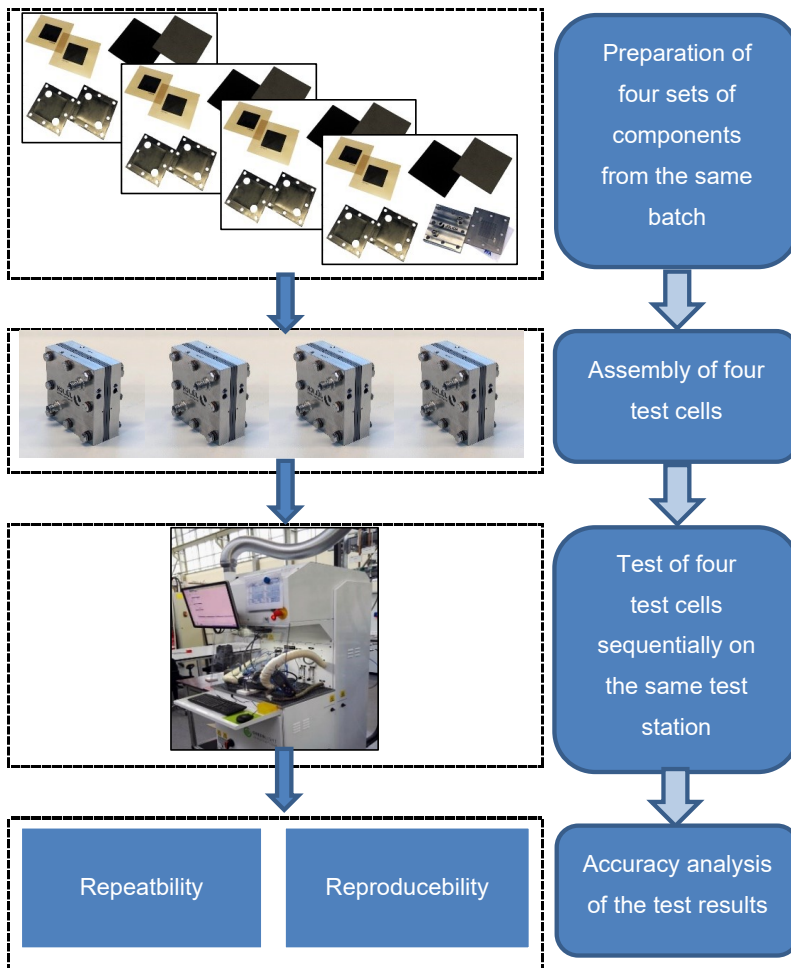
Figure 4.1 The structure of the accuracy study.
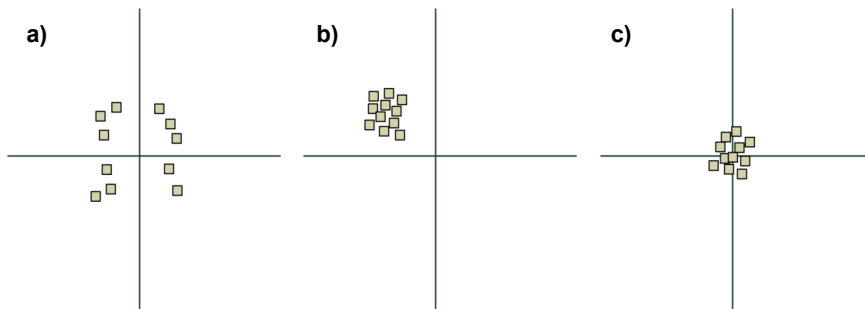
Figure 4.2: The demonstration of a) high trueness, low precision, b) high precision, low trueness, and c) high accuracy (high trueness and high precision).

4.2   Experimental

The detailed configuration of the test cell and test station used in this accuracy study has already been mentioned in chapter 3.

4.2.1 Operating conditions

The operating conditions used in the accuracy measurements are shown in Table 4.1. The experiments were performed at three different conditions which are: condition A, 60°C with the reactants relative humidity of 50% (Anode) / 50% (Cathode); condition B, 70°C with 30% (Anode) / 90% (Cathode); and condition C, 80°C with 90% (Anode) / 30% (Cathode). The different combinations of stoichiometry ratios and current density will also be performed for each condition. The process of each step will take 60 minutes. All experiments were conducted at ambient pressure.

4.2.2 Operating procedures

The operating procedures applied in the accuracy test are summarized in Table 4.2. Four test cells were assembled and tested sequentially during the experiment. The break-in procedure was performed for each newly assembled test cell. Subsequently, the conditioning procedures were performed in advance at each operating temperature to eliminate the historical influence. When the operating conditions (not the current density) were set to another value during the cell operation, to ensure that the test cell reached its steady state, a constant current density of 0.6 A/cm^2 was applied until all setpoints have reached the target value and remained constant for 10 minutes. During the testing process, the cell voltage response under each operating condition was recorded and used for the subsequent analysis.

Table 4.1: Operating conditions for the accuracy test.

Condition A	Condition B	Condition C	Stoichiometry ratio	Current density (A/cm^2)	Holding time (min)	Code
(A) Temperature = 60°C Rel. humidity: Anode 50% / Cathode 50%	(B) Temperature = 70°C Rel. humidity: Anode 30% / Cathode 90%	(C) Temperature = 80°C Rel. humidity: Anode 90% / Cathode 30%	1.2/2.5	0.2	60	1-1
			1.2/2.5	0.4	60	1-2
			1.2/2.5	0.7	60	1-3
			1.2/2.5	1.0	60	1-4
			2/4	0.2	60	2-1
			2/4	0.4	60	2-2
			2/4	0.7	60	2-3
			2/4	1.0	60	2-4
			1.5/2	0.2	60	3-1
			1.5/2	0.4	60	3-2
			1.5/2	0.7	60	3-3
			1.5/2	1.0	60	3-4

Table 4.2: Operating procedures for the accuracy test.

Step	Description	Specifications
Break-in	A break-in procedure was performed on the newly assembled cell.	See Chapter 3 for details.
Conditioning	This procedure was performed when a new operating condition was established.	See Chapter 3 for details.
Cell operation	Four test cells were operated sequentially for targeted operating conditions.	See table 4.1 for details.

4.3   The statistical analysis procedures

4.3.1 The basic statistical model

The basic model for the analysis of the accuracy of the test results can be expressed by the following equation [143]:

$$y = \bar{\bar{y}} + B + e \qquad\qquad 4.3$$

where:

y: test results,

$\bar{\bar{y}}$:   gross average of the test results,

B: variation part caused by the different repeatability conditions, and

e: random error in each measurement.

The variation B is generally considered as the sum of the systematic and random error caused by the different repeatability conditions, which include: (a) test samples, (b) test equipment, (c) test procedures, (d) test operators and (e) test environment which includes ambient temperature, humidity, pressure, etc.

Between-cell variance (σ_B^2): In this accuracy study, the term B is only caused by the change of factor (a) test samples (test cell). Thus, it can be treated as a between-cell variation. The expectation of B is assumed to be equal to 0, and the variance of B is called the between-cell variance, σ_B^2.

Within-cell variance (σ_W^2): In this accuracy study, the random error e occurs in measurement for each test cell, it can be treated as a within-cell variation. The expectation of the random error e is assumed to be 0, and the variance of e is called the within-cell variance, σ_W^2.

Repeatability variance (σ_r^2): It is expected that the difference of the within-cell variance between the four test cells should be small. This is because the test cells were assembled by the components from the same batch and same operator. Repeatability variance is a pooled variance that can be used to represent the within-cell variance for all test cells. The repeatability variance can be calculated by the arithmetic average of the within-cell variance, which is expressed by the equation:

$$\sigma_r^2 = \overline{var(e)} = \overline{\sigma_W^2} \qquad\qquad 4.4$$

where:

σ_r^2:   repeatability variance, and

σ_W^2:   within-cell variance,

Reproducibility variance (σ_R^2): Apart from the repeatability variance, another term that is reproducibility variance should also be considered during the analysis of the precision for the test cell. The reproducibility variance can be expressed by the following equation, which is the sum of the between-cell variance and the repeatability variance:

$$\sigma_R^2 = \sigma_B^2 + \sigma_r^2 \qquad\qquad 4.5$$

where:

σ_R^2:   reproducibility variance,

σ_B^2:   between-cell variance, and

σ_r^2:   repeatability variance.

In statistical practice, the true value of the results will never be known because the test results are based on the small number of samples rather than the whole population. So, the true value symbol σ is then replaced by the estimated value symbol s in the following calculation. The detailed calculations about the above parameters are listed in Appendix A.1 and A.2.

4.3.2   The consistency statistics

In order to evaluate the accuracy of the data obtained from test cells, the graphical technique name is called Mandel's k and h statistics were used in this study [144][146].

Mandel's k statistics, normally referred to as k-value, are used to evaluate the within-cell consistency. It is calculated by the within-cell standard deviation and the repeatability standard deviation, which can be expressed by the following equation:

$$k_i = \frac{s_i}{s_r} \qquad\qquad 4.6$$

where:

k_i: within-cell consistency statistics for i_{th} test cell,

s_i: standard deviation for i_{th} test cell, and

s_r: repeatability standard deviation, also known as pooled within-cell standard deviation for each test cell.

The k-value reflects the data's precision for each test cell. It uses the single cell's repeatability in contrast to the average repeatability for all test cells. A large k-value thus implies widespread data, and hence poor data precision. The critical k-value is used as a criterion to evaluate the seriousness of the data's spread deviation at a given significance level. If the k-value exceeds the critical k-value, it means that the test results have poor precision.

Mandel's h statistics, normally referred to as h-value, are used to evaluate the between-cell consistency. It makes the comparison between the deviation for one test

cell and the average deviation for all test cells, which can be expressed by the following equation:

$$h_i = \frac{d_i}{s_{\bar{y}}}$$ 4.7

where:

h_i: between-cell consistency statistics for i_{th} test cell,

d_i: deviation of the average value for i_{th} test cell, and

$s_{\bar{y}}$:   standard deviation of the test cell averages.

The h-value reflects the trueness of the data for each test cell. A larger h-value implies a higher deviation from the average, and hence the poor data trueness for the specific test cell. The critical h-value is used as a criterion to measure the seriousness of the data's deviation from the average at a given significance level. If the h-value exceeds the critical h-value, it means that the test results from the specific test cell have poor trueness and are not reliable. The detailed calculations about critical k-value and critical h-value are listed in Appendix A.3.

4.4   Results and analysis

The statistics used for the accuracy study were calculated according to Equations A.1 to A.9 (In Appendix). The statistics results for operating conditions A1-1 are listed in Table 4.3. The results for other operating conditions are listed in Appendix A.4. The graphs for Mandel's k and h statistics are presented in Figure 4.3 (k statistics) and Figure 4.4 (h statistics) in which the consistency of the test cell under different operating conditions is provided.

Table 4.3: The statistics data for operating condition A1-1.

Test cell Number	$\bar{y}$ (V)	s (V)	d (V)	h	k
1	0.757440	0.004596	0.005544	0.6660	0.9083
2	0.745329	0.004851	-0.006567	-0.7888	0.9587
3	0.744236	0.005582	-0.007660	-0.9201	1.1032
4	0.760578	0.005157	0.008682	1.0429	1.0192

Gross average, $\bar{\bar{y}}$ = 0.751895 V

Average standard deviation, $s_{\bar{y}}$ = 0.008325 V

Repeatability standard deviation, s_r = 0.005060 V

Reproducibility standard deviation, s_R = 0.009729 V

4.4.1 Assessment of Mandel's k statistics

The results of within-cell consistency are shown in Figure 4.3, the k-values for each test cell are grouped by the operating conditions. The horizontal dashed lines represent the critical k-values, which are used to test whether the standard deviation of each test cell's results is sufficiently different from the other test cells. The red dashed line means that the critical value was obtained based on the significant level of 1%, and the critical values for the black dashed line were based on a significant level of 5%.

In Figure 4.3a), part of the k-values from test cell 2 and test cell 3 are standing outside the k critical lines. For test cell 2, the k-value is higher than the 5% critical value at A1-2, and it also exceeds the 1% critical line at A2-2. For test cell 3, the k-values at A1-4, A3-3 and A3-4 all exceed the 1% critical line.

In Figure 4.3b), the k-value from test cell 3 in B1-1 far exceeds the 1% critical line, which is caused by a big fluctuation of the cell voltage in B1-1 (see details in Appendix A.5), severe liquid water flooding occurred during this period.

In Figure 4.3c), only the k-value from test cell 1 in C1-3 is found to be higher than the 1% critical value. This can be contribute to that the high operating temperature (80°C) and the low cathodic relative humidity (30%) cause the smallest amount of liquid water in the flow channel and so as the small voltage oscillation.

Generally speaking, the cases of the k-value that exceed the 1% critical k-value are mostly observed in A1-4, A3-4, B1-4, B2-4 and B3-4, where the current density is highest (1.0 A/cm^2) in these regions. The highest current density can generate the highest amount of water, and the operating conditions of A*-* and B*-* will make the voltage oscillation more severe. Overall, this type of test cell can provide a good level of precision in most of the operating conditions.
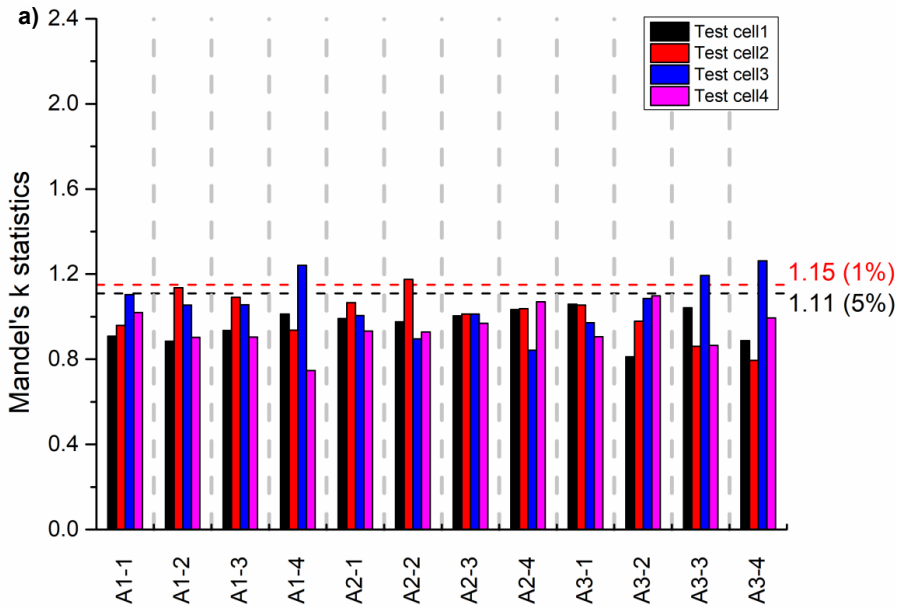
Figure 4.3 a): Results at operating conditions from A1-1 to A3-4.
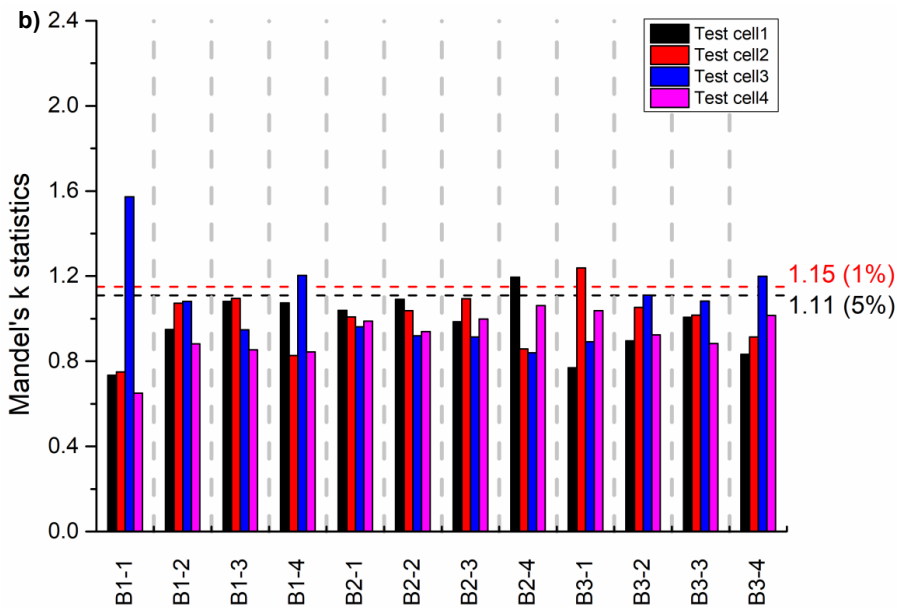
Figure 4.3 b): Results at operating conditions from B1-1 to B3-4.
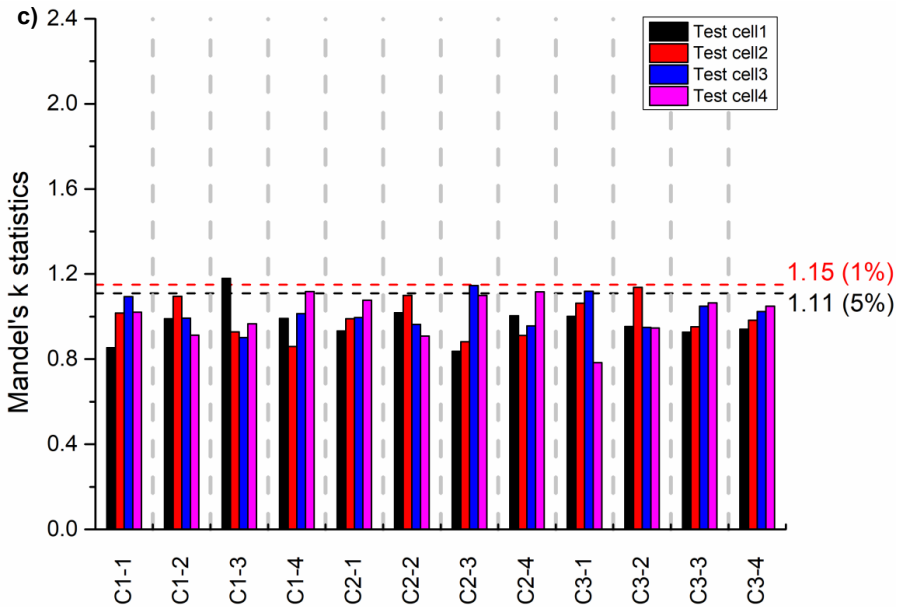
Figure 4.3 c): Results at operating conditions from C1-1 to C3-4.

Figure 4.3: The Mandel's k statistics graphics at different operating conditions.

4.4.2 Assessment of Mandel's h statistics

The results of the between-cell consistency are shown in Figure 4.4, the h-values for each test cell are grouped by the operating conditions. Two groups of horizontal dashed lines represent the corresponding critical h-values. The red lines indicate that the critical values are obtained based on a significance level of 1%, and the critical values for the black lines are based on a significance level of 5%. Three general patterns were observed in each graph, which are: Pattern 1, the test cell has positive h-values for all operating conditions, such as test cell 4; Pattern 2, the test cell has negative h-values for all operating conditions, such as test cell 3; and Pattern 3, the test cell has either positive or negative h-values, such as test cell 1 and test cell 2. It can be noticed that the h-values of test cell 1 and test cell 2 are close to each other and smaller than that of test cell 3 and test cell 4, which means that their results have a higher level of trueness. The h-values of test cell 3 and test cell 4 appear to be markedly different from each other, and part of the h-values from these two test cells are standing outside the critical h-values. The h-values of the A3-1, A3-3 and C3-1 from test cell 3 are higher than its 5% critical value. For test cell 4, the h-value at B2-3 is higher than its 5% critical value, and at B2-4 is higher than the 1% critical value. Nonetheless, they remain within the region of reasonable consistency. Overall, the

results indicate that a high level of the trueness of the test results can be obtained from this type of test cells at the most operating conditions.
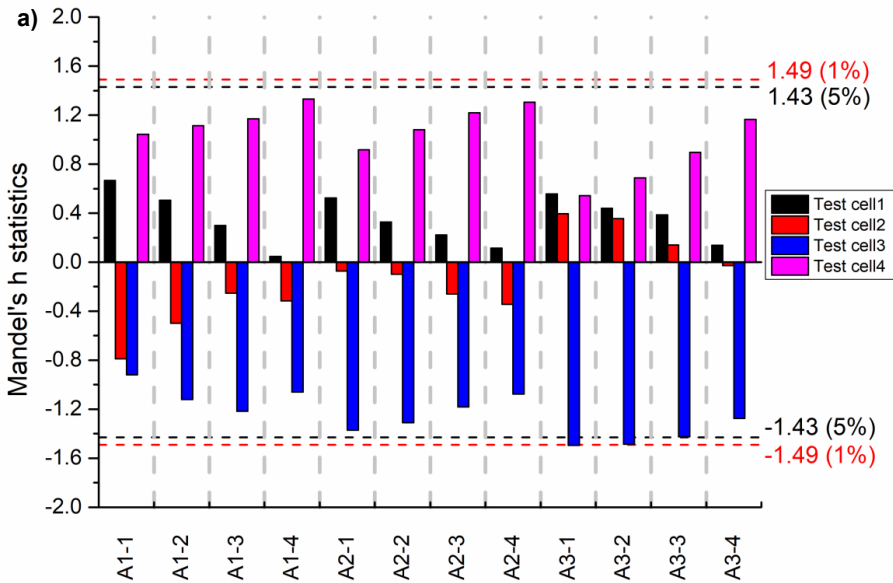
Figure 4.4 a): Results at operating conditions from A1-1 to A3-4.
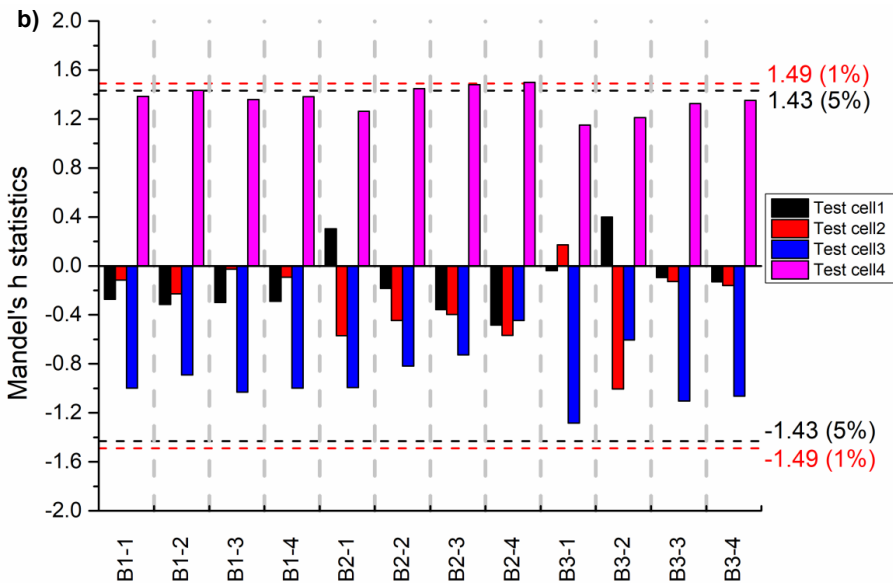
Figure 4.4 b): Results at operating conditions from B1-1 to B3-4.
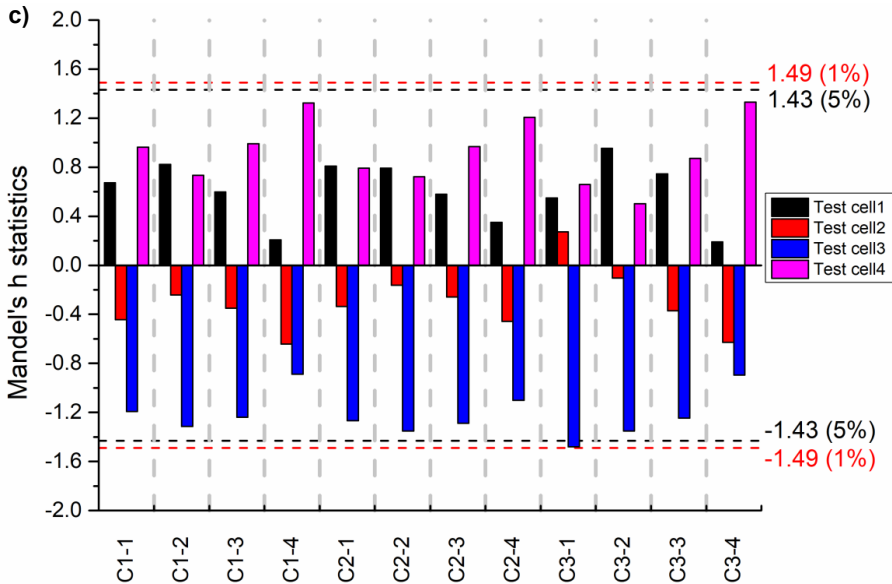
Figure 4.4 c): Results at operating conditions from C1-1 to C3-4.

Figure 4.4: The Mandel's h statistics graphics at different operating conditions.

4.4.3 Assessment of the repeatability and reproducibility

Figure 4.5 shows the repeatability standard deviation (S_r) and reproducibility standard deviation (S_R) of the test cells under different operating conditions. In accordance with the different operating conditions, the entire graph can be divided into three parts. Part 1 contains the standard deviations obtained from A1-1 to A3-4. After a slight decrease from A1-1 to A1-2, the red S_R line increases sharply and reaches a peak at A1-4. A similar trend for the S_R line was also observed from A2-1 to A2-4 and A3-1 to A3-4. The changes of the S_r line are similar to those of the S_R line. The current density applied to the test cell was increased from A1-1 to A1-4 (and also for A2-1 to A2-4, A3-1 to A3-4), the higher current densities lead to higher amounts of generated water in the test cell, which can lead to a higher repeatability and reproducibility standard deviation.

By comparing the S_r and S_R values between A1-*, A2-* and A3-*, it is observed that the lowest value is found in A2-*, the middle value is found in A1-* and the highest value is found in A3-*. The reason is that the A2-* has the highest stoichiometry ratio on the cathode side, which can blow away the excess liquid water during the cell operation and reduce the fluctuation of the test results. It was also found that the line trend shown in part 2 and part 3 is just as similar as in part 1. It can be concluded that the

repeatability and reproducibility of the test cell are more sensitive to the stoichiometry ratio and current density compared to temperature and relative humidity.

4.5   Summary

An accuracy study of the in-house-assembled LT-PEFC was carried out with the aim of evaluate the test cell's trueness and precision. Four test cells were assembled and tested. The results indicate that the test cell is characterized by a high level of accuracy, and the repeatability and reproducibility of the test cell can be influenced by the operating conditions, especially sensitive for the factors such as stoichiometry ratio and current density.
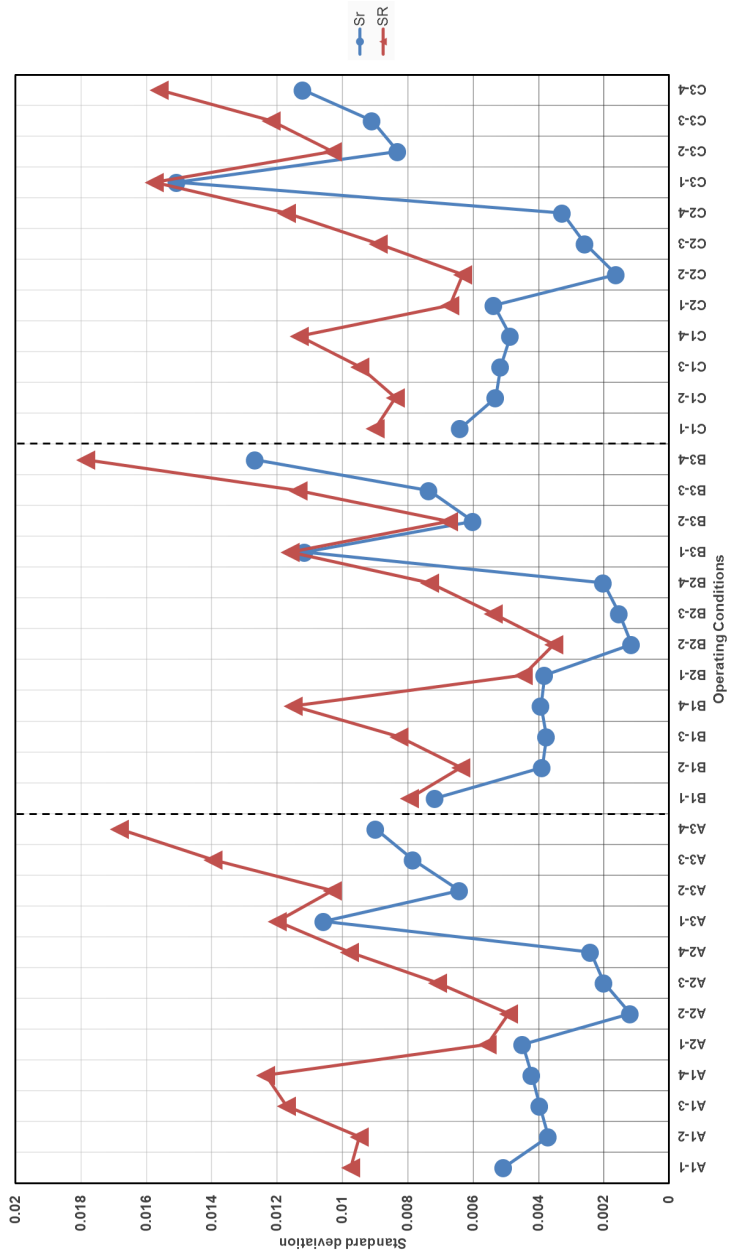
Figure 4.5: The repeatability (S_r) and reproducibility (S_R) standard deviation versus operating conditions.

4 Accuracy study of the test cell performance

5 Static behavior study of in-house assembled LT-PEFC

This chapter presents the characterization of the effects of different operating conditions on the static behavior of the in-house designed LT-PEFC via the Design of Experiments (DoE) methodology, with the aim to evaluate the most important operating conditions (factors) for the LT-PEFC to reach optimum performance in the selected operating ranges. Because of the hard-to-change factors present in the selected operating conditions, a fully randomized operation under the DoE method will become unrealistic and may lead to misleading results. Thus, the Split-plot Design method which is based on the DoE was applied in the research.

5.1 Experimental design method

The early planning stage is the crucial element in applying the DoE successfully to an experiment [147]. The key steps in the planning stage are selecting relevant factors and also quantifying their operating ranges and further determining their operating levels [148]. The detailed selection process of the factors and responses is presented in the following sections. As a brief recap, the term 'factor' refers to the input variable, such as reactant relative humidity, fuel cell temperature, etc. The term 'response' refers to the output variable, such as voltage, pressure drop, etc.

5.1.1 The factor selection

Due to the characteristics of the LT-PEFC, the water problem has always been a critical issue during its operation. Appropriate water management strategies can enable fuel cells to operate with high performance and long durability. Apart from the modification of the fuel cell and its components such as flow field, MEA and GDL, etc., adjusting and modifying the operating conditions of the fuel cell is also a promising water management strategy, which is widely used in both laboratories and industry areas [73]. Various parameters are included in the typical operating conditions, which are the stoichiometric ratios on the anode and cathode side, the relative humidities on the anode and cathode side, the operating pressure and the operating temperature. The selection of the ranges for these parameters is based on the literature, guidance from manufacturers and experience on the in-house designed single test cell operations. Typical test cell temperature is around 70°C, with fully saturated hydrogen at a stoichiometric ratio of 1.2, and fully saturated air at 2.5 [135]. The temperature range in this DoE experiment is set at 50-70°C; the range of relative humidity is 50-90%. Extreme conditions, such as high temperatures (above 70°C) with low relative humidity (below 50%); or low temperatures (below 50°C) with high relative humidity (above

90%), were not considered. The reason is that such extreme conditions could cause damage to the MEA and make it impossible to conduct the entire experiment. The range of the stoichiometric ratio on the anode side is set at 1.5-3.5. At the cathode side, it is 2.5-4.5. The backpressure applied on both anode and cathode sides is at 0-100 kPa. The orientation of the test cell is quantified to 0°, when the cathode side is oriented horizontally under the anode side; and to 180°, when the cathode side is oriented horizontally above the anode side.

The factor code, the name, the operating ranges and the factor type are summarized in Table 5.1. Seven numeric factors and two levels for each factor were determined during the planning phase of this DoE experiment. A large amount of time is required to change from low level to high level for the factors of cell orientation and temperature, so these two 'hard-to-change parameters' are considered as whole-plot factors in the split-plot design, which are represented by the lower case letters a and b. The remaining factors are considered as sub-plot factors, which are represented successively by the upper case letters from C to G.

Table 5.1: Selected factors and their ranges.

Factor Code	Factor	Unit	Range	Factor type	Factor rule in SPD
a	Cell orientation	°	0-180	Numeric	Whole-plot factor
b	Temperature	°C	50-70	Numeric	Whole-plot factor
C	Anode Stoi.		1.5-3.5	Numeric	Sub-plot factor
D	Cathode Stoi.		2.5-4.5	Numeric	Sub-plot factor
E	Anode R.H.	%	50-90	Numeric	Sub-plot factor
F	Cathode R.H.	%	50-90	Numeric	Sub-plot factor
G	Backpressure	kPa	0-100	Numeric	Sub-plot factor

5.1.2 The response selection

After the parameters and their ranges are determined, the next step is to select the appropriate responses. Some researchers [82,120,149,150] choose maximum power density as the response from the perspective of fuel cell vehicular applications.

However, the speed of the vehicle will be frequently changed at different conditions, especially in urban areas. Consequently, the voltage response at different current density points, as well as pressure drop response was studied in this test.

5.1.2.1 Voltage and voltage oscillation response

As covered in the literature review part, the polarization curve can be used to characterize the test cell performance. The major losses of a fuel cell can be divided into three parts, which are: activation loss, ohmic loss and mass transport loss [19]. It can be noted that the activation loss is dominating at the lower current density regime, the ohmic loss is dominating at the middle current density regime and the mass transport loss is dominating at the higher current density regime. Hence, the corresponding voltages at the current density of 0.2 A/cm^2 (low current density), 0.6 A/cm^2 (middle current density), 1.0 A/cm^2 (high current density) and 1.2 A/cm^2 (extreme current density) were recorded in this DoE experiment. Furthermore, differing operating conditions can also affect the voltage stability during cell operation. So, the voltage oscillation response calculated by the standard deviation of the voltage value was also recorded to analyze the voltage stability at each current density.

5.1.2.2 Pressure drop response

The pressure drop inside fuel cells has been used as an effective tool to analyze the water issue in channels [55][151]. For the triple serpentine flow field used in the in-house designed fuel cell, the pressure drop value is primarily influenced by the properties of the reactants and flow channels, as well as the friction between them [152]. When liquid water is introduced into the flow channel, the velocity of the reactants will be increased, which will affect the frictional coefficient and hence the pressure drop in the channel will increase. The higher the water amount in the channel, the higher the pressure drop will be [153]. The pressure drop at the cathode side was chosen as one response owning to that the water is generated on the cathode side, it is more likely to have the flooding issue compared to the anode side. The selected responses are summarized in Table 5.2.

Table 5.2: Selected Responses

Response	Unit
Voltage	mV
Voltage oscillation	mV
Cathodic pressure drop	mbar

5.2 Experimental setup

The operating conditions used in this DoE experiment are shown in Table 5.1. Experiments were performed to study the effect of the test cell orientation in the range of 0-180°, the test cell temperature in the range of 50-70°C; the anodic stoichiometric ratio in the range of 1.5-3.5 and the anodic relative humidity of 50-90%; the cathodic stoichiometric ratio in the range of 2.5-4.5 and the cathodic relative humidity of 50-90%; the backpressure in the range of 0-100 kPa. With the aid of DoE software (Design Expert trail version by Stat-Ease, Inc), a total number of 256 tests were created at four current density points (0.2 A/cm², 0.6 A/cm², 1.0 A/cm² and 1.2 A/cm²), 64 runs for each current density point. According to the principle of two-level factorial design [147], the number of tests for each current density should be originally 128 (2^7=128, with 2 levels and 7 factors). In order to increase the efficiency of the experiment and reasonably reduce the experimental effort, the fractional factorial split-plot design method was applied. The number of tests per current density value was then reduced from 128 to 64 and with a resolution level of VI, which means that the estimations of main factor effects are not confounded with four-factor interactions. A total of 256 tests (corresponding to four current densities) were run in a random order to avoid influence from systematic disturbances. A purge procedure was performed between the tests to eliminate the historical influence. During the testing process, the response of the voltage and cathodic pressure drop was recorded within a period of 180 s at each current density The voltage standard deviation over this period was recorded as the voltage oscillation response.

5.2.1 Experimental apparatus

The detailed configuration of the test station and the test cells were described in chapter 3. Figure 5.1 shows the test cell orientation at 0 and 180°. During the cell operation, the humidified reactants were introduced into the test cell. It is noteworthy that during this process, liquid water may be condensed in the inlet port and the outlet port on both the anode and cathode sides of the test cell, which has a significant adverse effect on a cell's performance.

An example of this failure situation is illustrated in Figure 5.2. The test cell was operated at 70°C, with 90% relative humidity on both sides, the stoichiometric ratio on the anode side is 1.2, and the cathode side is 2.5. It can be observed that without control of the temperature at the inlet and outlet tube, the cell performance decreases dramatically. In test 1, the cell performed well at the beginning. Then the voltage starts to decrease when the current density exceeds 0.4 A/cm². In test 2, the voltage was

reduced dramatically even at a small current density. It may be caused by the liquid water condensated in the inlet or outlet port during the process of test 1. A short purge procedure was performed between test 2 and test 3. It was observed that in test 3, the polarization curve showed good performance in the low current density regime, however, the voltage still decreases dramatically at around 0.2 A/cm^2.

As a solution, the electric heating tape (marked in Figure 5.1a) from WINKLER AG was used to cover the surface of the inlet and outlet tube on both anode and cathode sides. Therefore, the inlet and outlet tube temperature can be controlled at a specific temperature (usually test cell temperature) to avoid any liquid water condensation. The insulation material was also used to cover the heating tape and inlet/outlet tube, which can reduce the heat exchange with the ambient, and thus reduce the temperature fluctuations in this area.
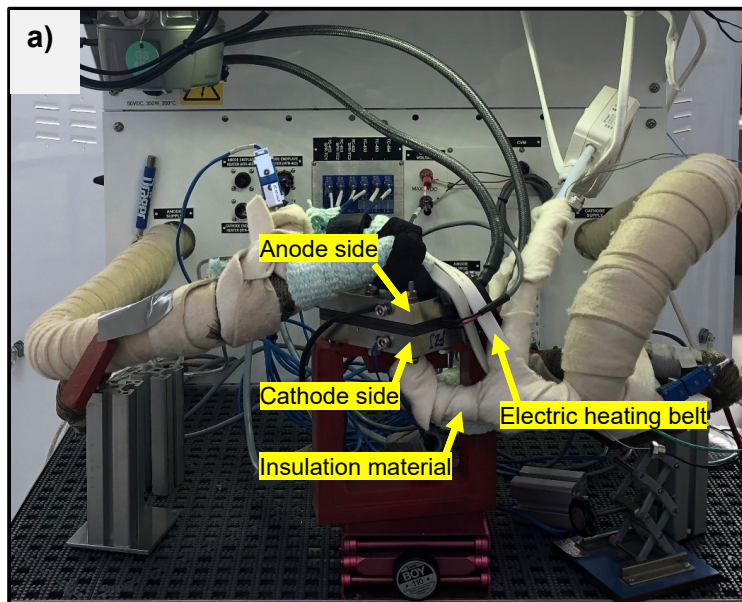
Figure 5.1 a): The cathode side is oriented horizontally under the anode side: 0°.
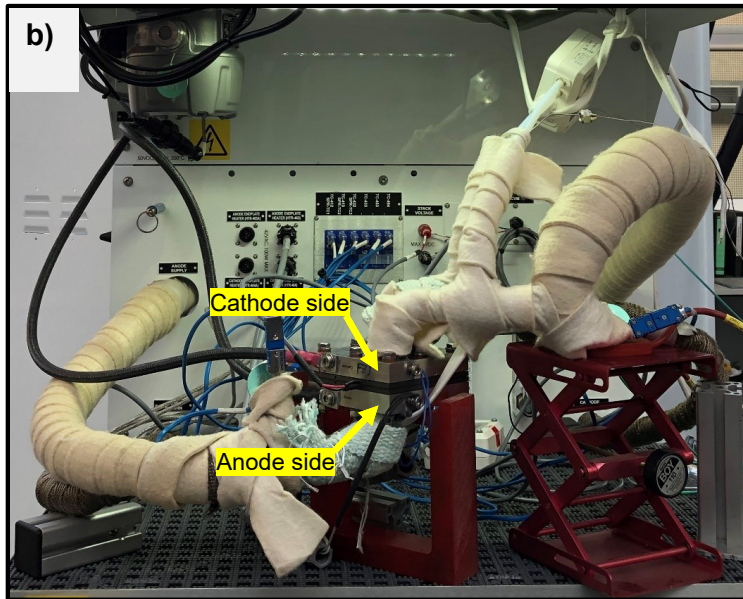
Figure 5.1 b): The cathode side is oriented horizontally above the anode side: 180°.

Figure 5.1: The test cell orientation at 0° and 180°.
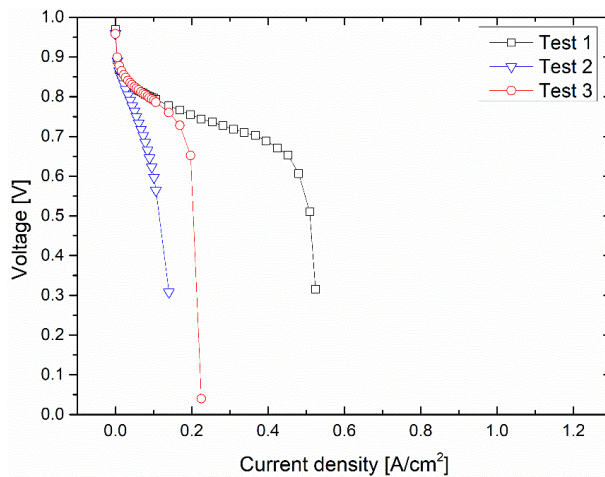
Figure 5.2: Test 1, Test 2 and Test 3 were performed without control of the temperature at the inlet and outlet tube. Test 2 was performed immediately after test 1. Test 3 was performed after a purging procedure.

5.3 DoE study results and discussion

5.3.1 Results of linear regression models

The linear regression models for the targeted responses were generated according to the results of the two-level factorial split-plot design. Two types of model can be used to represent the results of split-plot design, which are the coded factor model and the actual factor model. Both of them can be used to predict the targeted response value. In the coded factor model, the high and low levels of each coded factor are assigned to +1 and -1. However, in the actual factor model, these dimensionless coded factors are transformed into the actual factors with units, the coefficients of each term in the actual factor equation are scaled to fit the unit of the actual factor. Thus, the actual factor equation cannot be used to make a relative impact comparing with each factor based on their coefficients. So, the coded factor model was used in the analysis part. The voltage response model, the pressure drop response model and the voltage oscillation response model are illustrated in Table 5.3, Table 5.4 and Table 5.5, respectively.

5.3.1.1 The voltage response regression model

The regression models for the voltage response at different current densities (0.2 A/cm^2, 0.6 A/cm^2, 1.0 A/cm^2 and 1.2 A/cm^2) are shown in Table 5.3. In the first model, for the voltage at 0.2 A/cm^2, the factor b (Temperature), D (Cathode stoi.), G (Backpressure) and the interaction between b and G are statistically dominant among all factors. For the second model, which describes the voltage at 0.6 A/cm^2, apart from all significant factors in model 1), the interaction term bD is also included in model 2). The additional significant factor DG was added in model 3). In model 4), which describes the voltage at 1.2 A/cm^2, a new main factor F (Cathode R.H.) is added to the model. Overall, it is evident from the statistical model that more factors are relevant for the voltage response model at higher current densities owning to that a higher current density can cause a more complicated situation in the test cell.

Table 5.3: The voltage response regression model. (a: Cell orientation, b: Temperature, C: Anode stoi., D: Cathode stoi., E: Anode R.H., F: Cathode R.H., G: Backpressure)

1) Voltage @0.2 A/cm^2 =	2) Voltage @0.6 A/cm^2 =	3) Voltage @1.0 A/cm^2 =	4) Voltage @1.2 A/cm^2 =
+788.36	+695.95	+602.49	+559.18
+5.06 b	+14.01 b	+36.25 b	+43.68 b
+1.79 D	+6.87 D	+25.57 D	+34.64 D
+13.96 G	+15.99 G	+6.90 G	-5.39 F
+1.88 bG	-2.04 bD	-10.64 bD	+7.38 G
	+2.49 bG	+13.55 bG	-13.63 bD
		+5.07 DG	+14.36 bG

The selection of the significant terms in the voltage model

The relevant factors in these models were chosen due to their statistically significant effect on the corresponding response. Figure 5.3 presents the Pareto charts of the voltage regression model at different current densities. The Pareto chart can be considered as an effective graphical tool to determine which factors and their interactions are significant enough to be used in a regression model. The t-value limit and the Bonferroni limit, shown in Figure 5.3, are presented as the criterion for the significant factor selection. The lower one, the t-value limit, was calculated based on the standard critical t value with a significance level of 5%. The upper one, the Bonferroni limit, was calculated based on the "family-wise" corrected critical t value with a significance level lower than 5%., which is more stringent than the standard t-value limit [145]. The factors that exceed the t-value limit or the Bonferroni limit, as the open bars are shown in Figure 5.3, are selected as significant factors and can be added to the regression model. The factor in orange/blue represents a positive/negative effect on the targeted response.

Figure 5.3a, 5.3c, 5.3e and 5.3g represent the subplot effects that include factors C (Anode Stoi.), D (Cathode Stoi.), E (Anode R.H.), F (Cathode R.H.), G (Backpressure), the interaction between these subplot factors, as well as the interaction between subplot factors and whole-plot factors. Figure 5.3b, 5.3d, 5.3f and 5.3h represent the whole-plot effects that only include whole-plot factors a (Cell orientation), b (Cell temperature) and their interaction factor ab.

Subplot Effects

Whole-plot Effects
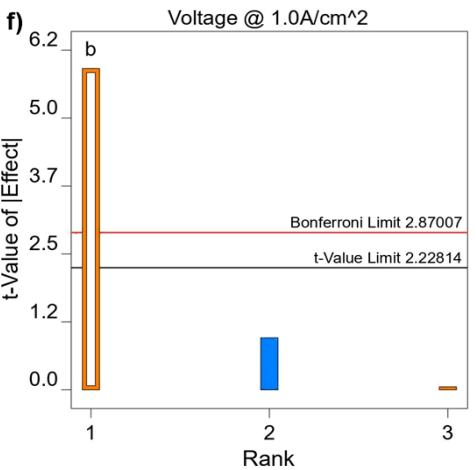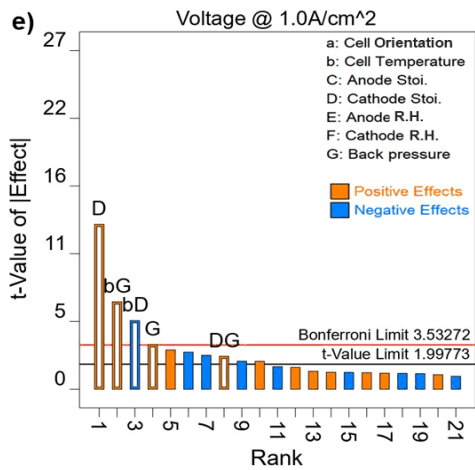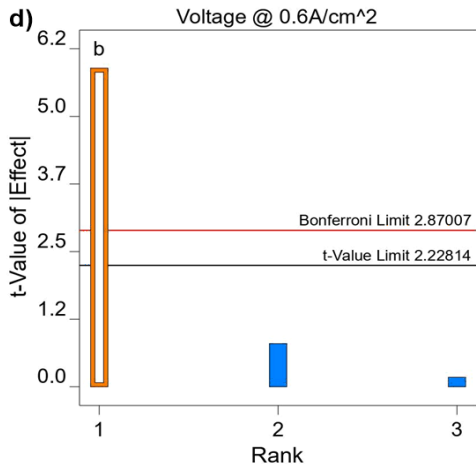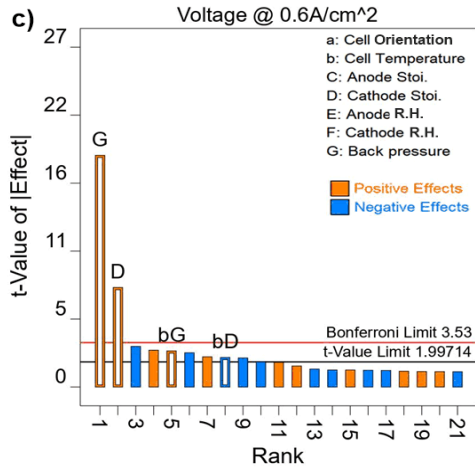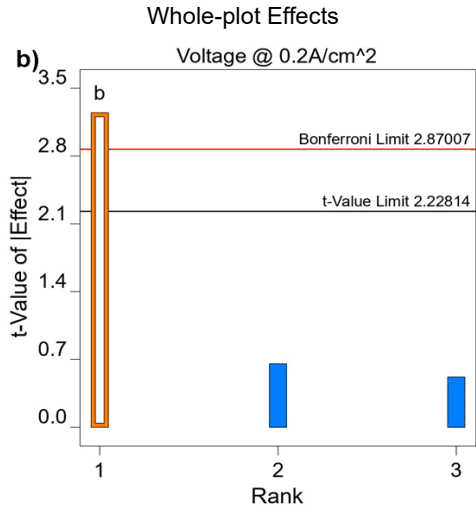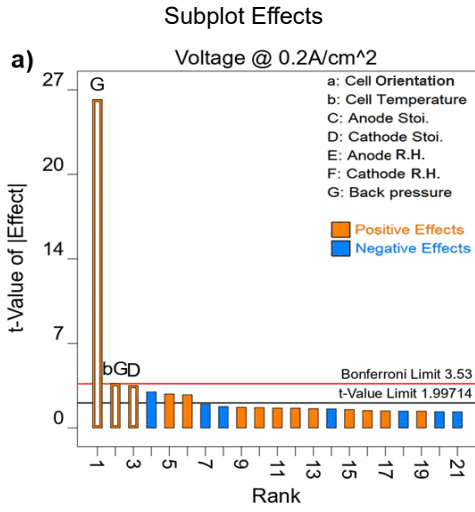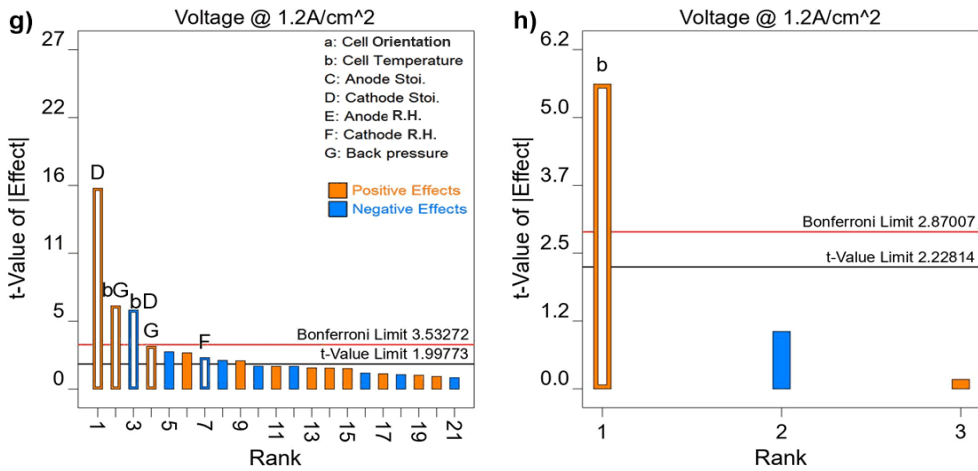
Figure 5.3: Pareto charts for voltage response model at the current densities of 0.2 A/cm^2, 0.6 A/cm^2, 1.0 A/cm^2, 1.2 A/cm^2.

It can be observed in Figure 5.3 that the most relevant factors on voltage response are factor b (Temperature), D (Cathode stoi.), G (Backpressure) and their interactions. In Figure 5.3a, for the voltage response at a current density of 0.2 A/cm^2, the significant factors are ranked in the order of G, bG, D. All of them have positive effects on the test cell voltage. The factor G, backpressure, has the highest impact compared to others. The higher pressure can effectively increase the partial pressure of oxygen, thereby increasing the voltage of the test cell. Figure 5.3c shows, when the current density is increased to 0.6 A/cm^2, the effect of factor D, Cathode stoi., on the voltage is enhanced. At a higher current density, more water will be generated on the cathode side, so the cathode stoichiometric ratio is gradually increasing its influence on the test cell voltage. The bD interaction is also significant enough to be added to the model, which has a negative effect on the cell voltage. The reason might be that at a higher temperature, more liquid water in the test cell will be evaporated into water vapor. The increased stoichiometric ratio under this condition will have a drying effect on the membrane, consequently lowering the cell voltage. Figure 5.3e shows that when the current density is increased to 1.0 A/cm^2, the effect of factor D, Cathode stoi., on voltage is dramatically enhanced. Currently, factor D is at rank 1 and factor G is at rank 4. It is reasonable that at 1.0 A/cm^2, more liquid water was generated on the cathode side than at 0.6 A/cm^2, the mass transport limitation controls the cell voltage now. The cathode stoichiometric factor becomes dominant under this condition. The interaction between D (Cathode Stoi.) and G (Backpressure) is additionally added to the model. Higher stoichiometry can flush out more liquid water, and higher pressure can

significantly increase the oxygen partial pressure. A combination of these two factors at their high levels will positively affect the cell voltage. Figure 5.3g shows the voltage regression model at the current density of 1.2 A/cm^2. The significant rank order of factors D, bG, bD and G are the same as those in Figure 5.3e. A new factor F, cathode relative humidity, is also observed in the model, which negatively affected the voltage of the test cell. It is readily understood that at such high current densities, more liquid water will be present in the pores of the catalyst layer, gas diffusion layer and the flow channels on the cathode side. A high cathode side relative humidity will introduce more water vapor into the test cell. It will, therefore, increase the risk of liquid water flooding on the cathode side, which will adversely affect proper water management.

In Figure 5.3b, 5.3d, 5.3f and 5.3h, the whole-plot factor b, test cell temperature, is significant for all regression models. However, the factor a, cell orientation, and the interaction between cell orientation and temperature, factor ab, are not considered to be significant in any of the regression models, which is out of the expectation. It is also noted that factors at the anode side, as anode stoichiometry ratio and relative humidity, are not considered significant for all current densities. The reason might be that the effects of the anode side parameters do not have a noticeable effect on the performance of the test cell in their selected operating ranges. It is also noteworthy that the interaction of three factors or higher orders almost does not exist in a practical system and can be safely ignored during the significance factor selection process [82]. This is also the reason that some factors are even higher than the t-value limit, but still not included in the regression model. An example can be found in Appendix A13.

The validation of the voltage regression model

Two residual assumptions are used to examine the validity of the fitted regression model: (1) Residuals are normally distributed, and (2) Residuals are independent of each other. Residuals are calculated by the difference between the measured value of each test and its corresponding predicted value obtained by the regression model. The plots about these two assumptions are shown in Figure 5.4. Note that points in Figure 5.4 are color-coded by the different values of responses. From blue point for the lowest value to red point for the largest value. Figure 5.4a, 5.4c, 5.4e and 5.4g represent the normal plot of residuals of the voltage response model at current densities of 0.2 A/cm^2, 0.6 A/cm^2, 1.0 A/cm^2, 1.2 A/cm^2 respectively. Abscissa terms in the plot are referred to as external studentized residuals, which are the standard deviation of each raw individual residuals from the residual mean value. Using external studentized residuals rather than raw residuals can improve the detection capacity of the abnormality. The

ordinate of the plot is the specified theoretical distribution of each residual. The residuals that follow the normal distribution should be located on the 45° straight line (red line in Figure 5.4a, 5.4c, 5.4e and 5.4g). However, it should be noted that it does not mean that each point must be located on that line perfectly; a mild violation is acceptable. It is observed that the residual of each regression model follows a normal distribution, which indicates that data is fitted well in the regression model. Figure 5.4b, 5.4d, 5.4f and 5.4h represent the plot of the residuals versus the test run order at different current densities. It can be concluded from these figures that the residuals are independent of each other, and that there is no specific residual pattern observed in each plot. Overall, both of the assumptions are not violated, indicating that the model is nicely validated.
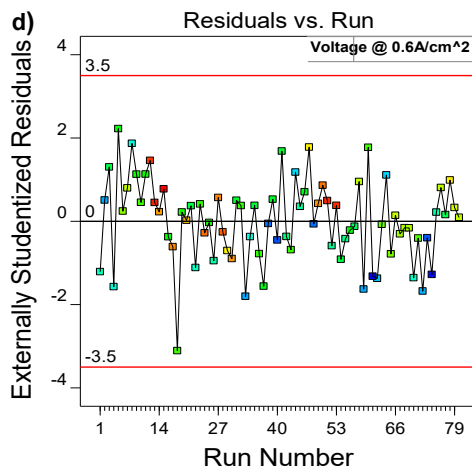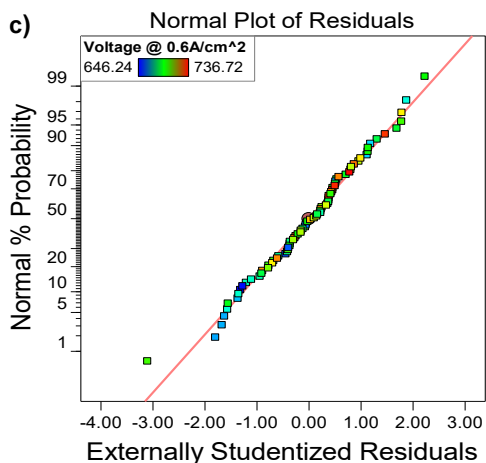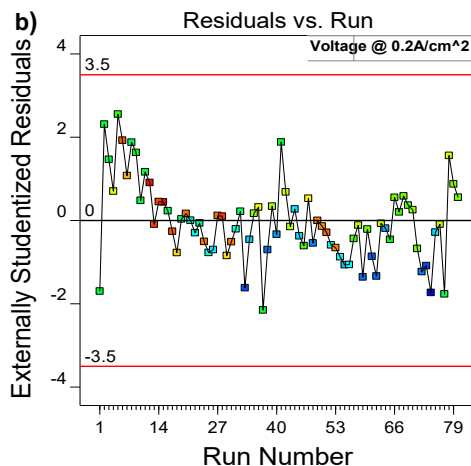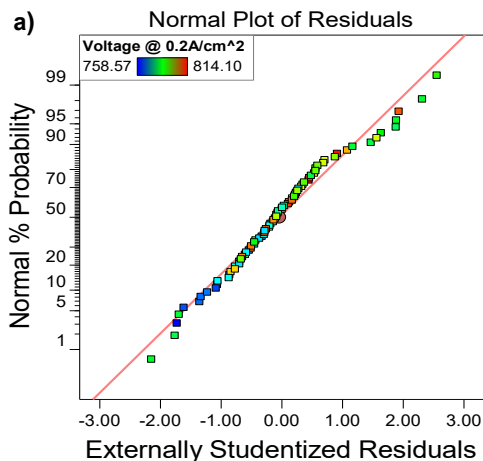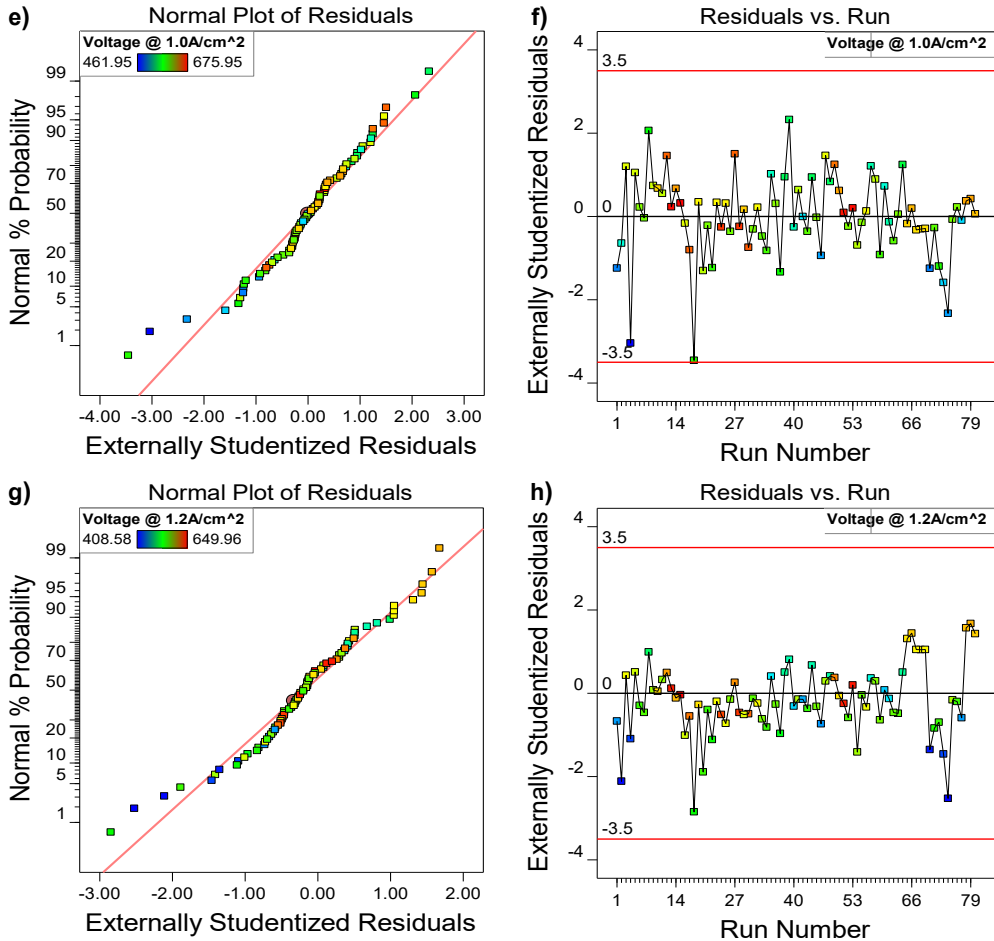
Figure 5.4: Normal plot of Residuals and Residuals vs. run order for voltage response at current densities of 0.2 A/cm², 0.6 A/cm², 1.0 A/cm², 1.2 A/cm².

5.3.1.2 The pressure drop response regression model

Table 5.4 shows the regression model of the pressure drop response at current densities of 0.2 A/cm², 0.6 A/cm², 1.0 A/cm² and 1.2 A/cm². In the pressure drop regression model at the current density of 0.2 A/cm², factor D (Cathode stoi.), G (Backpressure) and the interactions between D and G are statistically significant compared to other factors. The chosen factors in the second pressure drop regression model, factor D, factor G and the interaction factor DG are included in the model, which is just the same as those in the first regression model. The additional significant factor F (Cathode relative humidity) and the interaction factor FG are added in model 3). In the pressure drop regression model 4) at a current density of 1.2 A/cm², factor b

(temperature) and the interaction factor bD and bG are additionally added to the model. Similar to the voltage regression model, more factors are added to the pressure drop regression model at higher current densities.

Table 5.4: The pressure drop response regression model at different current densities. (a: Cell orientation, b: Temperature, C: Anode stoi., D: Cathode stoi., E: Anode R.H., F: Cathode R.H., G: Backpressure)

1) Pressure drop @0.2 A/cm² =	2) Pressure drop @0.6 A/cm² =	3) Pressure drop @1.0 A/cm² =	4) Pressure drop @1.2 A/cm² =
+4.01	+14.97	+26.54	+32.32
+1.26 D	+4.26 D	+8.47 D	+1.08 b
-0.9507 G	-3.04 G	+1.12 F	+10.70 D
-0.3190 DG	-0.6547 DG	-6.27 G	+1.44 F
		-1.99 DG	-8.10 G
		-0.5816 FG	+0.7559 bD
			-0.6824 bG
			-2.87 DG
			-0.6776 FG

The significant terms in the pressure drop model

Four sets of Pareto charts in Figure 5.5 were used to interpret the choices of the significant factors of the pressure drop regression models. It can be observed in Figure 5.5 that the most significant factors at low and middle current densities are factors D (Cathode Stoi.) and G (Backpressure). The factors F (Cathode R.H.) and b (Cell temperature) are additionally significant at higher current densities.

Based on Hagen-Poiseuille's equation, Li et al. [154] proposed an empirical equation for the single phase pressure drop calculation, as shown in Equation 5.1. They take the channel geometry, the operating parameters and the moist air into consideration. This equation can be used to calculate the pressure drop in serpentine or parallel channels.

$$\Delta p = 1.15 \times 10^{-11} \frac{L}{nAD_h^2} \frac{RT^{1.632}}{P_a - \phi P_{sat}} Q_v \qquad 5.1$$

where:

T: test cell temperature,

L: length of the flow channel,

D_h: hydraulic diameter of the flow channel,

A: cross-section area of the flow channel,

R: the gas constant,

P_a: mixture inlet pressure,

ϕ: mixture relative humidity,

P_{sat}:   saturation pressure,

Q_v: mixture volume flow rate.

According to Equation 5.1, the pressure drop is not only related to the geometry of the flow channel (L, n, A and D_h), but also related to the fuel cell operating conditions (T, ϕ, and P_a). Test cell temperature (T) and operating pressure (P_a) will influence the mixture viscosity, and the stoichiometry ratio is also directly related to the mixture volume flow rate (Q_v). This is consistent with the chosen significant factors in pressure drop regression models. A detailed derivation of Equation 5.1 is illustrated in Appendix A.6.

In Figure 5.5a, the pressure drop response at the current density of 0.2 A/cm^2, the significant factors are ranked in the order of D, G, DG. Factor D has a positive effect on cathode pressure drop, while factors G and DG have negative effects on cathode pressure drop. According to Equation 5.1, a higher cathode stoichiometry ratio will lead to a higher volume flow of the reactants, and therefore a higher pressure drop. Higher backpressure will cause a lower pressure drop value. The chosen significant factors in Figure 5.5c are just the same as those in Figure 5.5a. Figure 5.5e shows that in addition to factors D, G, DG, the factor F (Cathode R.H.) is also added to the model. Factor F has a positive effect on the pressure drop. At high current density, a high cathode relative humidity may introduce more liquid water into the flow channel, which will cause a higher pressure drop value. In Figure 5.5g, the current density was set to 1.2 A/cm^2, the temperature (factor b) is additionally added to the pressure drop regression model. It is in accordance with Equations A.19 and A.20 (In Appendix) that a temperature change will also cause a change in reactant viscosity and density, so as followed by a pressure drop value. The pressure drop regression models are well validated and detailed information can be found in Appendix A.7.

Subplot Effects

Whole-plot Effects

a) Pressure drop @ 0.2A/cm^2

b) Pressure drop @ 0.2A/cm^2

c) Pressure drop @ 0.6A/cm^2

d) Pressure drop @ 0.6A/cm^2

e) Pressure drop @ 1.0A/cm^2

f) Pressure drop @ 1.0A/cm^2
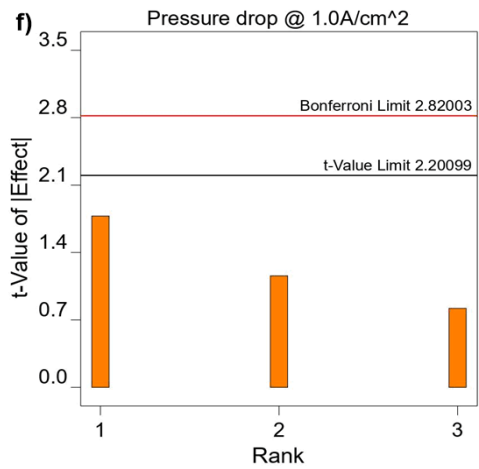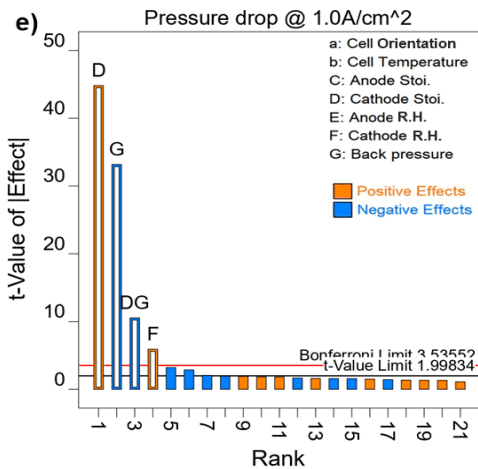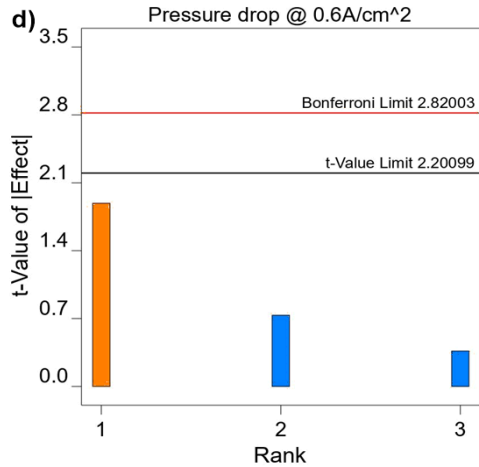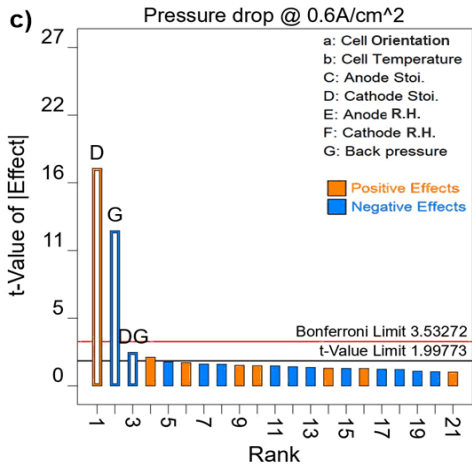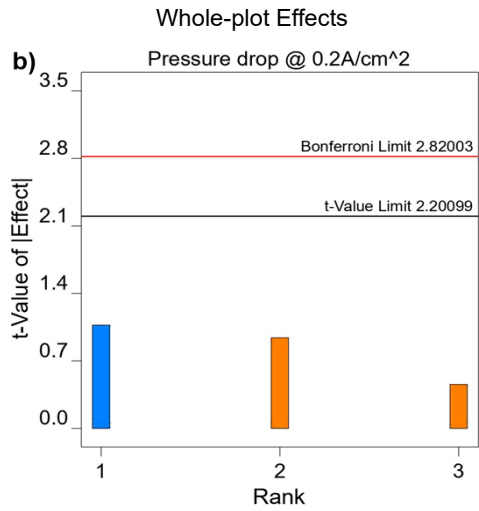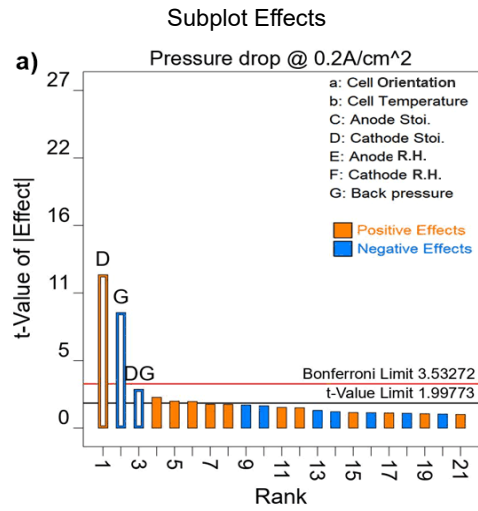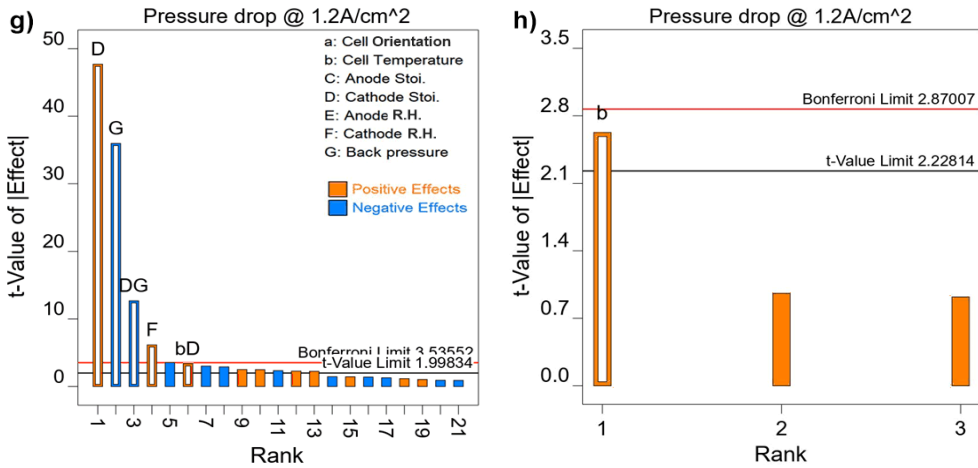
Figure 5.5: Pareto charts for the pressure drop response model at the current densities of 0.2 A/cm^2, 0.6 A/cm^2, 1.0 A/cm^2, 1.2 A/cm^2.

5.3.1.3 The voltage oscillation response regression model

Table 5.5 shows the regression model of the voltage oscillation response at different current densities (0.2 A/cm^2, 0.6 A/cm^2, 1.0 A/cm^2 and 1.2 A/cm^2). In the first voltage oscillation regression model at 0.2 A/cm^2, factor D (Cathode stoi.), G (Backpressure) and the interactions between D and G are statistically significant compared to other factors. For the second model, with voltage oscillation at 0.6 A/cm^2, apart from all significant factors in model 1), factor b (temperature) is also included in model 2). The chosen factors b, D, G and the interaction factor DG are included in model 3), which are just the same as those factors in the second regression model. The significant factor F (Cathode R.H.) is added additionally in model 4). Similar to the voltage and pressure drop regression model, the higher the current density, the more factors are involved in the voltage oscillation regression model.

Table 5.5: The voltage oscillation response regression model at different current densities. (a: Cell orientation, b: Temperature, C: Anode stoi., D: Cathode stoi., E: Anode R.H., F: Cathode R.H., G: Backpressure)

1) Voltage oscillation = @0.2 A/cm^2	2) Voltage oscillation = @0.6 A/cm^2	3) Voltage oscillation = @1.0 A/cm^2	4) Voltage oscillation = @1.2 A/cm^2
+1.00	+1.37	+2.60	+3.12
-0.3859 D	-0.4124 b	-0.9801 b	-1.45 b
+0.3653 G	-0.5887 D	-1.35 D	-1.62 D
-0.2861 DG	+0.2819 G	+0.6520 G	+0.4275 F
	-0.3294 DG	-0.4912 DG	+0.5852 G

The significant terms in the voltage oscillation model

It can be observed in Figure 5.6 that the most significant main factors at a low current density (0.2 A/cm^2) are factor D (Cathode stoi.) and G (Backpressure). Factor b (Cell temperature) is additionally added in the model at a medium current density (0.6 A/cm^2), and factor F (Cathode R.H.) is included in the model at a very high current density (1.2 A/cm^2).

In Figure 5.6a, the voltage oscillation response at a current density of 0.2 A/cm^2, the significant factors are ranked in the order of D, G, DG. Factor D (Cathode stoi.) and factor DG (the interaction between cathode stoi. and backpressure) have negative effects on voltage oscillation response. It is easy to understand that a higher cathode stoichiometric ratio can increase the ability to flush out the liquid water in the cathode flow channels, and also decrease the voltage fluctuation behavior. In contrast, factor G (Backpressure) has a positive effect on the voltage oscillation response. The reason is that high operating pressure can lead to high water vapor partial pressure. However, the water saturation pressure is constant at the constant temperature, thereby, more liquid water will be condensed at higher operating pressure, and thus cause an increase of the voltage fluctuation. The chosen significant factors in Figure 5.6c and 5.6e are just the same as those in Figure 5.6a. However, the whole-plot factor b (temperature) is additionally chosen in Figure 5.6d and 5.6f, which indicates that more water is generated at higher current densities, the higher temperatures can help to evaporate the liquid water into water vapor, thereby reducing the voltage oscillation behavior. In Figure 5.6g at 1.2 A/cm^2, factor F (Cathode R.H.) is additionally chosen as a significant factor, which has a positive effect on the voltage oscillation behavior. Since a high inlet gas relative humidity can introduce more water into the test cell,

combined with the high current density, more liquid water will be present in the flow channel, thereby increasing the voltage fluctuation behavior. It is worth noting that some terms in Figure 5.6 are not included in the regression model even though their t-values are higher than the t-value limit. It is because these terms are three or higher-order factors interaction. As aforementioned, the interactions of three factors or higher orders almost do not exist in the system and can be safely ignored during the significance factor selection process. The voltage oscillation regression models are well validated, and detailed information can be found in Appendix A.8.
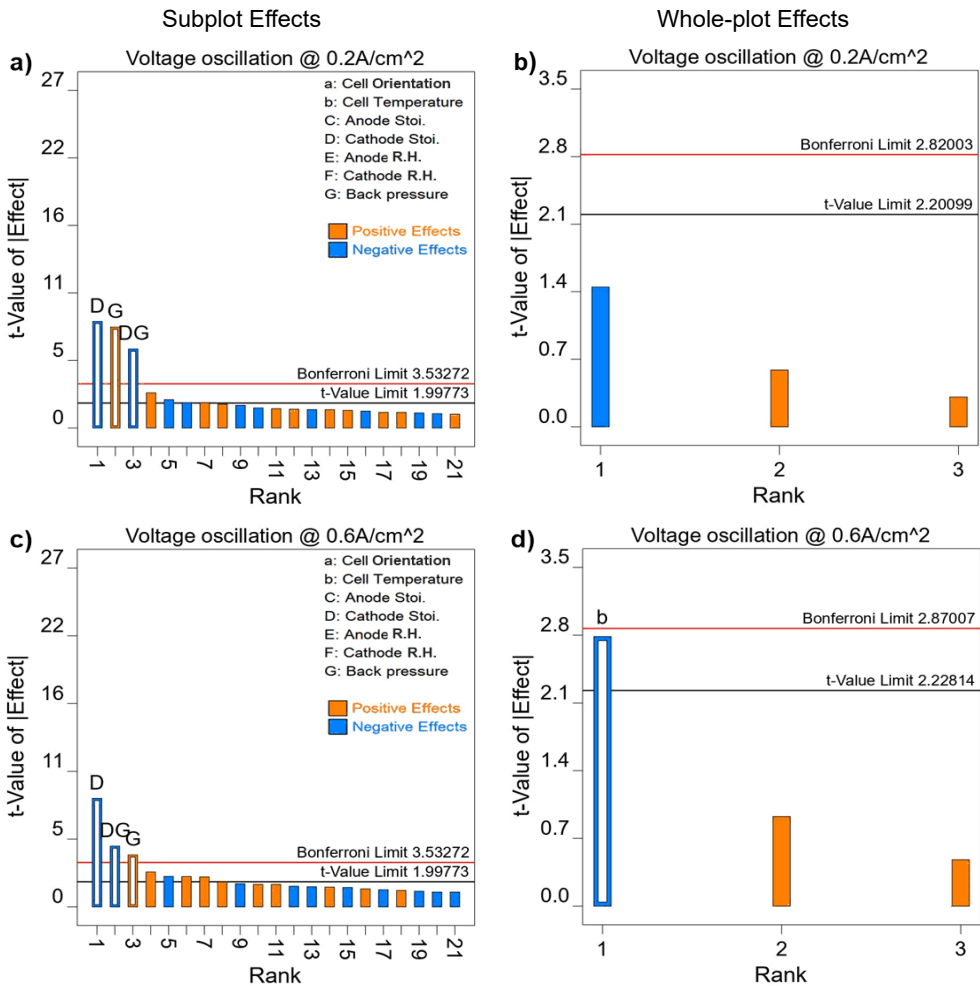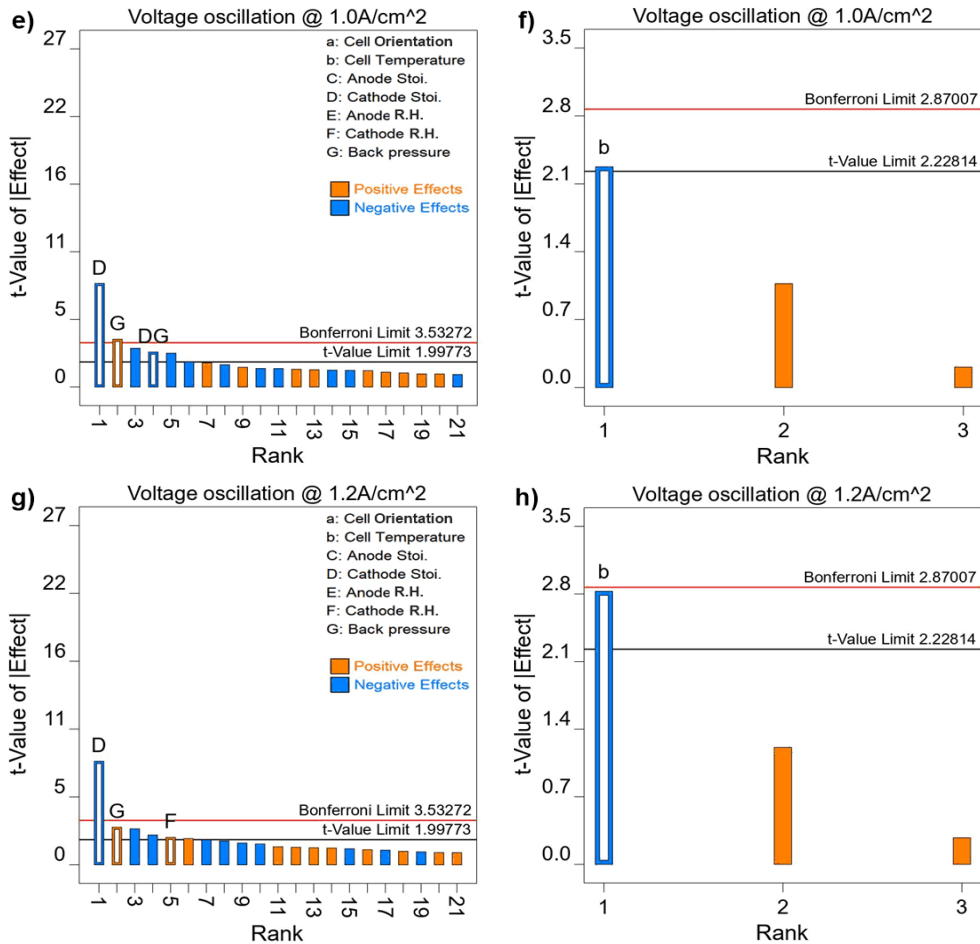
Figure 5.6: Pareto charts for the voltage oscillation response model at the current densities of 0.2 A/cm², 0.6 A/cm², 1.0 A/cm², 1.2 A/cm².

5.3.2 Curvature examination

In the last section, the split-plot factorial design was used to screen the statistically significant factors from a pool of parameters. As a result, temperature, cathode stoichiometric ratio, cathode relative humidity and backpressure were chosen as significant factors that can significantly influence the static performance of the LT-PEFCs. Out of expectation, the factor of the cell orientation (a) was not considered as a significant factor according to the results. The low level of the factor orientation (a) is that the test cell is orientated horizontally and the cathode side is under the anode side, which was quantified to 0°; the high level is that the cathode side is above the anode side, which was quantified to 180°. The results of the split-plot factorial design indicate

that the voltage response, the pressure drop response and the voltage oscillation response at the low level (0°) and the high level (180°) are not significantly different. However, it does not imply that there is no relationship between cell orientation and cell performance.

In a two-level split-plot factorial design, apart from the low and high levels of each factor, the center point information was also considered. Eight center points were additionally added in the design matrix, and in each center point, the cell orientation was set to 90° (vertical position), and the remaining factors were also set to their medium level. Figure 5.7 illustrates the center points of three responses with the different current densities. For the voltage response as shown in Figure 5.7(a), at 0.2 A/cm^2, a deviation between the average response (black line) and the responses at the center point (red points) was detected. With the increase of the current density, the deviation between the average response and the center point responses is becoming more significant, and the curvature effect (black dashed line) was found. Just as same as in Figure 5.7(a), the curvature effects were also detected in the pressure drop response as in Figure 5.7(b), and the voltage oscillation response as in Figure 5.7(c). Due to the limitations of the two-level factorial design, however, it cannot distinguish whether the curvature effect is caused by the cell orientation factor or by other factors. These factor effects are associated with each other. In order to get a precise assessment of the curvature effects of these statistically significant factors, the response surface methodology (RSM) was applied.
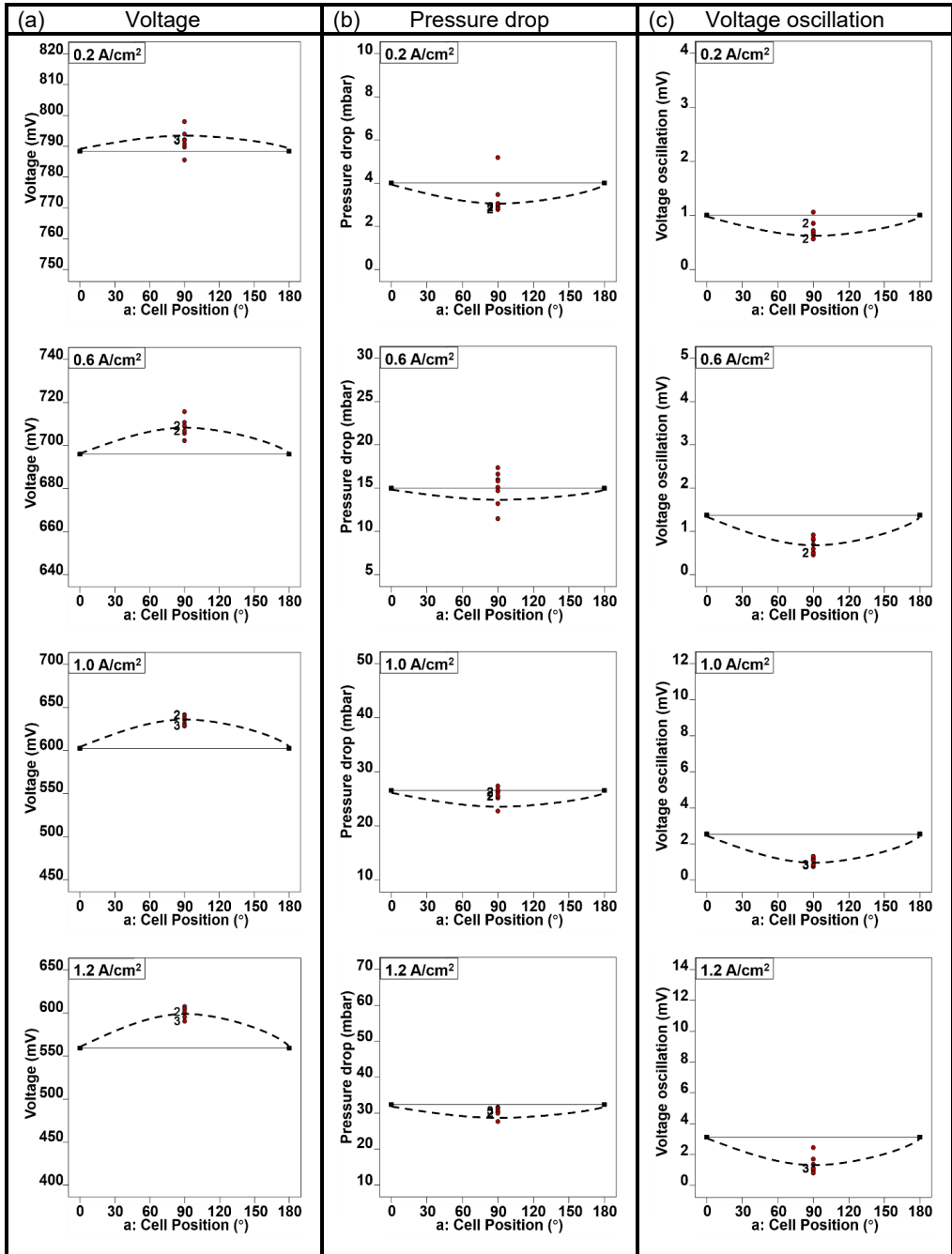
Figure 5.7: The center points in three responses with the different current densities.

5.4   RSM study results and discussion

RSM (Response Surface Methodology) is an effective statistical tool that is widely used in optimization problems. The two-level factorial design method is used as a screening approach to determine the statistically significant factors. Then RSM is applied to search for the optimal operating conditions based on these significant factors. The central composite design (CCD) is one primary type of RSM which was utilized in this experiment. Apart from the high-/low-level of each factor, CCD also adds the middle level of each parameter into the design matrix. A total number of 51 tests were performed. The design matrix of RSM study is illustrates in Appendix A.9.

5.4.1 Results of quadratic regression model

The quadratic regression model for each response was generated through the CCD method, which the general form can be expressed as the following equation [124]:

$$y = \beta_0 + \sum_{i=1}^{k} \beta_i x_i + \sum_{i=1}^{k-1} \sum_{j=i+1}^{k} \beta_{ij} x_i x_j + \sum_{j=i+1}^{k} \beta_{ii} x_i^2 + \varepsilon \qquad 5.2$$

where:

y: response value,

x_i: input coded factors,

β_0:   constant term,

β_i: coefficient of the first-order term,

β_{ij}:   coefficient of the interaction term,

β_{ii}:   coefficient of quadratic term,

ε: model residual.

5.4.1.1 The voltage response quadratic regression model

Table 5.6 presents the quadratic regression models of the voltage response at different current densities. In the quadratic models for the current densities at 0.2 A/cm^2 and 0.6 A/cm^2, compared to the corresponding linear regression models in Table 5.3, the quadratic term b^2 was added to the quadratic models. At higher current densities at 1.0 A/cm^2 and 1.2 A/cm^2, apart from b^2, the quadratic terms a^2 were also added to the quadratic models. It can be concluded that the curvature of the voltage response at low and middle current densities is contributing to the temperature (factor b) effect; the curvature at higher current densities can contribute to both effects of the temperature (factor b) and cell orientation (factor a). In this case, the non-significant factor a was also added to the quadratic regression model, which is used to support the hierarchy of factor a^2.

Table 5.6: The voltage response quadratic regression model. (a: Cell orientation, b: Temperature, D: Cathode stoi., F: Cathode R.H., G: Backpressure)

1) Voltage @0.2 A/cm² =	2) Voltage @0.6 A/cm² =	3) Voltage @1.0 A/cm² =	4) Voltage @1.2 A/cm² =
+786.48	+694.83	+617.48	+597.32
+2.17 b	+6.36 b	+4.02 a	+5.29 a
+1.10 D	+3.55 D	+16.47 b	+23.77 b
+17.36 G	+22.16 G	+12.98 D	+22.73 D
+0.52 bG	-0.79 bD	+21.35 G	+17.18 G
-8.54 b²	+1.25 bG	-4.57 bD	-10.82 bD
	-12.43 b²	+9.84 bG	+18.14 bG
		+4.21 DG	+8.20 DG
		-7.56 a²	-13.84 a²
		-20.40 b²	-27.44 b²

5.4.1.2 The pressure drop response quadratic regression model

Table 5.7 presents the quadratic regression models of the pressure drop response. Compared to the corresponding linear regression models in Table 5.4, the term a^2 was added to the quadratic model at all current densities. The curvature of the pressure drop response can contribute to the cell orientation (factor a).

Table 5.7: The pressure drop response quadratic regression model at different current densities. (a: Cell orientation, b: Temperature, D: Cathode stoi., F: Cathode R.H., G: Backpressure)

1) Pressure drop @0.2 A/cm² =	2) Pressure drop @0.6 A/cm² =	3) Pressure drop @1.0 A/cm² =	4) Pressure drop @1.2 A/cm² =
+2.50	+11.44	+21.18	+24.73
+0.0348 a	+0.4972 a	+0.3562 a	+0.0214 a
+0.9796 D	+3.64 D	+7.73 D	+0.4646 b
-0.8876 G	-2.48 G	-4.84 G	+10.03 D
-0.3392 DG	-0.5525 DG	-1.87 DG	-6.83 G
+0.8114 a²	+1.48 a²	+0.8937 a²	+0.7795 bD
			-2.75 DG
			+2.28 a²

5.4.1.3 The voltage oscillation response quadratic regression model

Table 5.8 presents the quadratic regression models of the voltage oscillation response. In the quadratic models for the current densities at 0.2 A/cm^2 and 0.6 A/cm^2, compared to the corresponding linear regression models in Table 5.5, the quadratic term D^2 was added to the quadratic models. At higher current densities at 1.0 A/cm^2 and 1.2 A/cm^2, quadratic terms a^2 and D^2 were both added to the quadratic models. The curvature of the voltage oscillation response at low and middle current densities is contributing to the cathode stoichiometric ratio (factor D) effect; the curvature at higher current densities can contribute to both effects of the cathode stoichiometric ratio (factor D) and cell position (factor a).

Normal residual plots and residuals versus run order plots show that the residuals of these quadratic models are normally distributed and also independent of each other (see Appendix A.10 for details). Quadratic regression models are well validated.

Table 5.8: The voltage oscillation response quadratic regression model at different current densities. (a: Cell orientation, b: Temperature, D: Cathode stoi., F: Cathode R.H., G: Backpressure)

1) Voltage oscillation = @0.2 A/cm^2	2) Voltage oscillation = @0.6 A/cm^2	3) Voltage oscillation = @1.0 A/cm^2	4) Voltage oscillation = @1.2 A/cm2
+1.02	+0.98	+1.66	+2.20
-0.5903 D	-0.1129 b	+0.0550 a	+0.1226 a
+0.1140 G	-0.5511 D	-0.3952 b	-1.05 b
+0.3170 D^2	+0.0713 G	-1.28 D	-1.86 D
	-0.1024 bG	+0.5440 G	+0.0855 G
	-0.1381 DG	-0.2500 bG	+0.4111 bD
	+0.4885 D²	-0.1185 DG	-0.7283 bG
		+0.5077 a²	-0.4547 DG
		+0.8206 D^2	+1.07 a²
			+1.23 D^2

5.4.2 Performance analysis

With the split-plot design method, the significant factors, including cell orientation (a), cell temperature (b), cathode stoichiometry ratio (D), and backpressure (G), were selected from a pool of parameters. Also, the curvature effect of each significant factor was detected and separated from each other using the RSM method. Corresponding quadratic regression models regarding the response of voltage, pressure drop and voltage oscillation were generated based on these significant factors as well as their interactions. The contour plots in Figure 5.8-5.11 were used to give a clear interpretation of the effects of the selected factors on the targeted responses.

Figure 5.8 shows the contour plots of the voltage response, pressure drop response, and voltage oscillation response (all at 0.2 A/cm^2) as a function of the cell orientation (a) and cathode stoichiometry ratio (D), at four combinations of the temperature (b) and the backpressure (G), namely, b (-) G (-), b (-) G (+), b (+) G (-), and b (+) G (+), in which (-) means the low-level value and (+) means the high-level value. At low temperature and low backpressure (b (-) G (-)), the voltage response (Figure 5.8a) and voltage oscillation response (Figure 5.8c) remain constant during the change in the cell orientation. This is because, at lower current densities, limited liquid water is produced which has limited effects on the cell performance, even at different cell orientations. For the response of cathodic pressure drop (Figure 5.8b), however, a change of the cell orientation will cause a change in the pressure drop value. The minimum value is observed around the cell orientation of 90°. This is because when the test cell is vertically positioned, the flow direction of the reactants is from the cell top to the cell bottom. In this situation, the force of gravity exerted a significant influence on the removal of the liquid water out of the flow field. When the cell is positioned at 0°or 180°, the effect of gravity force on the water removal disappears. It is observed that increasing the cathode stoichiometric ratio can lead to an improvement in the cell voltage and cathodic pressure drop, and also lead to a decrease in the voltage oscillation. This is due to the higher stoichiometric ratio that causes a higher gas flow rate in the cathode side, which can improve the liquid water removal rate and also can increase the availability of oxygen at the reaction site. This leads to a higher cell voltage and a decrease in voltage oscillations. As aforementioned in Equation 5.1, a higher gas flow rate can lead to an increase in the pressure drop. When at low temperature and high backpressure (b (-) G (+)), as shown in Figure 5.8d, voltage improves with the increase of the backpressure to its high level. This is because, at the constant temperature, higher operating pressure can lead to a higher oxygen partial pressure

of the reactants, and thus lead to a higher voltage response. With increasing operating pressure, the water saturation pressure will remain constant and the water vapor partial pressure will increase. If water vapor partial pressure is greater than the water saturation pressure, liquid water will be condensed in the GDL or flow channels. This will lead to an increase in the voltage oscillation level, as shown in Figure 5.8f. A rise in backpressure can lead to a decrease in pressure drop, as shown in Figure 5.8e, which can be inferred from Equation 5.1.

Compared to Figure 5.8a (b (-) G (-)), Figure 5.8g (b (+) G (-)) indicates that voltage improves with increasing temperature. Higher temperatures can result in higher reaction kinetics, and consequently a higher voltage response. It also can be noted in Figure 5.8h and Figure 5.8i that increased temperature does not have any effects on the pressure drop response and voltage oscillation response compared to Figure 5.8b and Figure 5.8c. This is due to low current density resulting in lower gas flow rates. Changes in temperature will affect the gas viscosity and density; however, it will cause a marginal change due to the small amount of gas. Therefore, the temperature is not a significant factor in the pressure drop response at low current density. Regarding the voltage oscillation response, only a small amount of liquid water is produced at the low current density, and the evaporation effect of high temperature is not evident in this condition. The temperature is consequently not a significant factor for the voltage oscillation response at 0.2 A/cm^2. Figure 5.8j illustrates that at high-level temperature and high-level backpressure (b (+) G (+)), voltage reached the highest value. Pressure drop response and voltage oscillation response in (b (+) G (+)) are remained constant compared to that of in (b (-) G (+)), since the temperature is not a significant factor for these two responses at 0.2 A/cm^2.
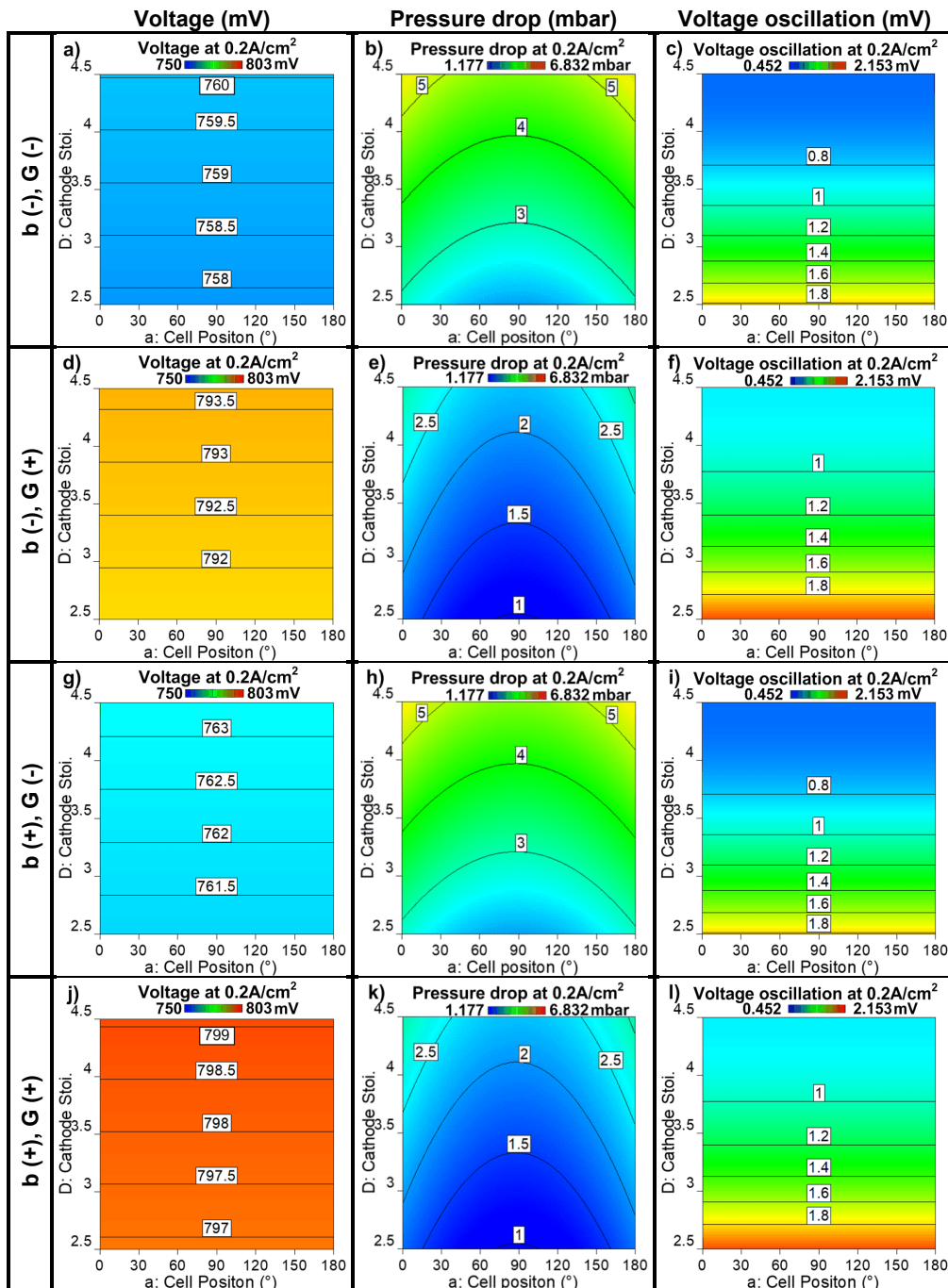
Figure 5.8: Voltage (mV), pressure drop(mbar) and voltage oscillation (mV) response at 0.2 A/cm², with the combination of the different levels of the temperature (b) and the backpressure (G).
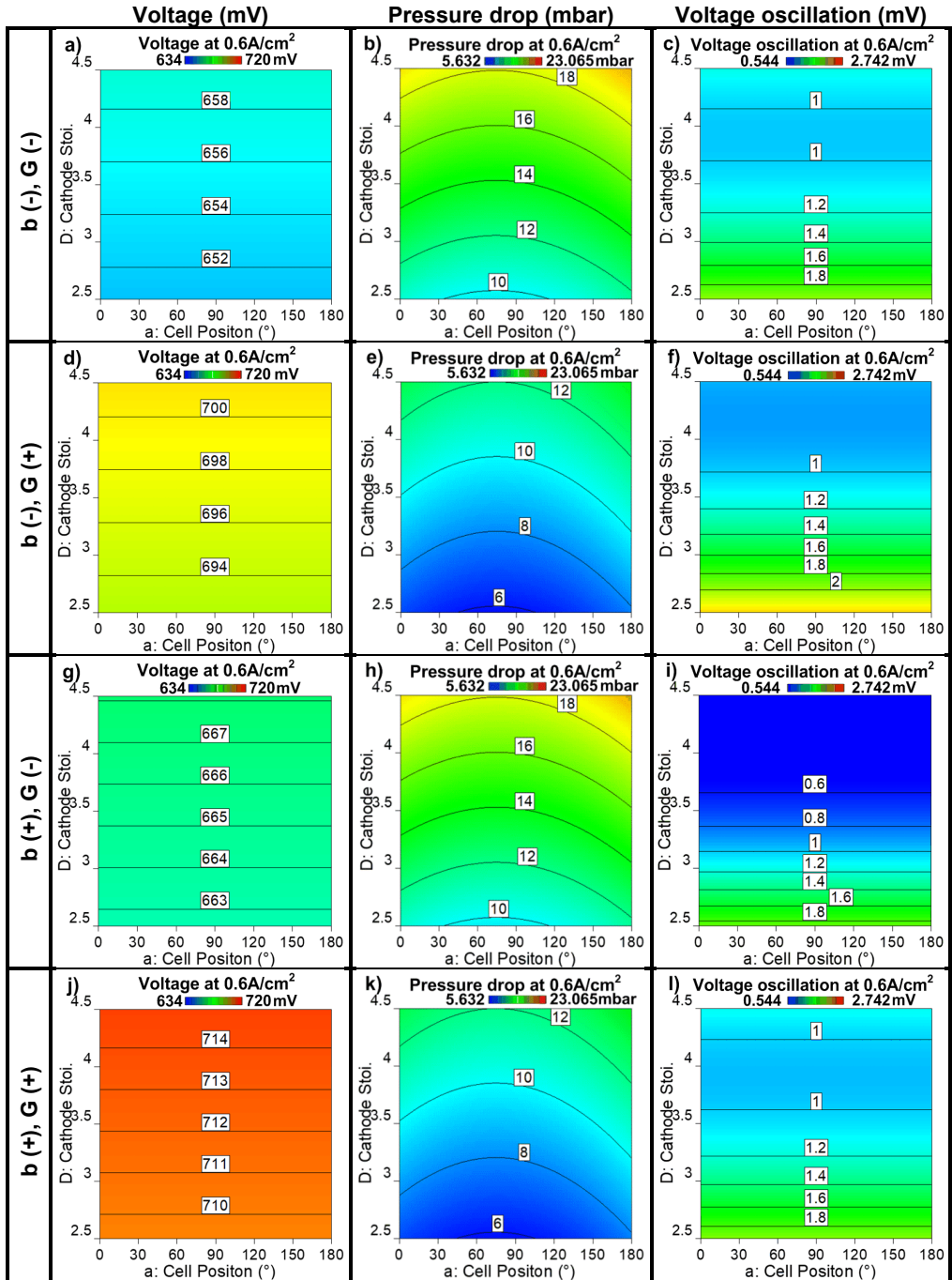
Figure 5.9: Voltage (mV), pressure drop (mbar) and voltage oscillation (mV) response at 0.6 A/cm^2, with the combination of the different levels of the temperature (b) and the backpressure (G).

Figure 5.9 displays the voltage response, pressure drop response, and voltage oscillation response over cell orientation (a) and cathode stoichiometry ratio (D) at 0.6 A/cm^2, with four combinations of the temperature (b) and the backpressure (G), namely, b (-) G (-), b (-) G (+), b (+) G (-), and b (+) G (+). It is observed that at different temperature and backpressure, the effects of cell orientation and stoichiometry ratio on the response of voltage, pressure drop and voltage oscillation at the current density of 0.6 A/cm^2 in Figure 5.9 are similar to those at the current density of 0.2 A/cm^2 in Figure 5.8. However, it was found in Figure 5.9b, 5.9e, 5.9h and 5.9k that the pressure drop response at the cell orientation of 180° is higher than that of at 0°. This is consistent with the results in [88]. It was explained that liquid water in the configuration of 180° is easier to form the slug flow, which causes a higher pressure drop than the film flow formed in the configuration of 0°. For the voltage oscillation response, a temperature rise can result in a decrease of voltage oscillation, which was not observed at 0.2 A/cm^2. This is because that more water is generated at higher current densities and increased temperatures can increase the evaporation rate of liquid water, thus decreasing the fluctuation of the voltage.

Figure 5.10 illustrates three responses at the current density of 1.0 A/cm^2. As in Figure 5.10a, at low temperature and low backpressure (b (-) G (-)), adjusting the cell orientation results in a change of the cell voltage, where the maximum value is observed around the cell orientation of 90° to 120°. When the test cell was vertically positioned, the direction of gas flow is from the top of the cell to the bottom of the cell. In addition to the movement of the gas, the gravity force effect can also contribute to the increase of liquid water removal efficiency in the GDL or flow channel. When the cell orientation is at 0°, the anode side is positioned horizontally on the top of the cathode side, the generated liquid water is more willing to move from the GDL to the flow channel due to the gravity effect. When the cell orientation is at 180°, where the cathode side is located horizontally above the anode side, the generated liquid water is more likely to attach to the GDL, and it will cause a higher hydration level of the membrane. This is the reason that the maximum voltage is found at the cell orientation of 90° to 120°. However, too much water attached to GDL will increase the mass transport losses, which contribute to the decrease of the voltage response at the cell orientation of 180°. This also explains the behavior of the voltage oscillation in Figure 5.10c, that the lowest oscillation was found at about the cell orientation of 90°, and also that the voltage oscillation at 180° is slightly higher than that at 0°.
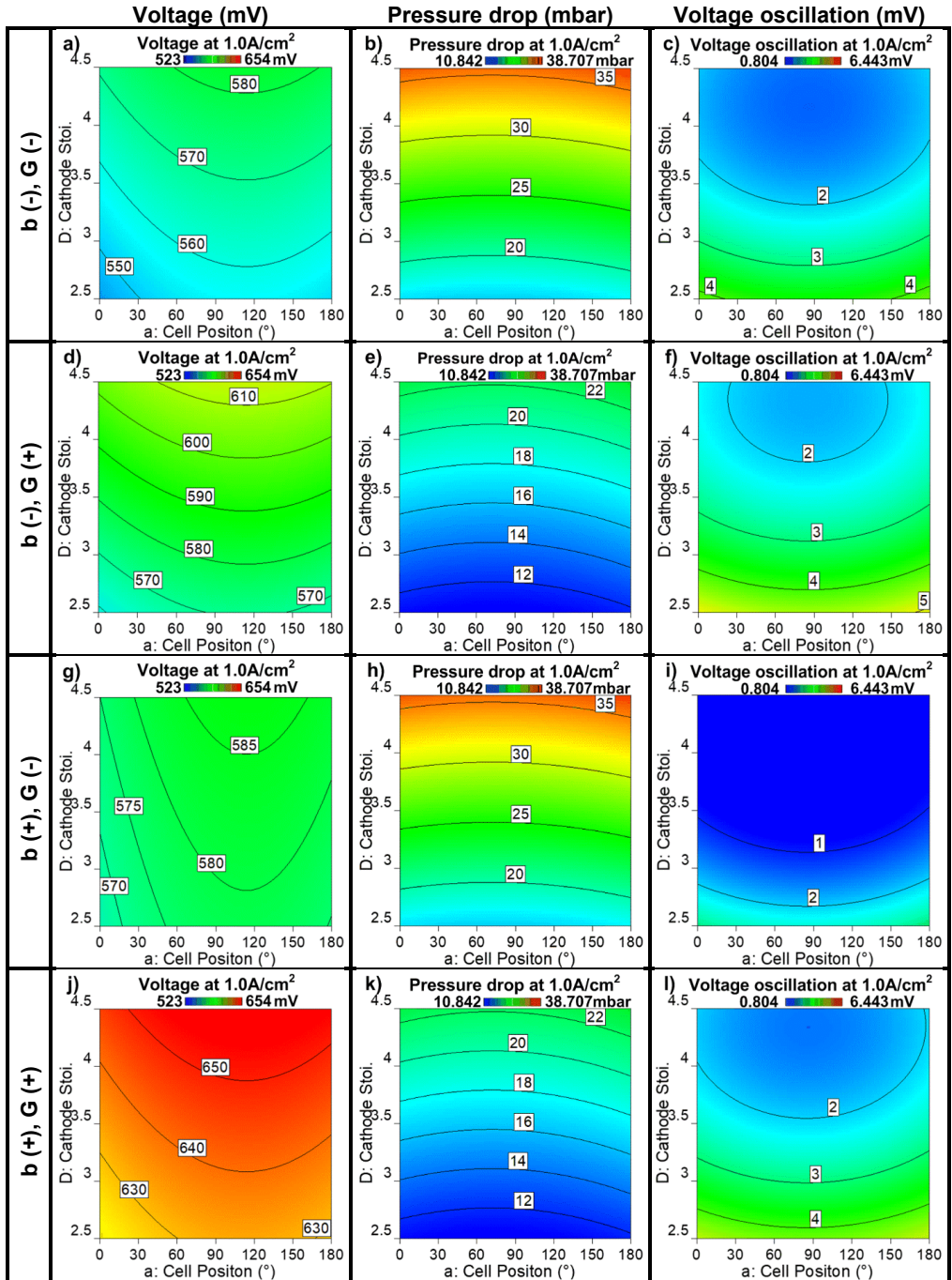
Figure 5.10: Voltage (mV), pressure drop (mbar) and voltage oscillation (mV) response at 1.0 A/cm^2, with the combination of the different levels of the temperature (b) and the backpressure (G).

Overall, it is observed that the effect of temperature and backpressure of targeted responses at 1.0 A.cm^2 are just the same as those at lower current densities.

The observed cell behavior in Figure 5.11 (at 1.2 A/cm^2), with different combinations of temperature and backpressure, is similar to those at 1.0 A/cm^2 (Figure 5.10). It was found in Figure 5.11b, 5.11e, 5.11h and 5.11k that the minimum pressure drop was observed at the cell orientation of 90°. However, the pressure drop value at 0° is very close to that of at 180°, this situation was not observed at lower current densities (except at 0.2 A/cm^2). This is because more water is produced at 1.2 A/cm^2 compared to other lower current densities. This high amount of water is more readily to form water slug flow at the cell orientation of 180° as well as at the cell orientation of 0° rather than film flow. It will cause no significant difference in the pressure drop between the cell orientation of 0° and 180°.

5.4.3 Optimization of selected parameters

The optimized operational factors were obtained through the RSM method and the optimum working conditions were determined. The goal of the optimization is to achieve the maximum voltage response, minimum cathodic pressure drop and voltage oscillation response. Figure 5.12 illustrates the contour plot of the desirability of the operating conditions at different current densities. The highest desirability means that the optimized operating conditions can maximize the voltage response and minimize the pressure drop and voltage oscillation response at the same time.

In Figure 5.12a, at 0.2 A/cm^2, the highest desirability is 0.833, the corresponding optimized operational factors are 88.12° (a), 61.57°C (b), 4.20 (D), 61.90% (F) and 100 kPa (G). In Figure 5.12b, at 0.6 A/cm^2, the highest desirability is 0.892, the corresponding optimized operational factors are 74.75° (a), 66.38°C (b), 3.78 (D), 60.23% (F) and 100 kPa (G). In Figure 5.12c, at 1.0 A/cm^2, the highest desirability is 0.919, the corresponding optimized operational factors are 93.79° (a), 68.47°C (b), 3.32 (D), 60.74% (F) and 100 kPa (G). In Figure 5.12d, at 1.2 A/cm^2, the highest desirability is 0.942, the corresponding optimized operational factors are 96.35° (a), 69.97°C (b), 3.16 (D), 50.03% (F) and 100 kPa (G).
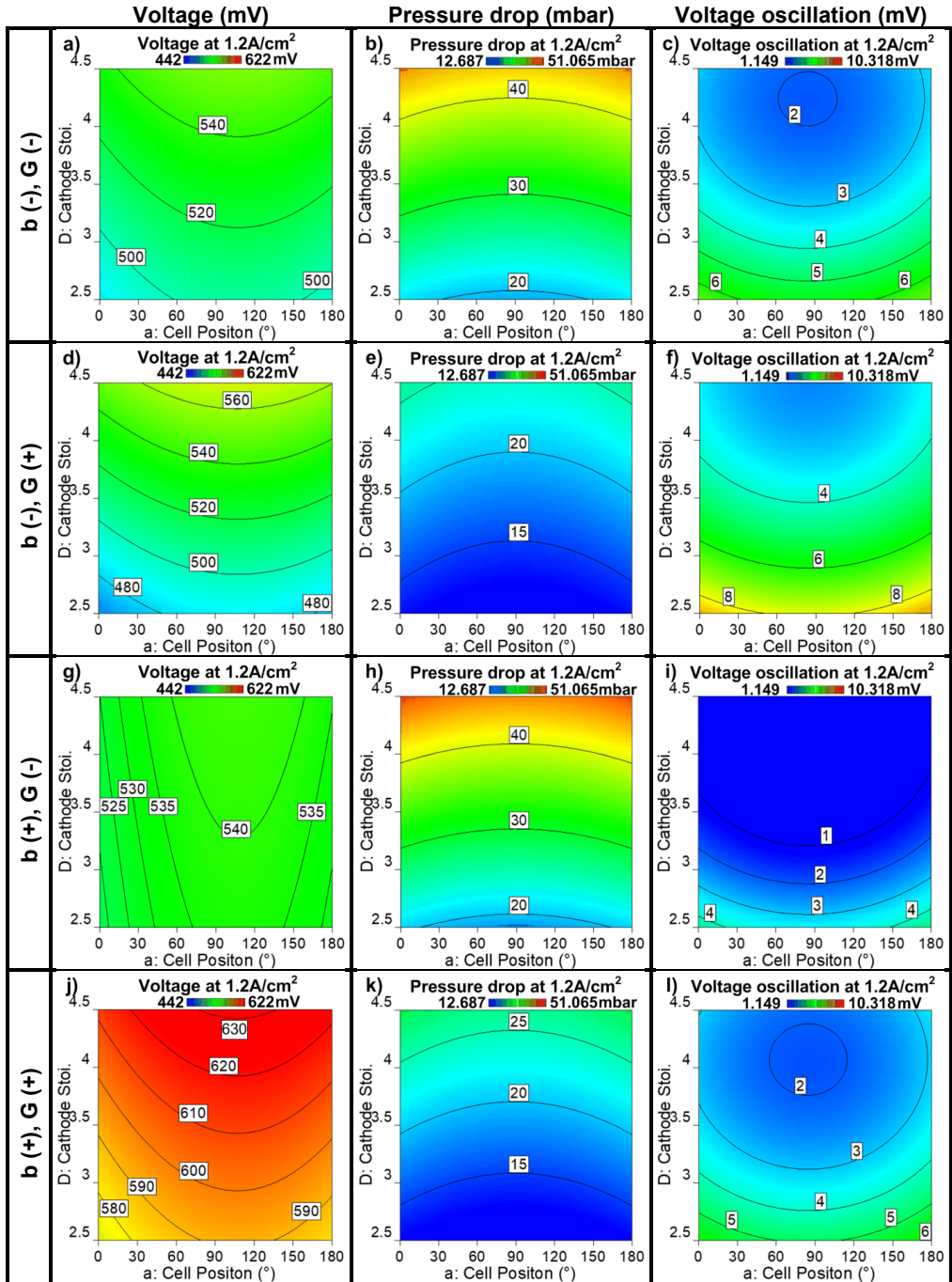
Figure 5.11: Voltage (mV), pressure drop (mbar) and voltage oscillation (mV) response at 1.2 A/cm^2, with the combination of the different levels of the temperature (b) and the backpressure (G).

It can be concluded that the test cell should operate at the vertical position. The optimum temperature is increased with the increase of the current density, which can help to evaporate more generated liquid water at high current densities. The lower relative humidity is needed at a higher current density to decrease the risk of liquid water flooding. The lower cathodic stoichiometric ratio is favored at high current density, which can decrease the pressure drop and hence the parasitic power of the system. The backpressure should be constantly kept at a high-level value at all current densities.
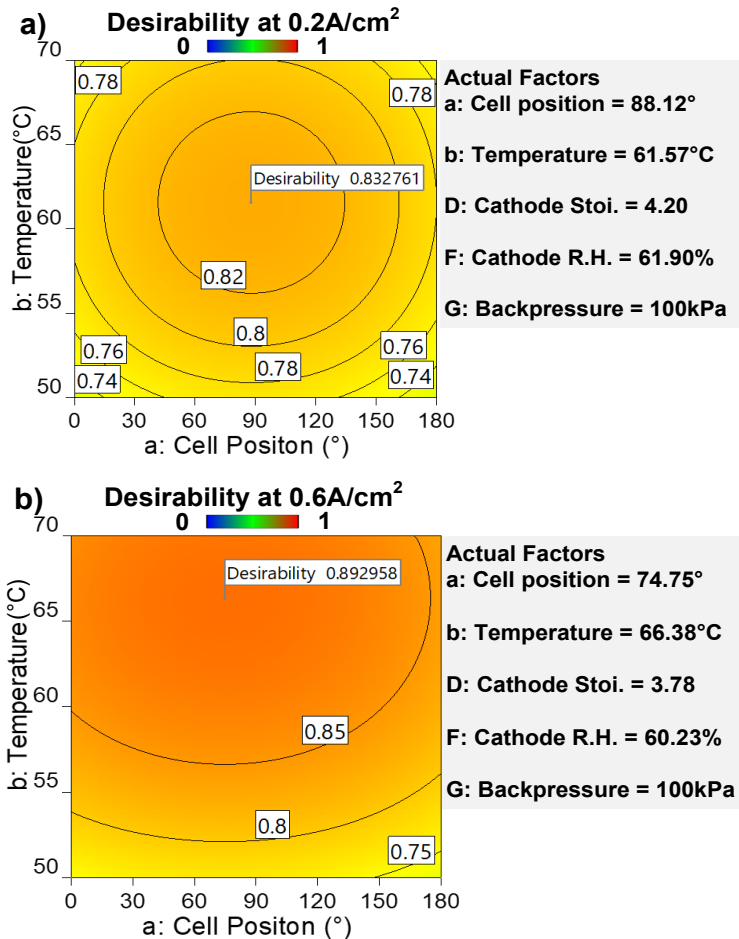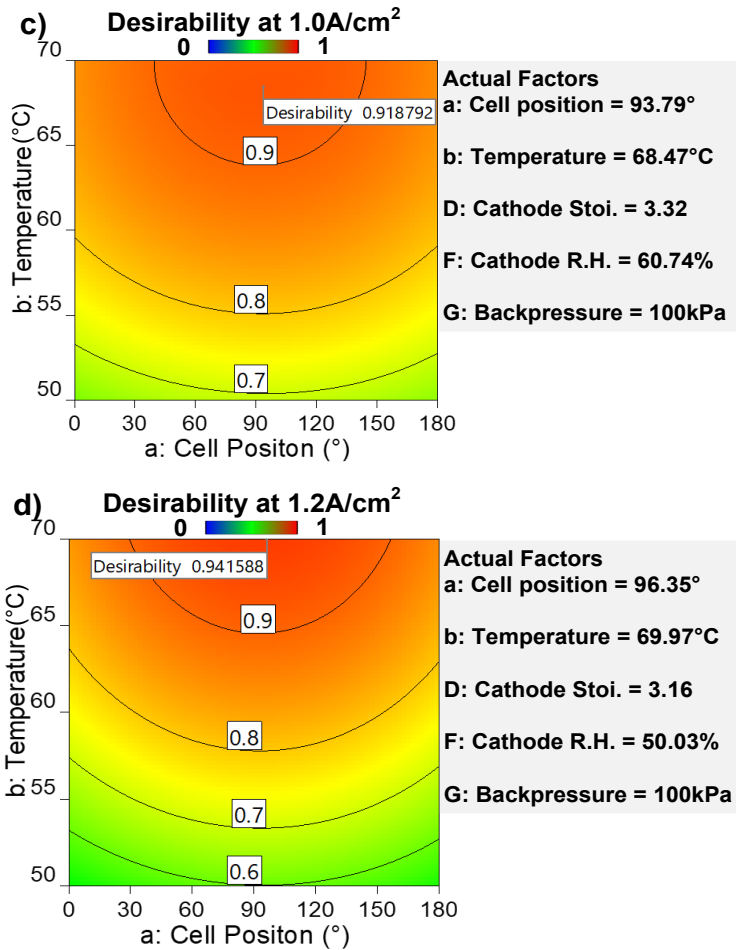
Figure 5.12: Contour plots of desirability at the current densities of a) 0.2 A/cm², b) 0.6 A/cm², c) 1.0 A/cm², and d) 1.2 A/cm².

5.5 Summary

A comprehensive study on the static behavior of the in-house designed PEFC at different operating conditions was performed through the DoE method. The statistically significant factors that have a great impact on the cell voltage, voltage oscillation and pressure drop were determined. The results show that the factor of cell orientation (a), temperature (b), cathode stoichiometric ratio (D), backpressure (G) are the most relevant factors for the cell operation. Then the curvature effect of factors a, b, and D was determined through the RSM method, and the optimum operating conditions for the fuel cell were obtained based on the goal of maximizing voltage response,

minimizing pressure drop and voltage oscillation response. The results show that the vertical position of the test cell is preferred at all current densities, and the optimum value of the remaining factors depends on the different current densities.

6   Transient behavior study of in-house assembled LT-PEFC

This chapter presents the effects of different operating conditions on the transient behavior of the in-house assembled LT-PEFC. The DoE method is used during the experiments to evaluate the importance of the operating conditions (factors) for the transient behavior of the LT-PEFC within the selected operating ranges. Furthermore, the impacts of load change parameters (including load change ramp and load change cycles) on the voltage response, pressure drop response and the cell ohmic resistance response are investigated.

6.1   DoE study of the operating parameters on cell transient behavior

6.1.1 The factor selection

The transient behavior of the test cell can be influenced by many different factors, such as operating temperature, relative humidity, stoichiometric ratio and operating pressure, etc. The detailed descriptions of these factors were discussed in chapter 1 The factor code, the name, the operating ranges and the factor type are summarized in Table 6.1. Seven numeric factors, namely load change step, temperature, anode and cathode stoichiometric ratio, anode and cathode relative humidity, and backpressure were determined during the planning phase of the DoE experiment, each factor has two levels. Among these seven factors, the change of temperature and relative humidity on both anode and cathode requires a large amount of time. Thus, these three factors were regarded as 'hard-to-change parameters', and were considered as whole-plot factors in the split-plot design. The other four factors were considered as subplot factors. In order to distinguish these three factors from the other factors, the factor codes of temperature and relative humidity of both sides were represented by the lower case letters b, e and f, and the other factors were represented by the upper case letters A, C, D and G. It also should be noted that the low-level of factor A means that the current density is shifted positively from 0.2 A/cm^2 to 0.4 A/cm^2 (or negatively from 0.4 A/cm^2 to 0.2 A/cm^2), by one step of (+/-) 0.2 A/cm^2. It should be noted here that (+/-) is just an indicator for the load change direction, (+) for the positive load change and (-) for the negative load change, both of them have no mathematical connotation. The high-level of factor A means that the current density is shifted positively from 0.2 A/cm^2 to 0.8 A/cm^2 (or negatively from 0.8 A/cm^2 to 0.2 A/cm^2), by one step of (+/-) 0.6 A/cm^2.

Table 6.1: Selected factors and their ranges

Factor Code	Factor	Unit	Range	Factor type	Factor rule in SPD
A	Load change step	A/cm²	0.2-0.6	Numeric	Subplot factor
b	Temperature	°C	50-70	Numeric	Whole-plot factor
C	Anode Stoi.		1.2-2.4	Numeric	Subplot factor
D	Cathode Stoi.		2.5-4.5	Numeric	Subplot factor
e	Anode R.H.	%	50-90	Numeric	Whole-plot factor
f	Cathode R.H.	%	50-90	Numeric	Whole-plot factor
G	Backpressure	kPa	0-100	Numeric	Subplot factor

6.1.2 The response selection

As covered in the literature review part (Chapter 1), the voltage undershoot/overshoot behavior was observed during the research of the dynamic behavior of LT-PEFC. It is highly influenced by the different operating conditions. It has been widely used as an indicator to characterize the transient behavior of the test cell [94,95,155]. An example of the voltage undershoot behavior is illustrated in Figure 6.1a. When the current density is changed positively from 0.2 A/cm² to 0.6 A/cm² immediately, the voltage will first drop to the lowest value and then reaches equilibrium. The difference between the lowest value and steady-state value is called the voltage undershoot magnitude. The voltage overshoot behavior is illustrated in Figure 6.1b. When the current density is changed negatively from 0.6 A/cm² to 0.2 A/cm², the voltage will first increase to the highest value and then reach its equilibrium. The difference between the highest/lowest value and equilibrium value is called the voltage overshoot/undershoot magnitude.
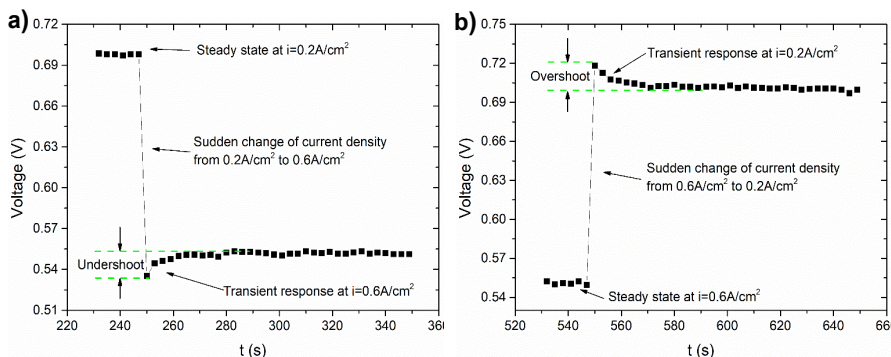
Figure 6.1: Examples for a) voltage undershoot which is caused by the change of the current density positively, and b) overshoot behavior which is caused by the change of the current density negatively.

The reason for the voltage undershoot behavior is that, when increasing the load, the gas consumption rate will increase immediately. Also, with a constant stoichiometry ratio, the gas supply rates increase with increasing current. However, the gas supply and mass transfer speed are much slower than the electrochemical reaction speed [99]. Additionally, the generated water accumulates in the GDL so that the reactant transport pathways are blocked and unable to reach the reaction site on time, which will cause sudden starvation in the short run and the voltage starts to decline. The voltage achieves a constant value again as soon as the mass transfer process reaches the new equilibrium.

The reason for the voltage overshoot behavior is that sudden current drops lead to a decrease in the gas consumption rate. Excess water generated by the previous larger current would have kept the membrane sufficiently hydrated. Furthermore, the gas supply and mass transfer speed are much slower than the electrochemical reaction speed, leading to the presence of relatively high gas concentrations at the reaction sites, and hence the behavior of voltage overshoot occurs. As the mass transfer process reaches a new equilibrium, the voltage decreases and reaches a constant value.

6.1.3 Experimental setup

The detailed configuration of the test station and the test cell were described in chapter 3. The operating conditions used in the dynamic tests are illustrated in Table 6.1. The test cell used in this experiment was set to the vertical position. The effect of the selected seven factors was studied in this experiment, which is load change step

from the low level of (+/-) 0.2 A/cm^2 to the high level of (+/-) 0.6 A/cm^2, the test cell temperature from 50-70°C, anode stoichiometric ratio in the range of 1.2-2.4 and relative humidity of 50-90%, cathode stoichiometric ratio in the range of 2.5-4.5 and relative humidity of 50-90%, the backpressure in the range of 0-100 kPa. According to the two-level factorial design principle, a total number of 128 (with 2 levels and 7 factors: 2^7=128) tests should be performed for both voltage overshoot and undershoot behavior analysis. In order to improve the efficiency of the experiment and reasonably reduce the experimental effort, the fractional factorial design method was applied, by which the number of tests was then reduced from 128 to 64. Despite only half of the test needs to be run after applying the fractional factorial design method. It still results in a high-resolution level of VI, which means the estimations of the main factor effects will not be confounded with the four-factor interaction effects. These 64 tests were run in a random order to avoid influence from systematic disturbances.

6.1.4 DoE study results and discussions

6.1.4.1 Results of linear regression models

Linear regression models for the targeted responses were generated according to the results of the split-plot design. The coded factor equation model was used in the analysis part. The voltage undershoot and overshoot regression models are shown in Table 6.2. In the voltage undershoot regression model, factor A (Load change step), factor b (Temperature), factor D (Cathode stoi.), factor e (Anode R.H.), factor f (Cathode R.H.), factor G (Backpressure) and the interaction factors Ab and AG are statistically dominant among all factors. In the voltage overshoot regression model, factor A (Load change step), factor D (Cathode stoi.), factor G (Backpressure) and the interaction factor Ab are selected as significant factors. It should be noted that the non-significant factor b was also added to the voltage overshoot model, which is used to support the hierarchy of the interaction factor Ab.

Table 6.2: The voltage response regression model. (A: Load change step, b: Temperature, C: Anode stoi., D: Cathode stoi., e: Anode R.H., f: Cathode R.H., G: Backpressure)

1) Voltage undershoot =	2) Voltage overshoot =
20.49	+16.16
+7.81 A	+4.60 A
-3.09 b	-0.5447 b
-2.56 D	-1.59 D
+1.94 e	-1.48 G
-2.06 f	-0.8367 Ab
-6.23 G	
-2.77 Ab	
-2.96 AG	

Significant terms in the regression model

Figure 6.2 shows the Pareto charts of the voltage undershoot and overshoot regression models, which can be considered as a useful graphical tool to determine, which factors and their interactions are significant enough to be used in a regression model. The descriptions of the Pareto charts were discussed in chapter 5. As a brief recap, if the t-value of the factor exceeds the t-value limit or the Bonferroni limit, then this factor is regarded as a significant factor and can be added to the regression model, as shown in Figure 6.2 represented by open bars. The factor that has a positive effect on the targeted response is represented by the color orange, and the factor that has a negative effect on the targeted response is represented by the color blue. Figure 6.2a and 6.2c include the subplot factors, the interaction between these subplot factors, and the interaction between subplot factors and whole-plot factors. Figure 6.2b and 6.2d include whole-plot factors and their interaction factors. In Figure 6.2a, the selected subplot factors for the voltage undershoot response are factor A (Load change step), D (Cathode Stoi.), G (Backpressure), and their interactions AG and Ab. In addition, except for factor A, all selected factors have a negative effect on the voltage undershoot response, which means that increasing the values of these factors will reduce the voltage undershoot magnitude. In Figure 6.2b, the selected whole-plot factors for the voltage undershoot response are b (Cell temperature), e (Anode R.H.) and f (Cathode R.H.). Also, factors b and f have a negative effect, factor e has a positive effect on the voltage undershoot response. For the voltage overshoot response, in Figure 6.2c, the selected subplot factors are factor A (Load change step), D (Cathode

Stoi.), G (Backpressure), and their interactions Ab, which factor A has a positive effect, the factors D, G and Ab have a negative effect on the voltage undershoot response. In Figure 6.2d, despite the t-value of factor b (Cell temperature) is lower than the t-value limit, still, it is selected as a whole-plot factor. The reason is that the non-significant factor b was used to support the hierarchy of the interaction factor Ab. It can be observed that fewer factors are related to the overshoot response compared to the undershoot response. The voltage undershoot and overshoot regression models are well validated, and detailed information can be found in Appendix A.11.
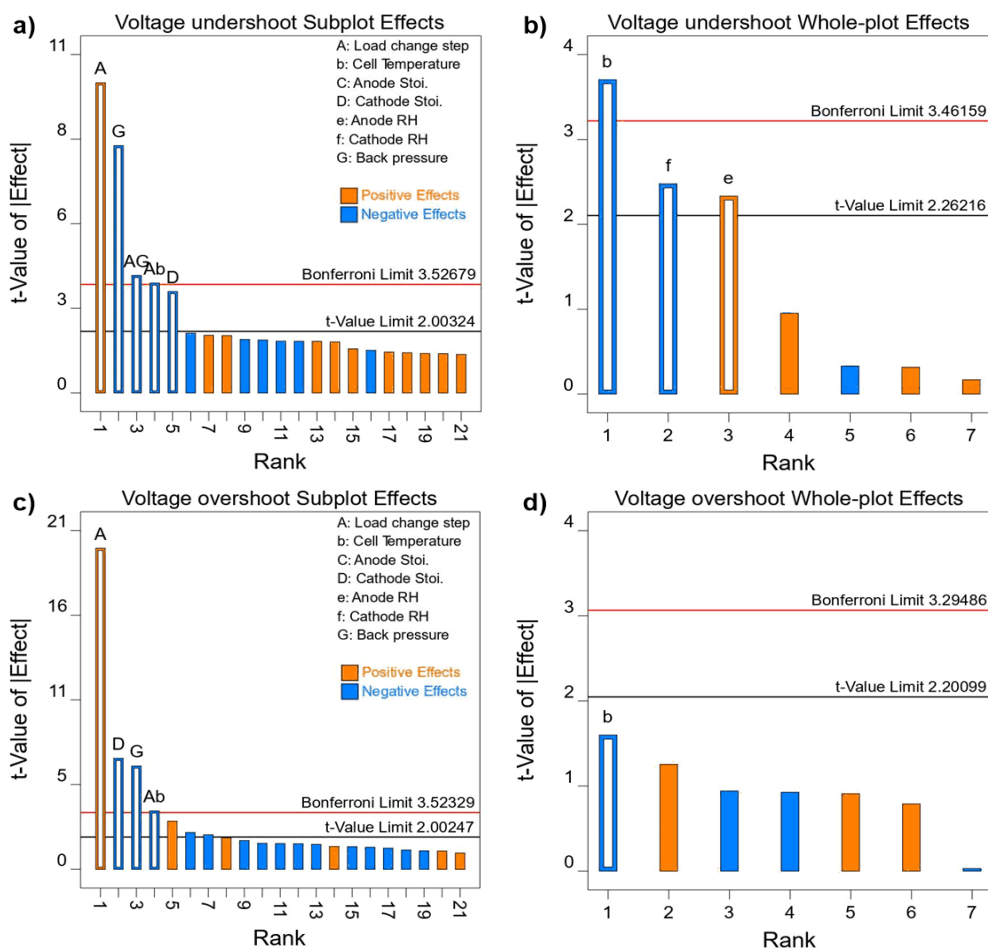
Figure 6.2: Pareto charts for voltage overshoot and undershoot regression model; a), b) for the subplot effects and c), d) for the whole-plot effects.

6.1.4.2 Performance analysis

The main effects and the interaction effects of the selected significant factors on the voltage undershoot and overshoot magnitude are presented in this section. Figure 6.3-6.7 illustrate the main effect plot, and Figure 6.8-6.9 illustrate the interaction effect plot. These plots demonstrate the mean effect of each factor on the selected response. The response values are averaged at each level of the factors. In each main effect plot, the black line represents the effect of the factor, the blue horizontal line represents the general average value of all test results. The higher slope of the black line compared to the blue horizontal line means that the change in the corresponding factor level has a greater influence on the response. In each interaction effect plot, two non-parallel lines mean there is an interaction between the two factors. The more non-parallel the two lines (in black and red), the greater the interaction effect on the response.

Load change step

The influences of the load change step on the voltage undershoot behavior and voltage overshoot behavior are shown in Figure 6.3. It can be observed from Figure 6.3a that the voltage undershoot magnitude at the load change step of $+0.2$ A/cm^2 (0.2 to 0.4 A/cm^2) is lower than that at the load change step of $+0.6$ A/cm^2 (0.2 to 0.8 A/cm^2). This is because the reactant gas supply speed is slower than the electrochemical reaction speed. A higher load change step results in a higher gas consumption rate and a water generation rate, which will exacerbate the gas starvation situation and consequently increase the voltage undershoot magnitude. In Figure 6.3b, a similar trend was observed, that the voltage overshoot magnitude increases with an increase of the load change step from -0.2 A/cm^2 (0.4 to 0.2 A/cm^2) to -0.6 A/cm^2 (0.8 to 0.2 A/cm^2). A large load change step -0.6 A/cm^2 will result in a relatively large reactant concentration on the electrode, and thus a large overshoot magnitude.
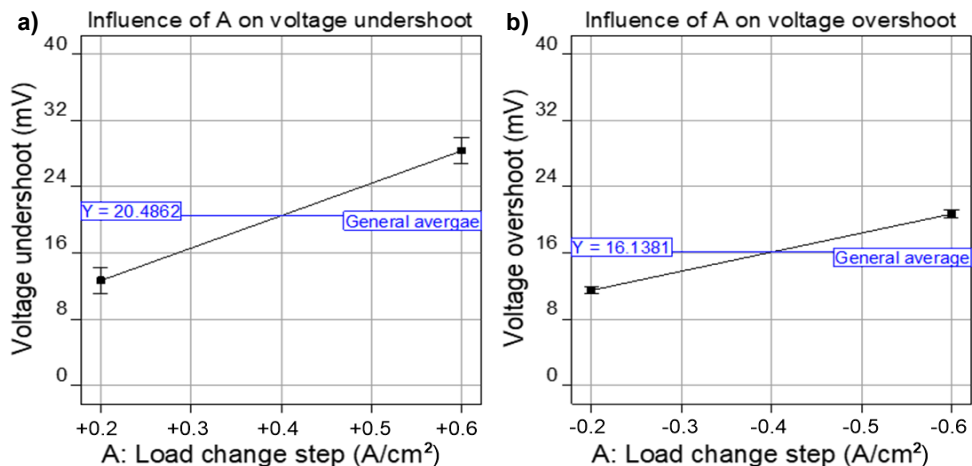
Figure 6.3: Effects of load change step on the response: a) effects on the voltage undershoot behavior; b) effects on the voltage overshoot behavior.

Temperature

The effects of temperature on the voltage undershoot behavior and voltage overshoot behavior are shown in Figure 6.4. It can be observed from Figure 6.4a that the voltage undershoot magnitude at the temperature of 70°C is lower than that at 50°C. Higher temperatures can evaporate more liquid water into water vapor, resulting in better access of the reactants to the reaction site and thus a lower voltage undershoot magnitude. The temperature effect plot in Figure 6.4b, is close to the horizontal line, indicating that the change in the temperature level statistically has no significant effect on the voltage overshoot magnitude. This is because the cell has reached its equilibrium at a higher current density. Sudden shifts of the current density from high to low can decrease the gas consumption rate, resulting in a relatively high reactant concentration on the electrode. A change in temperature can affect the two-phase state of water within the cell, which influences the time it takes for a cell to reach a new steady state, but it has a limited effect on the voltage overshoot magnitude.
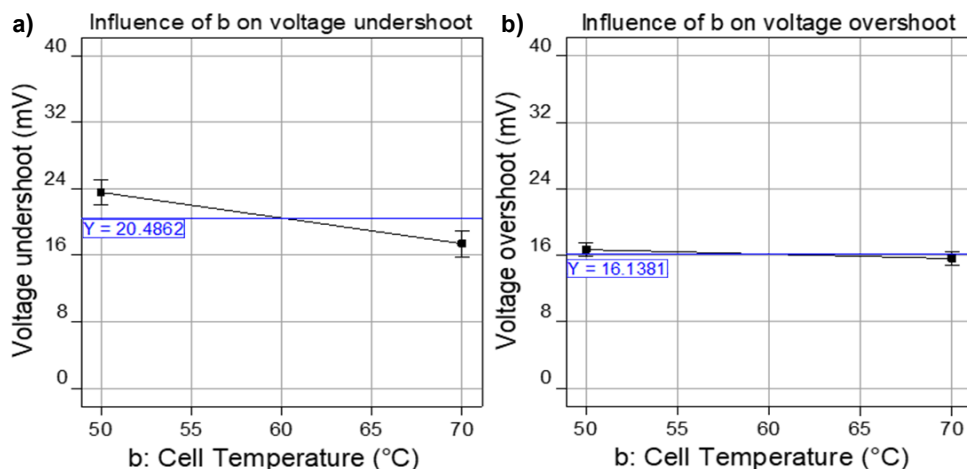
Figure 6.4: Effect of temperature on the response: a) effects on the voltage undershoot behavior; b) effects on the voltage overshoot behavior.

Stoichiometric ratio

The effect of the stoichiometric ratios on the anode side (λ_a) and the cathode side (λ_c) on the voltage undershoot and overshoot behavior are shown in Figure 6.5. It can be observed from Figure 6.5a that the voltage undershoot magnitude decreases with the decrease of the λ_c. A similar trend has also been found in Figure 6.5b, as the voltage overshoot decreases with the decrease of λ_c. The reason is that a higher λ_c could bring a higher oxygen concentration at the reaction site of the electrode, thus reducing the activation loss of the test cell. Besides, higher λ_c helps to flush the liquid water out of the flow channel, reducing the mass transport loss of the test cell.

Figure 6.5c and 6.5d show the effect of λ_a on the voltage undershoot and overshoot magnitude, respectively. From these two figures, it can be found that their effect on the voltage undershoot and overshoot magnitude are not apparent. This is because the gas flow rate at the anode side is much lower than that of the cathode side, the ability to purge out liquid water is much smaller than that of the cathode side. Moreover, the more liquid water the more complex two-phase flow situation at the cathode side. The dynamic behavior of the test cell is much dependent on the situation of the cathode side rather than of the anode side. Consequently, the effect of λ_a within the selected range on the voltage undershoot and overshoot is not significant.
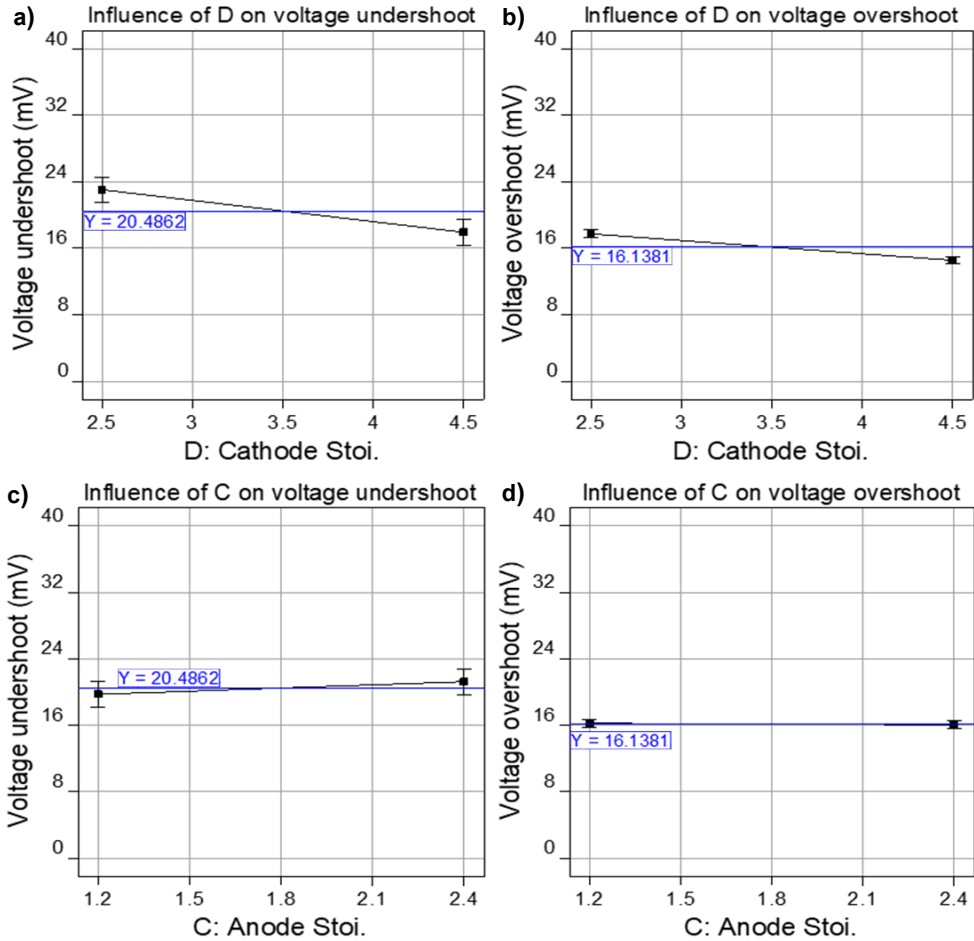
Figure 6.5: Effect of stoichiometric ratio on the response: a) and c) effects on the voltage undershoot behavior; b) and d) effects on the voltage overshoot behavior.

Relative humidity

Figure 6.6 illustrates the effect of relative humidity on the voltage undershoot and overshoot behavior, both the relative humidity at the anode side (R.H.$_a$) and the cathode side (R.H.$_c$) are considered. It can be observed from Figure 6.6a that the voltage undershoot magnitude increased with the increase of the R.H.$_a$. This is because, at the anode side, the ability of the hydrogen to flush out liquid water is relatively small. The high relative humidity at the anode side makes the liquid water cumulating and resulting in a higher mass transport loss and thus a higher voltage undershoot magnitude. Figure 6.6c shows that the voltage undershoot magnitude

decreases with the increase of the $R.H._c$. Lower $R.H._c$ would lead to membrane dehydration and hence increased membrane ohmic resistance, which would reduce the membrane conductivity. Furthermore, when the current density shifts from a low value to a high value at the low $R.H._c$ situation, compared to the electrochemical reaction time, a significant amount of time is required for the membrane rehydration to reach the new steady-state, and eventually cause a higher voltage undershoot magnitude. On the contrary, a higher $R.H._c$ can compensate for the situation caused by the lower $R.H._c$, resulting in a lower voltage undershoot magnitude.

Figure 6.6b and Figure 6.6d show that both the effects of $R.H._a$ and $R.H._c$ on the voltage overshoot magnitude are not obvious. It can be interpreted as the cell has reached its equilibrium at the higher current density. EOD is reduced when current density shifts from the high value to the low values, at which point the membrane hydration level is adequate for the lower current densities. As a result, the effects of $R.H._a$ and $R.H._c$ on the voltage overshoot magnitude are statistically not significant.

Backpressure

Figure 6.7 depicts the effects of the backpressure on the voltage undershoot and overshoot behavior. Note that the backpressure is set equally on the anode side and cathode side. In Figure 6.7a, it can be observed that the voltage undershoot magnitude is decreased with the increase of the backpressure. The reason is that when the current density shifts from a low value to a high value, higher operating pressure can cause an increased reactant concentration on the electrode surface and thus a lower voltage undershoot magnitude. A similar trend was also observed in Figure 6.7b which presents the influence of backpressure on the voltage overshoot behavior. However, the effect of the backpressure on the overshoot behavior is smaller than that of the undershoot behavior. Sudden shifts of the current density from high to low can decrease the gas consumption rate, resulting in a relatively high reactant concentration on the electrode. Under this situation, the effect of the backpressure on the voltage overshoot magnitude is decreased.
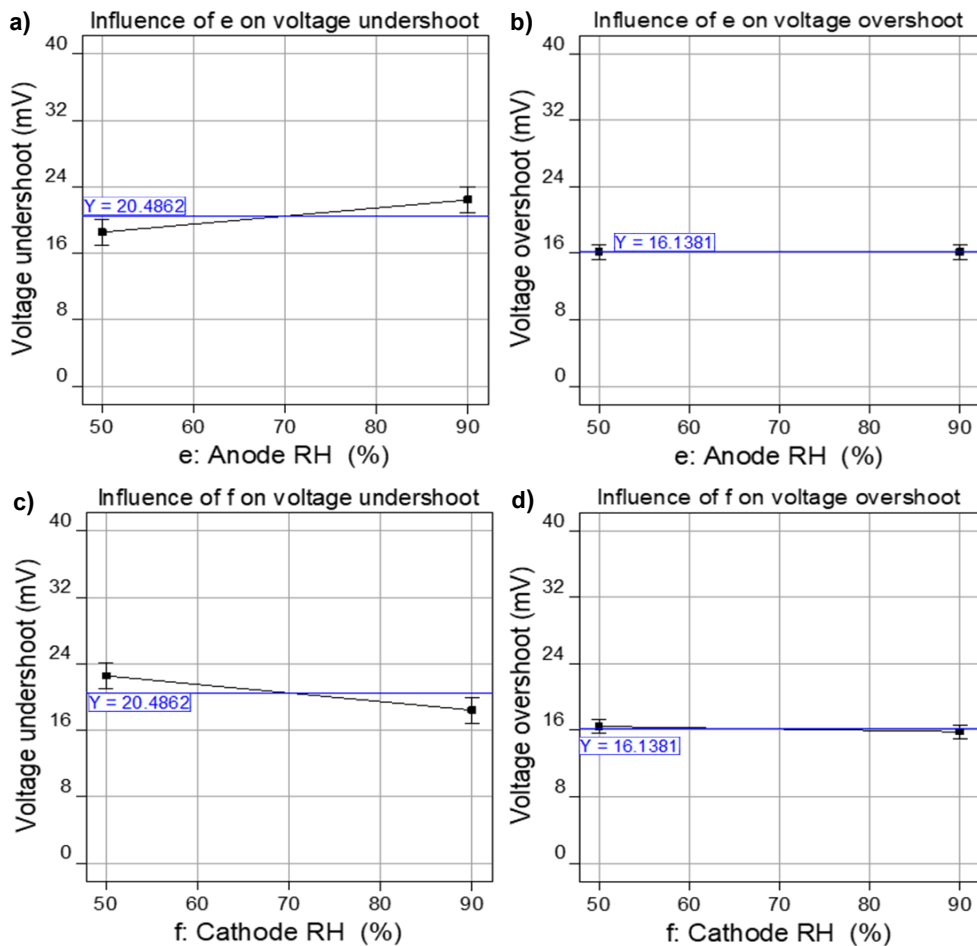
Figure 6.6: Effect of relative humidity on the response: a) and c) effects on the voltage undershoot behavior; b) and d) effects on the voltage overshoot behavior.
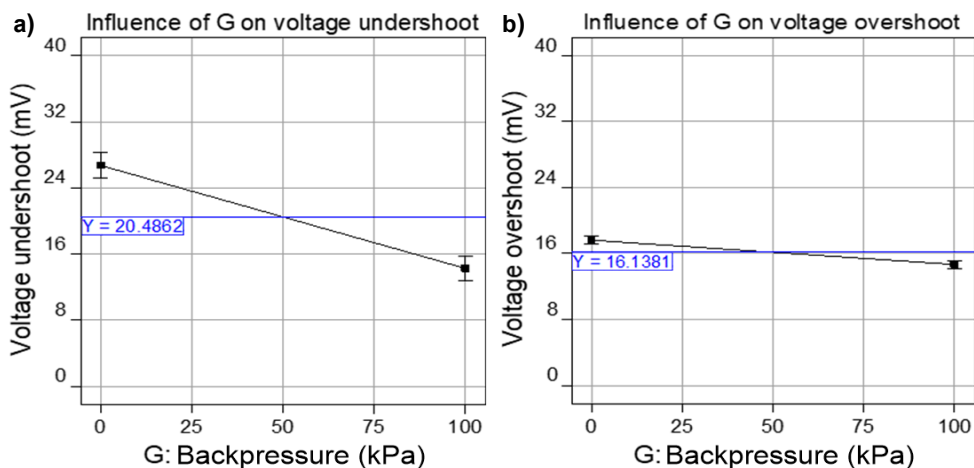
Figure 6.7: Effect of backpressure on the response: a) effects on the voltage undershoot behavior; b) effects on the voltage overshoot behavior.

Ab interaction

The effect of the interaction term Ab on the voltage undershoot and overshoot behavior is shown in Figure 6.8. The operating temperature for the black square is the low level of 50°C (b-), and for the red triangle is the high level of 70°C (b+). It should be noted that the more nonparallel the black line and red line in the figure, the greater the effect of the interaction of two factors on the response.

From Figure 6.8a, it can be found that the effect of the load change step on voltage undershoot magnitude is also affected by the temperature. The effect of the temperature is not significant when the load change step is at 0.2 A/cm², as there is only a slight difference between the black square and red triangle. However, the effect of temperature on the undershoot magnitude becomes more evident at the higher load change step, as a large difference between black square and red triangle is found in Figure 6.8a when the load change step is 0.6 A/cm². This is because a higher temperature can reduce the activation losses and the reactant concentration losses of the test cell, and the effect of increasing temperature on the two losses is more evident at the higher current densities. A similar conclusion can also be obtained concerning the influence of Ab on voltage overshoot, as shown in Figure 6.8b. But overall, the effect of the interaction term Ab on the overshoot behavior is much smaller than that of the undershoot behavior. This is because when the load changes from a high value to a low value, the gas consumption rate decreases, resulting in a relatively high reactant concentration on the electrode. Consequently, the gas starvation situation no

longer exists during this period. The resulting loss of voltage is mainly attributed to the higher activation loss at lower temperatures. This activation loss is not comparable to the loss of the gas concentration when the load shifts from a low value to a high value. Therefore, the interaction factor Ab has a limited impact on the voltage overshoot magnitude.
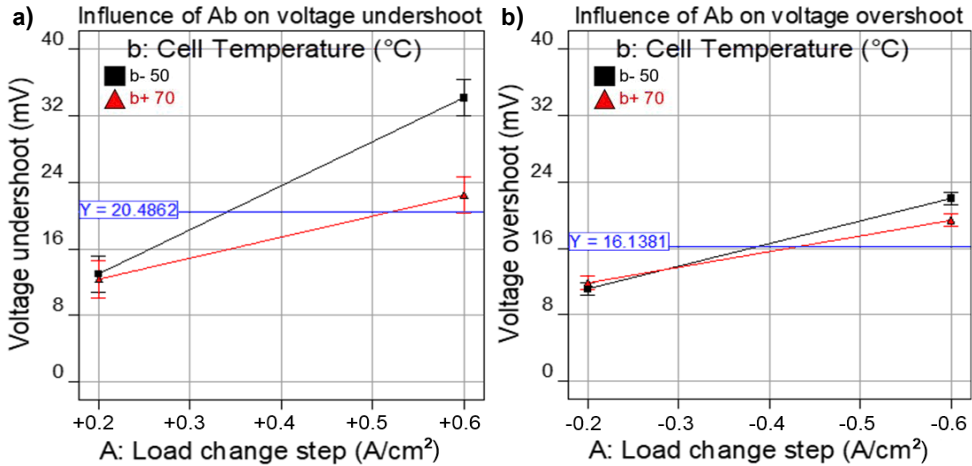
Figure 6.8: Effect of Ab interaction on the response: a) effects on the voltage undershoot behavior; b) effects on the voltage overshoot behavior.

AG interaction

Figure 6.9 shows the effect of the interaction term AG on the voltage undershoot and overshoot behavior. In Figure 6.9a, it can be concluded that the effect of the load change step on voltage undershoot magnitude is also affected by the backpressure. The effect of the backpressure is significant when the small load change step is applied. This is because higher backpressures can reduce the concentration losses of the test cell and thus a lower voltage undershoot magnitude. When the load change step is higher, the sudden gas starvation situation is becoming more severe than that of the lower load change step, it makes the effect of backpressure more evident at the higher load change step. In Figure 6.9b, the interaction term AG's effect on the overshoot behavior is not significant. The reason is that when the load changes from the high value to the low value, the gas starvation situation no longer exists.

Figure 6.9: Effect of AG interaction on the response: a) effects on the voltage undershoot behavior; b) effects on the voltage overshoot behavior.

6.2 Study of the load change ramps on cell dynamic behavior

The statistically significant factors have been determined in the last section. The factor of the load change step has the most impact on the cell dynamic behavior. Hence, it is interesting to know the impact of the different load change methods on the cell dynamic behavior. The responses of voltage, pressure drop and ohmic resistance were recorded during the tests. Part of this section has been published in 'Energies' [89].

6.2.1 Test conditions

The detailed descriptions of the test apparatus and test procedures have been presented in Chapter 3. Table 6.3 illustrates the operating conditions of the experiments. The cell temperature was set to 60°C, the anode/cathode inlet relative humidity was set to 90%/90%, and the stoichiometry ratio on both sides was set equally to 2.

Table 6.3: Test conditions

Cell temperature	60°C
Rel. humidity H_2	90%
Rel. humidity air	90%
λ_{H_2}	2
λ_{Air}	2

Four sets of tests were performed in this study, each test corresponds to different load-cycling profiles. All four tests were started with the same start-up phase, in which the current density was set to 0.2 A/cm² and kept constant for 5 min. Figure 6.10 demonstrates the first load-cycle profile of test No. 1. After the start-up phase, the current density is changed sequentially in four steps:

- Step 1. Change current density linearly from 0.2 A/cm² to 0.6 A/cm² in 5 min.
- Step 2. Keep current density constantly at 0.6 A/cm² for 5 min.
- Step 3. Change current density Linearly from 0.6 A/cm² to 0.2 A/cm² in 5 min.
- Step 4. Keep current density constantly at 0.2 A/cm² for 5 min.

The load ramps in test 1 can be labeled as 5-5-5-5, in which each number represents the time duration for each step. The times for the load ramps and constant current phases of all four tests are listed in Table 6.4. All 4 tests have similar load-cycling profiles but with different change times for the load ramps. In addition, the maximum duration of each test was no more than two hours. The maximum number of cycles from each test was no more than 10.
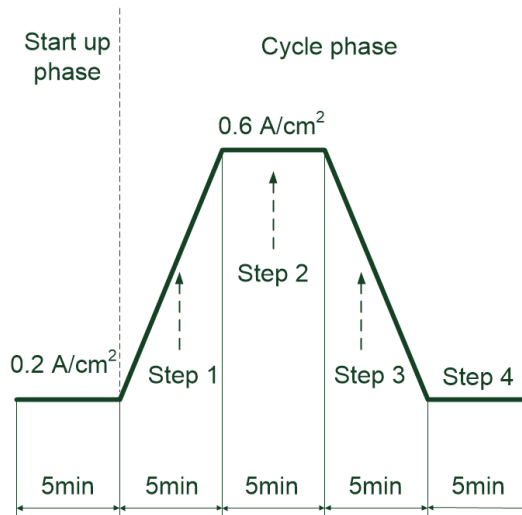
Figure 6.10: The first cycle of the load-cycling profile in test No. 1, label: 5-5-5-5.

Table 6.4: Detailed information of four tests.

Test	Label	Time for each step (minute)			
		Step 1	Step 2	Step 3	Step 4
No. 1	5-5-5-5	5	5	5	5
No. 2	2.5-5-2.5-5	2.5	5	2.5	5
No. 3	1-5-1-5	1	5	1	5
No. 4	0-5-0-5	0	5	0	5

6.2.2 Results and Discussion

The cell voltage response and cathodic pressure drop response of test No. 1 to test No. 4 are illustrated in Appendix A.12.

6.2.2.1 Effect of load ramps on voltage overshoot and undershoot behavior

The voltage overshoot and undershoot behavior were observed from test No. 1 to test No. 4. The reason for the voltage overshoot/undershoot behavior has been discussed in section 6.1.2. The average overshoot magnitude (V_{AOM}) and undershoot magnitude (V_{AUM}) were defined to study the effect of the different load ramps on the voltage overshoot/undershoot behavior. The equations for V_{AOM} and V_{AUM} are as follows:

$$V_{AOM} = \sum_{i=1}^{n} V_{OMi}/n \qquad\qquad 6.1$$

$$V_{AUM} = \sum_{i=1}^{n} V_{UMi}/n \qquad\qquad 6.2$$

where:

V_{OMi}: voltage overshoot magnitude of i_{th} cycle,

V_{UMi}: voltage undershoot magnitude of i_{th} cycle, and

n: the number of cycles.

The effect of different load ramps on V_{AOM} and V_{AUM} is illustrated in Figure 6.11. In Figure 6.11a, V_{AOM} does not show any obvious difference between tests No. 1, No. 2 and No. 3. V_{AOM} is increased obviously in test No. 4. The increase in fluctuation is also observed from test No.1 to test No.4. A similar trend is observed in Figure 6.11b, the values of V_{AUM} are kept constant from tests No. 1 to test No. 3, while an increased V_{AUM} is observed in test No.4, with a huge deviation. It can be concluded from Figure

6.11 that, load change with the ramp (test No.1-No.3) can effectively improve the cell's dynamic behavior, especially for the voltage undershoot behavior, which is caused by the reactant starvation inside the fuel cell. A load ramp can increase the load change duration, this can make a good balance between the fast electrochemical process and the slow gas supply process, and the mass transfer process can consequently achieve equilibrium quickly and easily. In addition, although load change with a ramp can enhance a cell's dynamic behavior (test No.1-No.3), the effect between each ramp on V_{AOM} and V_{AUM} is relatively close, this may suggest that the load change ramp of 1min (test No.3) is adequate to this in-house-assembled LT-PEFC.
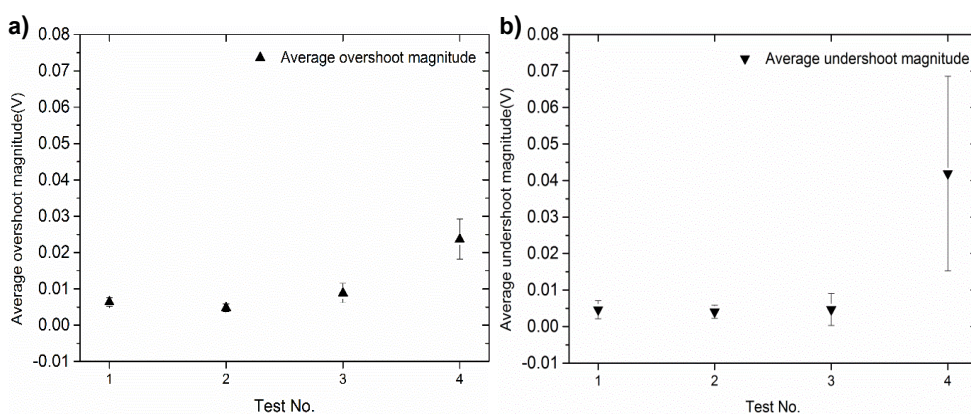
Figure 6.11: Effect of load ramps on the average magnitude a) average overshoot magnitude, V_{AOM}; b) average undershoot magnitude, V_{AUM}.

6.2.2.2 Effect of load ramps on cathodic pressure drop change

The cathodic pressure drop was recorded at the constant current density phase in each test. The top average pressure drop (ΔP_{TopA}) is calculated by averaging the pressure drop at 0.6 A/cm² in each test, and the bottom average pressure drop (ΔP_{BotA}) is calculated at 0.2 A/cm². It can be observed from Figure 6.12 that, the difference of corresponding changes of ΔP_{TopA} and ΔP_{BotA} between each test was not obvious, which implies that the load change ramp has a limited impact on the static behavior of the test cell.
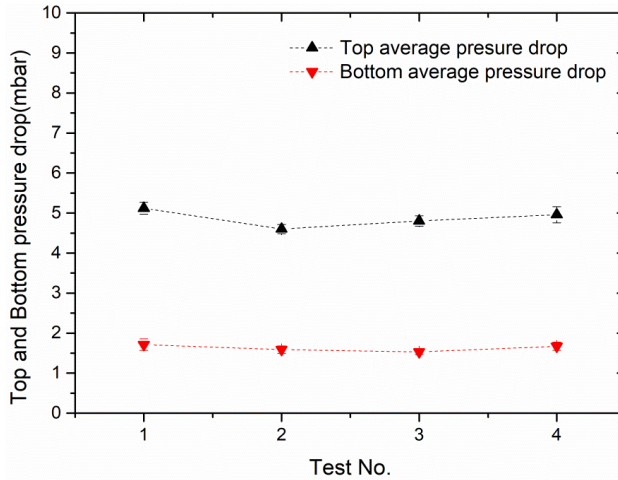
Figure 6.12: The Top and bottom average pressure drop for each test.

6.2.2.3 Effect of load ramps on ohmic resistance

The ohmic resistance of the test cell was measured at the constant frequency of 3 kHz in this experiment. Figure 6.13 illustrates the ohmic resistance at the constant current density phase of 0.6 A/cm² and 0.2 A/cm², in each cycle. It is observed that the ohmic resistance at 0.2 A/cm² is significantly higher than that of 0.6 A/cm². The reason is that more water is produced at higher current densities, which can make the membrane at a good hydration state and thus lead to higher protonic conductivity. It is also found that the difference in ohmic resistance between each test was not significant. As a result, load change ramps have a limited effect on the static behavior of the test cell, which is consistent with the findings in the last section.
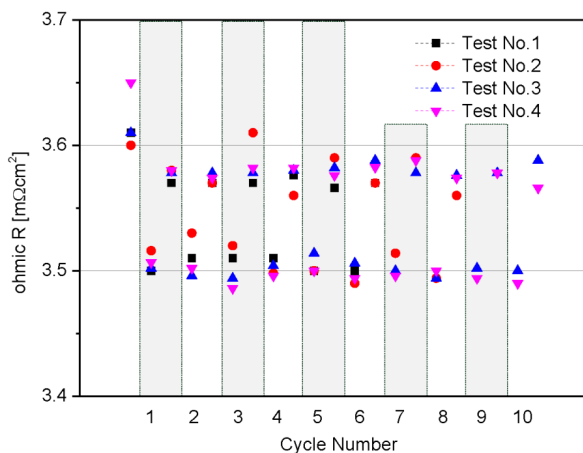
Figure 6.13: Ohmic resistance of different tests and cycles (upper values at 0.2 A/cm², lower values at 0.6 A/cm²).

6.3   Summary

The DoE study was used to investigate the dynamic behavior of the in-house assembled LT-PEFC, where different operating conditions were performed. The factors that have significant impact on the cell voltage undershoot and overshoot behavior were determined through statistical analysis. The results show that the factor of load change step (a), temperature (b), cathode stoichiometric ratio (D), anode relative humidity (e), cathode relative humidity (f), backpressure (G) are statistically significant factors for the voltage undershoot behavior. The factor load change step (a), temperature (b), cathode stoichiometric ratio (D), backpressure (G) are statistically significant factors for the voltage overshoot behavior. In addition, different load profiles were applied to the in-house designed LT-PEFC, and their corresponding cell voltage undershoot and overshoot behavior, pressure drop and ohmic resistance were measured. With the measured data, the impact of the different load profiles on the transient behavior of LT-PEFC was determined. The results show that the load change ramp has a strong effect on the voltage overshoot and undershoot behavior. The load ramps have a limited impact on the average pressure drop value of each test. The difference in the cell ohmic resistance between each load change ramp was not obvious.

7   Discussion

This thesis aimed to investigate the effect of different operating parameters and their mutual influences on the performance of the in-house-assembled LT-PEFC, in which the static behavior and dynamic behavior of the test cell were studied with the help of the Design of Experiments (DoE) methods. The effects of each selected operation parameter on cell performance and underlying mechanisms are identified.

Before the study of the static and dynamic behavior of the test cell, an accuracy study was first carried out to evaluate the reliability of the test cell's results (chapter 4). Data from four test cells were analyzed, in which the components used to assemble the test cells are all from the same batch. Two themes are incorporated in the study: (a) within-cell consistency (repeatability) and (b) between-cell consistency (reproducibility), which are characterized by k-value and h-value, respectively. Both themes are analyzed under four current densities, namely 0.2 A/cm^2, 0.4 A/cm^2, 0.7 A/cm^2, 1.0 A/cm^2, and various operating conditions.

The results of within-cell consistency (Figure 4.3) indicate that the higher stoichiometric ratio (Anode/Cathode: 2/4) results in better test cell repeatability. This is because the higher stoichiometric ratios can greatly reduce liquid water content in the flow channel and consequently decrease the oscillation of the cell voltage. In addition, the worse test cell repeatability is observed in the conditions of high current density (1.0 A/cm^2) and lower operating temperatures and stoichiometric ratios, as the k-value is exceeded the 1% critical k-value in these operating conditions. This is because higher current densities can generate higher amounts of water, which will cause the voltage to oscillate more severely at lower temperatures and lower stoichiometric ratios. Generally speaking, most of the k-values of these test cells are below the critical k-value, which means a good level of precision can be achieved in most of the operating conditions. The results of between-cell consistency (Figure 4.4) indicate that a high level of trueness test results can be obtained from this type of test cell, as nearly all cells' h-values are staying within the critical h-value range. The difference between the h-values of four test cells may be caused by errors in cell assembly.

The variations of the repeatability/reproducibility standard deviation (S_r/ S_R) at different load changes and operating conditions were also investigated. The results show that both the S_r and S_R are highly influenced by the load change and stoichiometric ratio. It was found that the S_r and S_R were increased with the increase of the current density,

which has been explained before. However, a violation behavior was found that both the S_r and S_R, especially S_R, are higher at the lowest current density. The reason could be attributed to improper experimental procedures. At each temperature, the experiments were conducted continuously with three round load changes (e.g., A1-1 to A1-4, A2-1 to A2-4, and A3-1 to A3-4 in Figure 4.5), each round with specific stoichiometric ratio. When the first round was finished, the current density will be changed from 1.0 A/cm^2 to 0.2 A/cm^2, so the cell will be influenced by the higher amount of liquid water generated at higher current densities, and thus a higher voltage oscillation. During the 1-hour operation at 0.2 A/cm^2, the cell will gradually achieve its equilibrium and the S_r and S_R start to decrease when it moves to 0.2 A/cm^2. Overall, the results of this part imply that careful control of the cell assembly, proper test procedures and operating conditions are important to obtain reliable results.

The DoE study of the static behavior of the single PEFCs was analyzed in chapter 5. A split-plot factorial design was used to characterize the effect of the different operating factors on the responses of the cell voltage, cathodic pressure drop and voltage oscillation. The impacts of seven operating factors, namely: cell orientation (a), cell temperature (b), anodic/cathodic stoichiometric ratio (C/D), anodic/cathodic relative humidity (E/F) and backpressure (G), were investigated. The responses were sampled at current densities of 0.2 A/cm^2, 0.6 A/cm^2, 1.0 A/cm^2, and 1.2 A/cm^2, which are representing the low load, middle load, high load and extreme load conditions. The significant main factors and the significant interaction terms were determined via statistical analysis and visualized by the Pareto plots. The regression models regarding the selected responses were built according to the split-plot factorial design.

The results showed that, for the voltage response, the factors of temperature (b), cathodic stoichiometry ratio (D), backpressure (G) and the interaction factor bG are the significant factors at all current densities. At lower current densities (0.2 A/cm^2 and 0.6 A/cm^2) in Table 5.3, the main effect factor backpressure has the highest coefficient, which implies that the change of the backpressure makes the highest contribution for the cell voltage increases. This is because a lower amount of liquid water in the flow channels at lower current densities, and higher backpressure can improve the partial pressure of the reactants and facilitate the diffusion of the reactants to the catalyst layer. However, at higher current densities, the impact of backpressure on voltage was decreased and the factors of temperature and cathodic stoichiometric ratio became dominating among other factors. This is because more water was generated at high current densities and more liquid water was condensed in the flow channel. In this

situation, the higher temperature and higher stoichiometry ratio can not only increase the discharge speed of liquid water out of the fuel cell but also lead to a higher electrochemical reaction rate. The significant factors of temperature (b), cathodic stoichiometry ratio (D), backpressure (G) and the interaction factor DG were observed for the voltage oscillation responses in Table 5.5. The voltage oscillation is mainly caused by the liquid water situation inside the fuel cell, such as water slugs' movement in the flow channel. The temperature and stoichiometry ratio have negative effects on voltage oscillation and the backpressure has a positive effect on the voltage oscillation. A higher temperature and higher stoichiometry ratio can help to decrease the amount of liquid water in the fuel cell, and lower backpressure can help to decrease the liquid water condensation. Generally speaking, these three factors (temperature, stoichiometry ratio and backpressure) can influence the cell performance from both the electrochemical and water management point of view.

For the pressure drop response, apart from the liquid water conditions inside the flow channels, the pressure drop is also highly dependent on the cell operating conditions. The pressure drop response in Table 5.4 revealed that the stoichiometry ratio (D), and the backpressure (G) are the most important main factors for all current densities and their influence on the pressure drop can be explained by Equation 5.1. It was also found that the temperature (b) and cathode R.H. (F) became significant at higher current densities. Factor F has a positive impact on pressure drop. This is because more water was generated at higher current densities, and higher relative humidity can also introduce more water into the cell and thus a higher pressure drop. These results are also supported by the findings in Table 5.3 and Table 5.5, in which the cathode R.H. (F) was observed at higher current densities. It has a negative impact on both, voltage and voltage oscillation responses. The temperature factor should have a positive impact on the pressure drop. However, in a two-phase flow situation, a higher temperature can evaporate more liquid water into water vapor and thus decrease the pressure drop. In this situation, the temperature's positive and negative impact on pressure drop canceled each other out. That might be the reason why the temperature factor was not significant for the pressure drop at lower current densities. The temperature factor was only found significant at the highest current density of 1.2 A/cm^2. The reason might be that a lot of heat was generated at this high current density, and the high inlet gas flow rate made a dryer situation inside the cell compared to the lower current densities. In this situation, the temperature factor became significant enough to be added to the model.

During the analysis, the cell orientation (factor a) is considered not significant according to the results of the factorial design. The results of the center point examination (Figure 5.7) suggest that the curvature effect exists among these factors. However, due to the limitations of the factorial design, it cannot distinguish whether this curvature effect is caused by the cell orientation factor or other factors. In this situation, the RSM was applied and the second-order regression model regarding each response was built (Table 5.6-Table 5.8). The results imply that the cell orientation (factor a), temperature (factor b), and backpressure (factor G) have curvature effects on the selected responses.

The quadratic term of temperature (b^2) is observed at all current densities of the voltage response (Table 5.6). The coefficient of factor b^2 is negative, which implies that the highest voltage can be observed in this temperature range. It is easy to understand, that a higher temperature can lead to a higher electrochemical reaction rate and also can help to evaporate the liquid water into water vapor which could mitigate the risk of flooding. However, an excessive temperature will cause the membrane to become dehydrated, resulting in higher ohmic resistance and hence lower voltage.

The quadratic term of cell orientation (a^2) is relevant at all current densities of the pressure drop response (Table 5.7). The coefficient of factor a^2 is positive implies that the lowest pressure drop can be observed within the selected cell orientation range. According to the RSM optimization results, the best cell orientation is around 90° (vertical position). This is supported by the findings in the literature [156]. When the test cell is oriented vertically, the gravity effects can facilitate the removal of liquid water from the flow channel and this will be preferable for the water management of the fuel cell. And the lower pressure drop can also decrease the parasitic power of the fuel cell system. The discussion above is also supported by the results for voltage response (Table 5.6) and voltage oscillation response (Table 5.8). The factor a^2 is relevant at higher current densities of both voltage and voltage oscillation. The highest voltage and the lowest voltage oscillation can be obtained when the cell is in the vertical position, and this is validated in this experimental design space. The results in this part imply that the cell orientation is crucial for fuel cell water management, performance and stable operation and the best cell orientation is vertical position.

The quadratic term of cathode stoichiometry ratio (D^2) is observed at all current densities of the voltage oscillation response (Table 5.8). This is because that a higher inlet flow rate can help to remove the liquid water out of the flow channel and hence

decrease the voltage oscillation. When the amount of liquid water inside the flow channel is small enough, the effect of the inlet flow rate on voltage oscillation will be reduced. It should be noted that a higher inlet flow rate can also lead to dehydration of the membrane and thus the reduction of the cell voltage. However, the quadratic term D^2 is not observed in the voltage response, which implies that the stoichiometry ratio within the experimental design space is appropriate for the cell operation.

Finally, using the second-order regression model, maximum voltage, minimum pressure drop and voltage oscillation were achieved and corresponding optimized values of each operating condition were obtained. In realistic applications, these optimized response values can be treated as the criteria for a cell's operation. When a fuel cell is operated in a manner that deviates from the criteria, adjustment of each main significant factor and also the coordinated adjustment of their interaction factors (in the regression model) within the design space can be treated as an effective control strategy that can make the cell operation well.

The DoE study of the dynamic behavior of the single PEFCs was analyzed in chapter 6 (section 6.1). A split-plot factorial design was used to characterize the effect of the different operating factors on the responses of the voltage overshoot behavior and voltage undershoot behavior. The impacts of seven operating factors, namely: load change step (A), temperature (b), anodic/cathodic stoichiometric ratio (C/D), anodic/cathodic relative humidity (e/f) and backpressure (G), were investigated.

The regression models regarding the selected responses were illustrated in Table 6.2. It can be observed that the voltage overshoot value is smaller than the voltage undershoot value, and the number of significant factors and their coefficients in the overshoot regression model are all smaller than that of the voltage undershoot regression model. This is because the voltage overshoot behavior only occurs when the current shifts from its high value to its low value. The sudden decrease of the current leads to a decrease in the gas consumption rate. Moreover, the slower change of the gas supply is currently leading to a relatively high gas concentration at the reaction sites. However, for the voltage undershoot behavior, sudden current increases can lead to an increase in the gas consumption rate. At this moment, the rate of change in the gas supply is very slow compared to the electrochemical reaction rate and this will cause sudden gas starvation in the short run. Subsequently, the reactants will be transported to the reaction site until equilibrium is reached. During this period, the transport of the reactants is highly influenced by the water situation

inside the fuel cell, and thus the voltage undershoot behavior will relate to more operating factors.

It can be observed, from the voltage undershoot/overshoot regression model (Table 6.2), that an increase of the temperature (factor b), cathode stoichiometry ratio (factor D) and backpressure (factor G) can lead to a reduction of the voltage undershoot/overshoot value and thus improve the dynamic behavior of the test cell. Similarly, increasing these three factors can also improve the static behavior of the test cell. As discussed in Chapter 5, the optimized backpressure is set to 100 kPa, the optimized temperature is around 60-70°C and the optimized stoichiometry ratio is around 3.1-4.2, depending on different current densities. At static operation mode, the operating conditions should be maintained within optimum ranges to ensure that the cell can achieve the best static performance. When dealing with the dynamic behavior, in my opinion, the highest priority should be to adjust factor D to further improve the dynamic performance of the test cell. This is because the period for the load change is very short. It takes too long to change the temperature or/and backpressure and it may also result in an adverse influence on the static operation of the test cell. However, the adjustment of factor D is very flexible and the effect of the change in the short period of factor D on cell static operation may be negligible.

A key factor for the dynamic behavior is the load change step (factor A), especially for the voltage undershoot behavior. This is because a step-type large load change is more prone to cause reactant starvation in the fuel cell. This is due to the change of the electrochemical reaction rate, which is much faster than the change of the gas supply rate. Prolonging the load change duration can help to achieve the balance between the electrochemical reaction rate and the gas supply rate, and thus improve the dynamic behavior of the fuel cell. The additional experiments regarding the different load change profiles were operated and analyzed in section 6.2. In this section, four different load change ramps (with the different load change durations of 5 min, 2.5 min, 1 min, and 0 min) were studied. Also, each load change profile was cycled several times to simulate the load change conditions for real vehicular applications. The results show that the load profile with 0 min change duration (step function) leads to the highest voltage overshoot/undershoot magnitude compared to other load profiles. The load change with the ramp (5 min, 2.5 min, 1 min) can effectively decrease the voltage overshoot/undershoot magnitude. Further, it was observed that the load change ramp does not have an obvious influence on the average pressure drop and the membrane ohmic resistance, suggesting that the load change ramp has a limited effect on the

static behavior of the fuel cell. All of this information could help to improve the control strategy of the fuel cell system for real-life applications.

In this thesis, the interpretations of the experimental results are based on understanding mechanism of the LT-PEFC, the fluid dynamics, and also the learnings from literature. It is encouraged to conduct in-situ and ex-situ experiments with the help of X-ray or neutron radiography technologies in the future to have a full understanding of the mass transport situation inside the fuel cell. Furthermore, it was determined that the cell is preferred to be vertically positioned to get better performance. Based on this result, it would be interesting to study the flow field orientation on the cell performance in future investigations. At last, the results obtained in this thesis are based solely on our in-house-assembled single LT-PEFC, whether these results can fit the fuel cell with different components (CCMs, GDLs and flow fields), or even stacks is still a question and needs further investigation.

7 Discussion

8 Conclusions

Extensive experiments were performed to characterize the consistency of the in-house-assembled LT-PEFC and the effects of different operating conditions on the LT-PEFC's static and dynamic behavior. The key conclusions are as follows:

1) The performance of the in-house-assembled LT-PEMC shows a high level of repeatability and reproducibility.

2) The repeatability and reproducibility of the test cell not only can be affected by the cell assembling procedure but also can be influenced by the different operating conditions and experimental procedures.

3) Compared to the factors of temperature and relative humidity, the repeatability and reproducibility of the test cell are more sensitive to the factors of stoichiometry ratio and the current density.

4) The results of the DoE study on the static operation of LT-PEFC show that the statistically significant main factors are cell orientation (factor a), temperature (factor b), cathodic stoichiometry ratio (factor D), and backpressure (factor G).

5) After the RSM optimization process, the best cell orientation was determined to be positioned vertically, which implies that the gravity effects play a significant role in whether the fuel cell can be operated well and stable.

6) The second-order term of temperature (factor b^2), observed in the voltage quadratic regression model, implies that there exists a specific temperature value that can make the cell reach the maximum voltage. And this maximum value shifts according to different current densities.

7) The values of the required cathode stoichiometry ratio (factor D) to remove the liquid water in the flow channel were determined by the voltage oscillation quadratic regression model.

8) The value of each operating factor should be set according to the results of the RSM optimization process, to make sure that the test cell can achieve the best static operation performance.

9) The results of the DoE study on the dynamic operation of LT-PEFC show that the statistically significant main factors are: load change step (factor A), temperature (factor b), cathodic stoichiometry ratio (factor D), backpressure (factor G) and the relative humidity on both anode and cathode side (factor e and f).

10) Due to the fast response time, adjusting the cathodic stoichiometry ratio (factor D) is an effective way to improve the dynamic behavior of the fuel cell. And this method also has the minimum influence on the cell's static behavior.

8 Conclusions

11) The load change with the ramp can effectively improve the dynamic behavior of the LT-PEFC, and it has a limited impact on the static behavior of the LT-PEFC.

Appendix

A.1 The basic statistics calculations in chapter 4

The basic statistics of the test results include cell average value and standard deviation, which are calculated by the following equation:

$$\bar{y}_i = \sum_{k=1}^{n} y_{ik}/n \qquad\qquad \text{A.1}$$

and

$$s_i = \sqrt{\sum_{k=1}^{n}(y_{ik} - \bar{y}_i)^2/(n-1)} \qquad\qquad \text{A.2}$$

where:

$\bar{y}_i$:   average of test results for i_{th} test cell,

y_{ik}: k_{th} test results of the i_{th} test cell,

n: number of the test results of the i_{th} test cell, and

s_i: standard deviation for i_{th} test cell.

A.2 The intermediate statistics calculations in chapter 4

The intermediate statistics are calculated based on the basic statistics and are used for the calculation of the precision statistic. It includes the gross average, test cell deviation and the test cell average standard deviation.

The gross average

The gross average, $\bar{\bar{y}}$, is the average of all test cell averages at the same operating conditions, which can be expressed by the following equation:

$$\bar{\bar{y}} = \sum_{i=1}^{p} \bar{y}_i/p \qquad\qquad \text{A.3}$$

where:

$\bar{\bar{y}}$:   gross average,

$\bar{y}_i$:   average of test results for i_{th} test cell, and

p: number of the test cells.

The test cell deviation

The test cell deviation, d, represents the difference between the test cell average and gross average, which is expressed by the following equation:

Appendix

$$d_i = \bar{y}_i - \bar{\bar{y}} \qquad\qquad \text{A.4}$$

where:

d_i: deviation of the i_{th} test cell.

$\bar{y}_i, \bar{\bar{y}}$ have the same meaning as for equation A.3.

The test cell average standard deviation

$$s_{\bar{y}} = \sqrt{\sum_{i=1}^{p} d_i{}^2/(p-1)} \qquad\qquad \text{A.5}$$

where:

$s_{\bar{y}}$: the standard deviation of the test cell averages at the same operating conditions.

The precision statistics include the repeatability and reproducibility standard deviation.

Repeatability standard deviation

According to equation A.5, the repeatability standard deviation can be estimated by the following equation:

$$s_r = \sqrt{s_W^2} = \sqrt{\sum_{i=1}^{p} s_i{}^2/p} \qquad\qquad \text{A.6}$$

where:

s_r: repeatability standard deviation,

s_i: standard deviation for i_{th} test cell,

s_W^2: within-cell variance.

Reproducibility standard deviation

The reproducibility standard deviation can be estimated by the following equation:

$$s_R = \sqrt{s_B^2 + s_r^2} \qquad\qquad \text{A.7}$$

The estimated value of the between-cell variance, s_B^2, is calculated by:

$$s_B^2 = s_{\bar{y}}^2 - \frac{s_r^2}{n} \qquad\qquad \text{A.8}$$

where:

$s_{\bar{y}}^2$:   variance of the test cell average value.

Substituting s_B^2 into equation A.7 produces the following equation:

$$s_R = \sqrt{s_{\bar{y}}^2 + s_r^2 \frac{n-1}{n}} \qquad\qquad \text{A.9}$$

A.3   The critical k-value and critical h-value in chapter 4

The critical k-value

The critical k-value is used as a criterion to evaluate the seriousness of the data's spread deviation at a given significance level, which can be calculated by the following equation:

$$k_{crit} = \sqrt{\frac{p}{1 + (p-1)/F\{\alpha, v_1, v_2\}}} \qquad\qquad \text{A.10}$$

where:

k_{crit}:   critical k-value,

p: number of test cells,

$F\{\}$:   F-distribution value,

v_1, v_2:   degree of freedom, $v_1 = (n-1)(p-1), v_2 = (n-1)$, and

α: significance level, it is normally 5%.

The critical h-value

The critical h-value is used as a criterion to measure the seriousness of the data's deviation from the average at a given significance level, which can be calculated by the following equation:

$$h_{crit} = \pm \frac{(p-1)t\{\alpha, v\}}{\sqrt{p(t^2 + p - 2)}} \qquad\qquad \text{A.11}$$

where:

h_{crit}:   critical h-value,

p: number of test cells,

$t\{\}$:   t-distribution value,

v: degree of freedom, $v = (p-1)$, and

α: significance level, it is normally 5%.

A.4 The results of accuracy statistics in chapter 4

Table A.1: The accuracy statistics for each operating condition.

Operating conditions	$\bar{\bar{y}}$ (V)	$s_{\bar{y}}$ (V)	s_r (V)	s_R (V)	r (V)	R (V)
A1-1	0.7519	0.008325	0.005060	0.009729	0.014167	0.027241
A1-2	0.7002	0.008727	0.003687	0.009467	0.010324	0.026506
A1-3	0.6404	0.011012	0.003946	0.011691	0.011049	0.032735
A1-4	0.5819	0.011609	0.004196	0.012337	0.011750	0.034544
A2-1	0.7691	0.003352	0.004466	0.005566	0.012506	0.015585
A2-2	0.7113	0.004761	0.001182	0.004904	0.003310	0.013730
A2-3	0.6494	0.006791	0.001973	0.007069	0.005526	0.019794
A2-4	0.5908	0.009469	0.002389	0.009763	0.006689	0.027336
A3-1	0.7595	0.005750	0.010553	0.011972	0.029549	0.033521
A3-2	0.7013	0.008079	0.006407	0.010291	0.017939	0.028816
A3-3	0.6341	0.011562	0.007833	0.013943	0.021932	0.039042
A3-4	0.5650	0.014250	0.008974	0.016816	0.025126	0.047086
B1-1	0.7522	0.003521	0.007150	0.007938	0.020020	0.022226
B1-2	0.7043	0.005070	0.003878	0.006371	0.010857	0.017838
B1-3	0.6441	0.007369	0.003744	0.008257	0.010484	0.023119
B1-4	0.5777	0.010820	0.003910	0.011498	0.010948	0.032194
B2-1	0.7692	0.002372	0.003791	0.004456	0.010616	0.012477
B2-2	0.7166	0.003331	0.001132	0.003516	0.003169	0.009844
B2-3	0.6563	0.005155	0.001511	0.005369	0.004230	0.015034
B2-4	0.5958	0.007032	0.002007	0.007310	0.005619	0.020469
B3-1	0.7627	0.003377	0.011144	0.011591	0.031204	0.032455
B3-2	0.7096	0.003130	0.005987	0.006729	0.016763	0.018841
B3-3	0.6420	0.008671	0.007337	0.011335	0.020543	0.031738
B3-4	0.5657	0.012638	0.012660	0.017844	0.035449	0.049963
C1-1	0.7383	0.006373	0.006379	0.008994	0.017861	0.025183
C1-2	0.6788	0.006514	0.005289	0.008374	0.014809	0.023447
C1-3	0.6114	0.007933	0.005155	0.009447	0.014433	0.026451
C1-4	0.5388	0.010237	0.004844	0.011315	0.013563	0.031682
C2-1	0.7528	0.004060	0.005357	0.006700	0.014999	0.018761
C2-2	0.6877	0.006103	0.001616	0.006311	0.004524	0.017672
C2-3	0.6153	0.008510	0.002567	0.008885	0.007188	0.024878
C2-4	0.5449	0.011236	0.003246	0.011691	0.009090	0.032735
C3-1	0.7467	0.004835	0.015053	0.015739	0.042150	0.044069
C3-2	0.6821	0.006134	0.008301	0.010288	0.023243	0.028806
C3-3	0.6069	0.008149	0.009088	0.012172	0.025446	0.034083
C3-4	0.5196	0.010911	0.011203	0.015598	0.031368	0.043674

A.5   The raw data of test cell 3 in chapter 4.
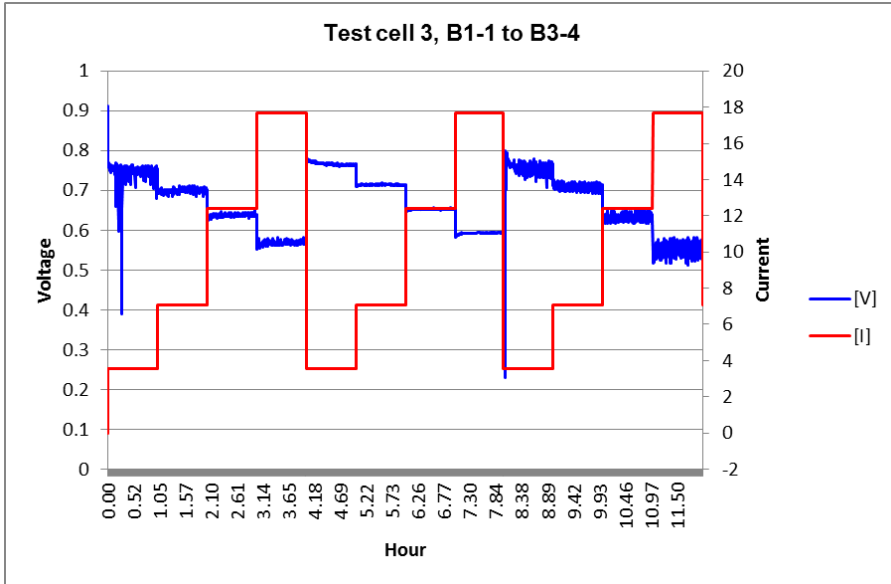
Figure A.1: The raw data of test cell 3 from B1-1 to B3-4.

A.6   Derivation for Equation 5.1 in chapter 5

The Darcy-Weisbach equation is widely used to calculate the pressure drop in the flow field, which can be expressed by the following equation [157]:

$$\Delta p = \lambda \frac{L}{D_h} \frac{\rho_{mix} \bar{v}^2}{2}$$

A.12

where:

λ: friction factor,

L: length of the flow channel,

D_h: hydraulic diameter of the flow channel,

ρ_{mix}:   mixture (air and water vapor) density,

$\bar{v}$:   mixture flow velocity.

Friction factor λ can be expressed by the following equation [158]:

$$\lambda = \frac{64}{Re}$$

A.13

where:

Re: Reynolds number.

Reynolds number can be expressed by the following equation [158]:

Appendix

$$Re = \frac{\rho D_h \bar{v}}{\mu_{mix}}$$

A.14

where:

μ_{mix}: mixture viscosity.

Substituting λ and Re into Equation A.12 produces the following equation:

$$\Delta p = \frac{32 \mu_{mix} \bar{v} L}{D_h^2}$$

A.15

where:

$\bar{v}$: mixture flow velocity.

The relationship between flow velocity and mass flow rate can be expressed by:

$$Q_m / n = \rho_{mix} A \bar{v}$$

A.16

where:

Q_m: mixture mass flow rate,

n: number of flow channels,

A: cross-section area of the flow channel.

Substituting $\bar{v}$ (in Equation A.16) into Equation A.15, the following equation is generated:

$$\Delta p = \frac{32L}{nAD_h^2} \cdot \frac{\mu_{mix}}{\rho_{mix}} \cdot Q_m$$

A.17

The mixture mass flow rate, Q_m, is the combination of the dry air mass flow rate and the water vapor mass flow rate, which can be expressed by the following equation:

$$Q_m = Q_a (1 + \frac{18 \phi P_{sat}}{29 P_a})$$

A.18

where:

Q_m: mixture mass flow rate,

Q_a: dry air mass flow rate,

ϕ: mixture relative humidity,

P_{sat}: saturation pressure,

P_a: mixture inlet pressure.

The mixture viscosity, μ_{mix} (Pa·s), is correlated with the temperature (K), which can be expressed by the following equation [154]:

$$\mu_{mix} = 4.842 \times 10^{-7} T^{0.6392}$$

A.19

The mixture density, ρ_{mix}, can be expressed by:

$$\rho_{mix} = \frac{29 P_a + 18 \phi P_{sat}}{RT}$$

A.20

where:

P_a: mixture inlet pressure.

P_{sat}:   saturation pressure,

R: the gas constant,

ϕ: mixture relative humidity

Combining Equations A.17-A.20, the pressure drop equation can be hence expressed by [154]:

$$\Delta p = 1.15 \times 10^{-11} \frac{L}{nAD_h{}^2} \frac{RT}{P_a - \phi P_{sat}} Q_v \qquad \text{A.21}$$

where:

T: test cell temperature,

Q_v: mixture volume flow rate.

A.7   The validation of the pressure drop regression model in chapter 5

Figure A.2 illustrates the normal plot of Residuals (Figures A.2a, A.2c, A.2e and A.2g) and Residuals versus run order (Figures A.2b, A.2d, A.2f and A.2h) for pressure drop response at current densities of 0.2 A/cm², 0.6 A/cm², 1.0 A/cm², 1.2 A/cm². Some residuals are not ideally located on the straight line in Figures A.2a and A.2c. However, as aforementioned, a mild violation is still acceptable. Overall, it can be inferred from Figure A.2 that the residuals are normally distributed, and also independent of each other. The pressure drop regression models are well validated.
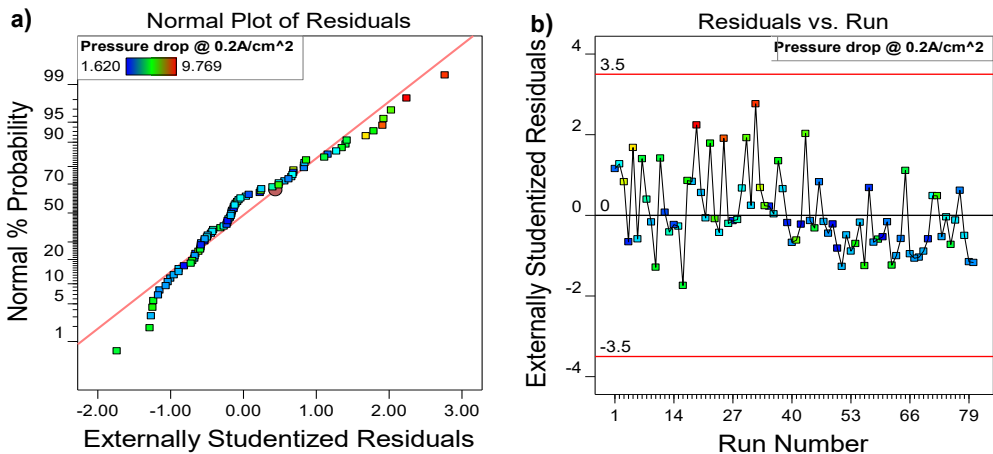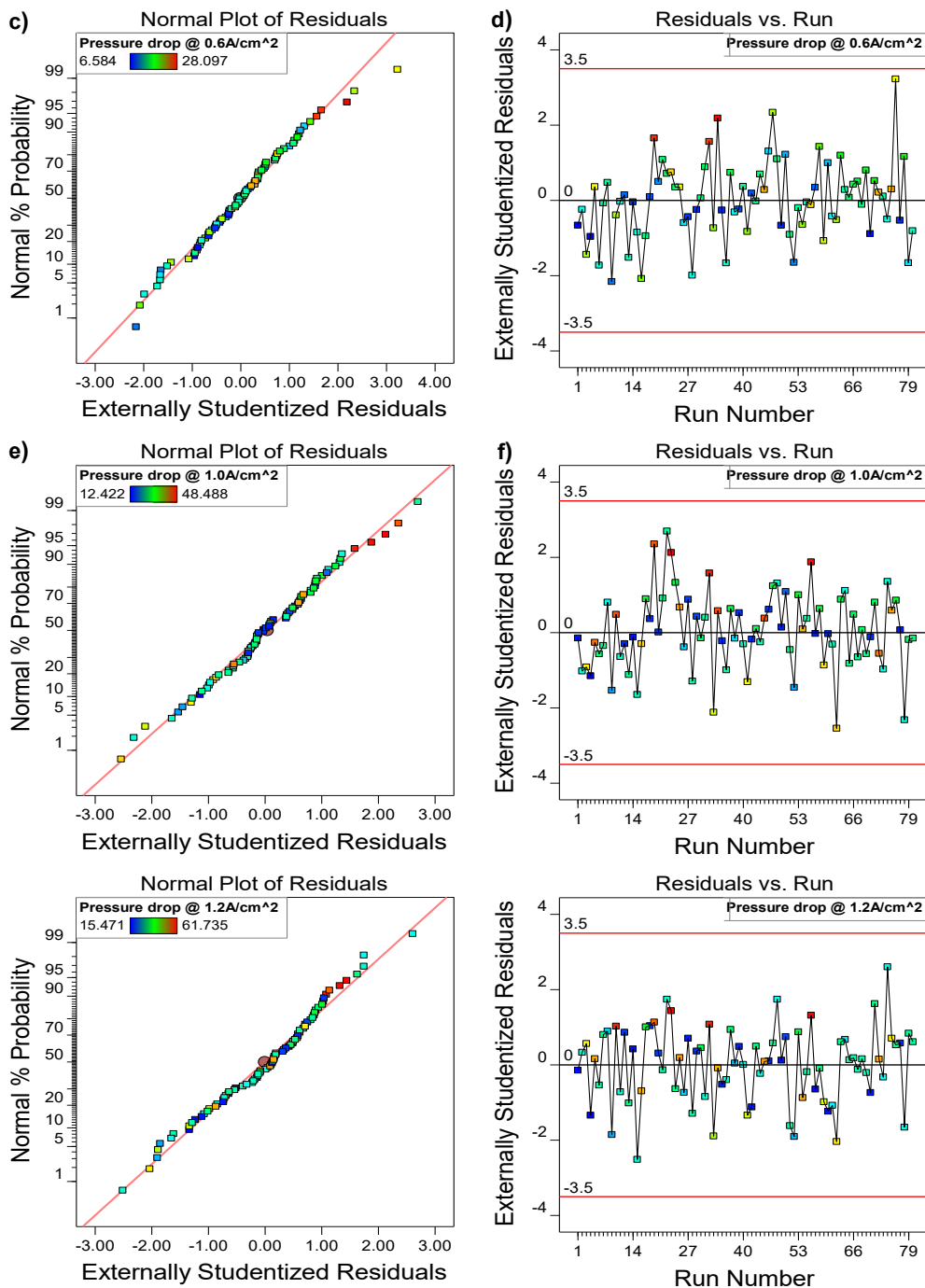
Figure A.2: Normal plot of Residuals and Residuals vs. run order for pressure drop response at current densities of 0.2 A/cm^2, 0.6 A/cm^2, 1.0 A/cm^2, 1.2 A/cm^2.

A.8 The validation of the voltage oscillation regression model in chapter 5

Figure A.3 illustrates the normal plot of Residuals (Figure A.3a, A.3c, A.3e and A.3g) and Residuals versus run order (Figure A.3b, A.3d, A.3f and A.3h) for voltage oscillation response at current densities of 0.2 A/cm², 0.6 A/cm², 1.0 A/cm², 1.2 A/cm². Some residuals are not ideally located on the straight line. However, as aforementioned, a mild violation is still acceptable. Overall, it can be inferred from Figure A.3 that the residuals are normally distributed, and also independent of each other. The voltage oscillation regression models are well validated.
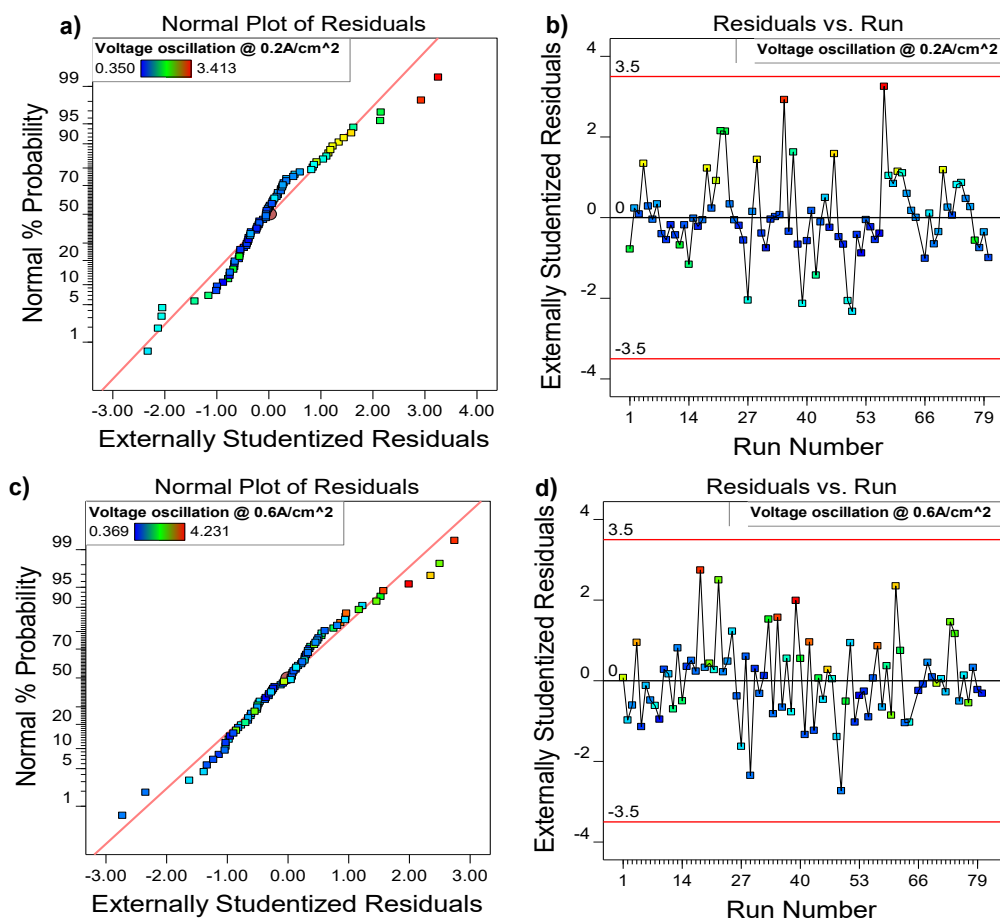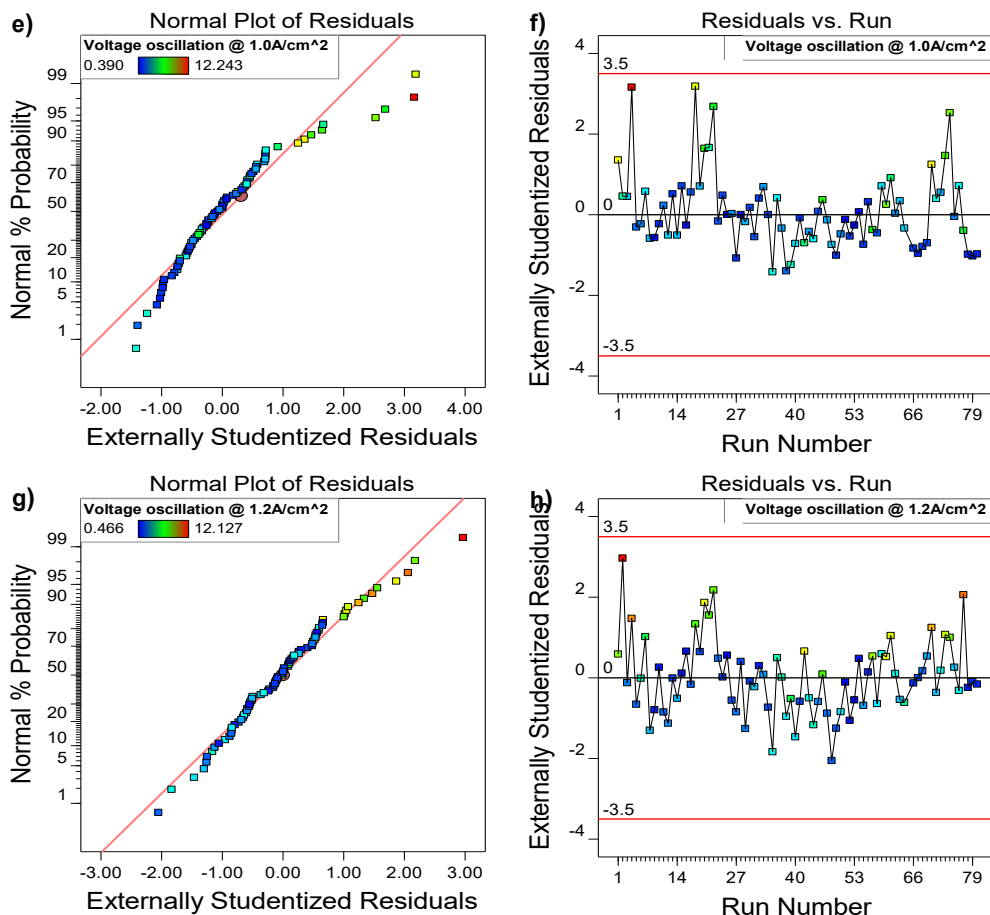
Figure A.3: Normal plot of Residuals and Residuals vs. run order for voltage oscillation response at current densities of 0.2 A/cm^2, 0.6 A/cm^2, 1.0 A/cm^2, 1.2 A/cm^2.

A.9   Design matrix of RSM study in chapter 5

The first column in Table A.2 shows the standard order of the tests, and the rest of the columns illustrate the significant factors which were obtained from the two-level factorial design, respectively. Tests 1-32 represent the two-level factorial design based on the five significant factors, which are used for estimating the coefficients on the linear and interaction terms of the regression model. Tests 33-42 represent 'star-point' tests, which are used for calculating the quadratic terms in the regression model. Tests 43-51 represent nine repeated center-points tests, which are used for calculating replicated true error.

Table A.2: The design matrix of RSM study.

Standard order	Cell positon (°)	Temperature (°C)	Cathode Stoi.	Cathode R.H. (%)	Backpressure (kPa)
1	0	50	2.5	50	0
2	0	50	4.5	50	0
3	0	50	2.5	90	0
4	0	50	4.5	90	0
5	0	50	2.5	50	100
6	0	50	4.5	50	100
7	0	50	2.5	90	100
8	0	50	4.5	90	100
9	180	50	2.5	50	0
10	180	50	4.5	50	0
11	180	50	2.5	90	0
12	180	50	4.5	90	0
13	180	50	2.5	50	100
14	180	50	4.5	50	100
15	180	50	2.5	90	100
16	180	50	4.5	90	100
17	0	70	2.5	50	0
18	0	70	4.5	50	0
19	0	70	2.5	90	0
20	0	70	4.5	90	0
21	0	70	2.5	50	100
22	0	70	4.5	50	100
23	0	70	2.5	90	100
24	0	70	4.5	90	100
25	180	70	2.5	50	0
26	180	70	4.5	50	0
27	180	70	2.5	90	0
28	180	70	4.5	90	0
29	180	70	2.5	50	100
30	180	70	4.5	50	100
31	180	70	2.5	90	100
32	180	70	4.5	90	100
33	0	60	3.5	70	50
34	180	60	3.5	70	50
35	90	50	3.5	70	50
36	90	70	3.5	70	50
37	90	60	2.5	70	50
38	90	60	4.5	70	50
39	90	60	3.5	50	50
40	90	60	3.5	90	50
41	90	60	3.5	70	0
42	90	60	3.5	70	100
43	90	60	3.5	70	50
44	90	60	3.5	70	50

45	90	60	3.5	70	50
46	90	60	3.5	70	50
47	90	60	3.5	70	50
48	90	60	3.5	70	50
49	90	60	3.5	70	50
50	90	60	3.5	70	50
51	90	60	3.5	70	50

A.10 The validation of the quadratic regression models in chapter 5

a) Normal Plot of Residuals

b) Residuals vs. Run

c) Normal Plot of Residuals
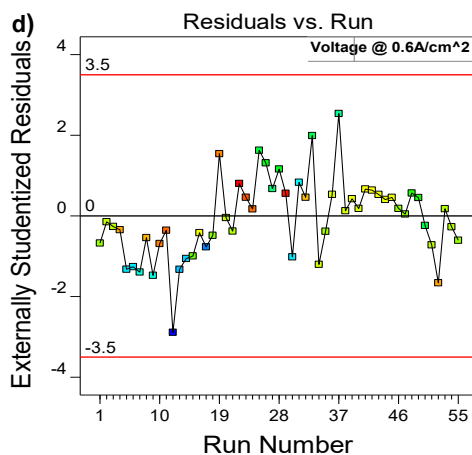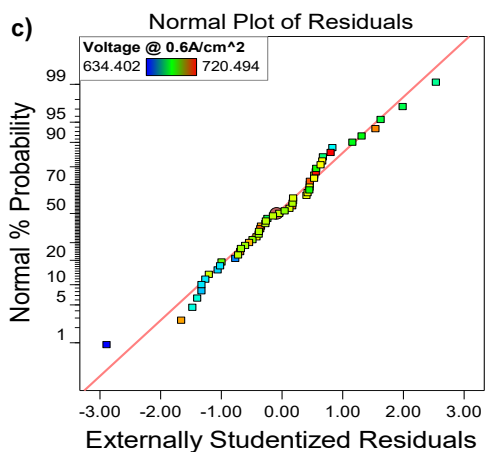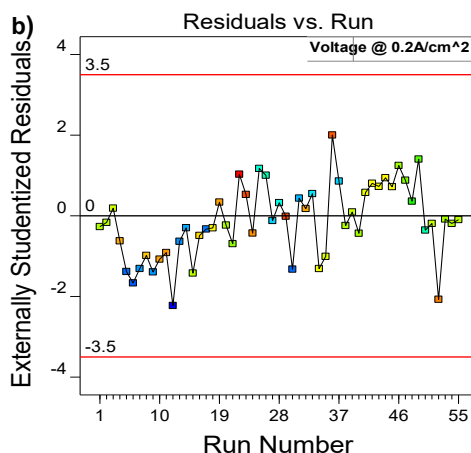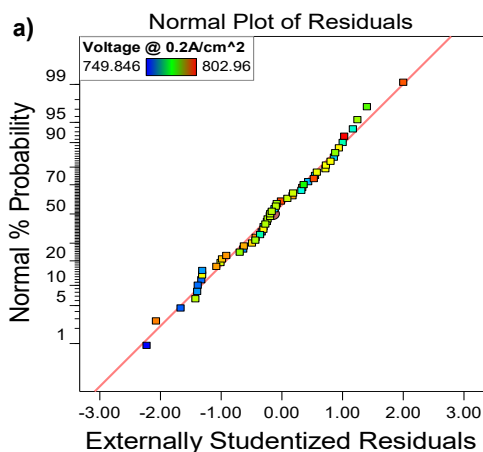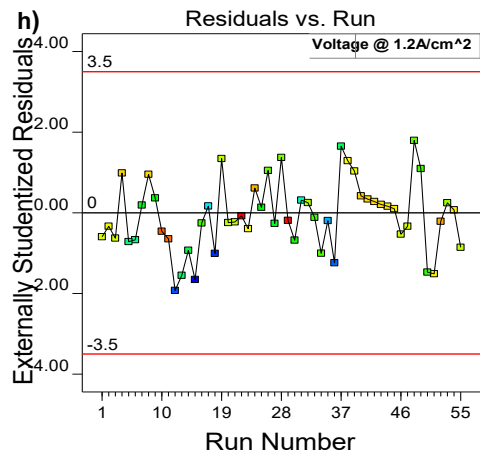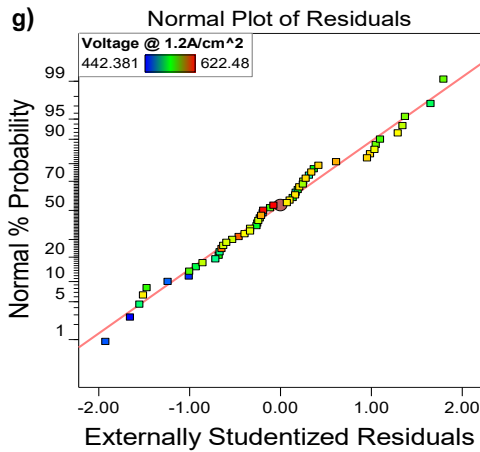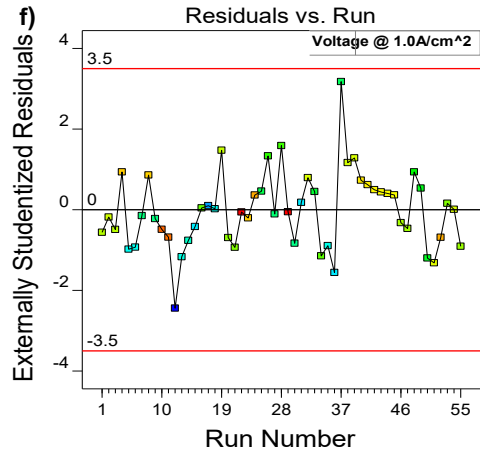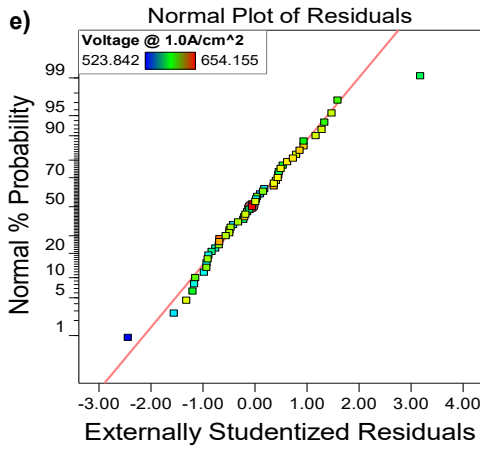
d) Residuals vs. Run

Figure A.4: Normal Residuals plots and Residuals vs. run order for voltage response quadratic regression model at the current densities of 0.2 A/cm^2, 0.6 A/cm^2, 1.0 A/cm^2, 1.2 A/cm^2.
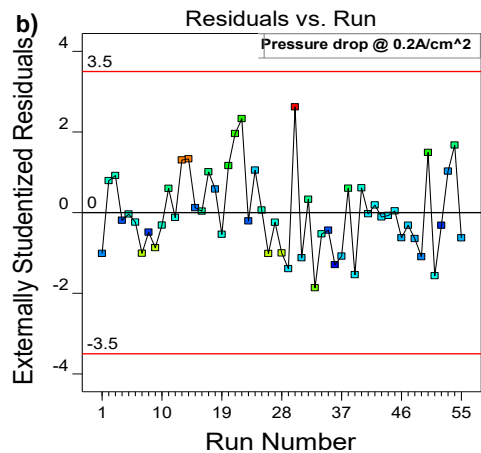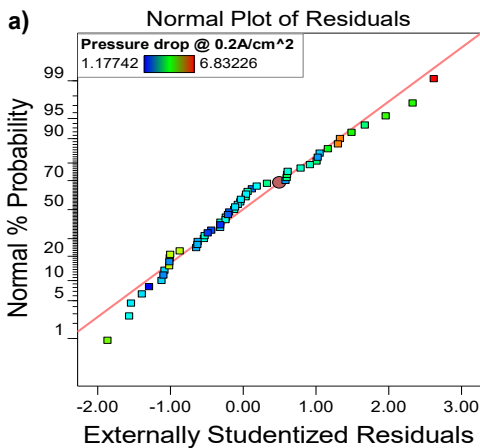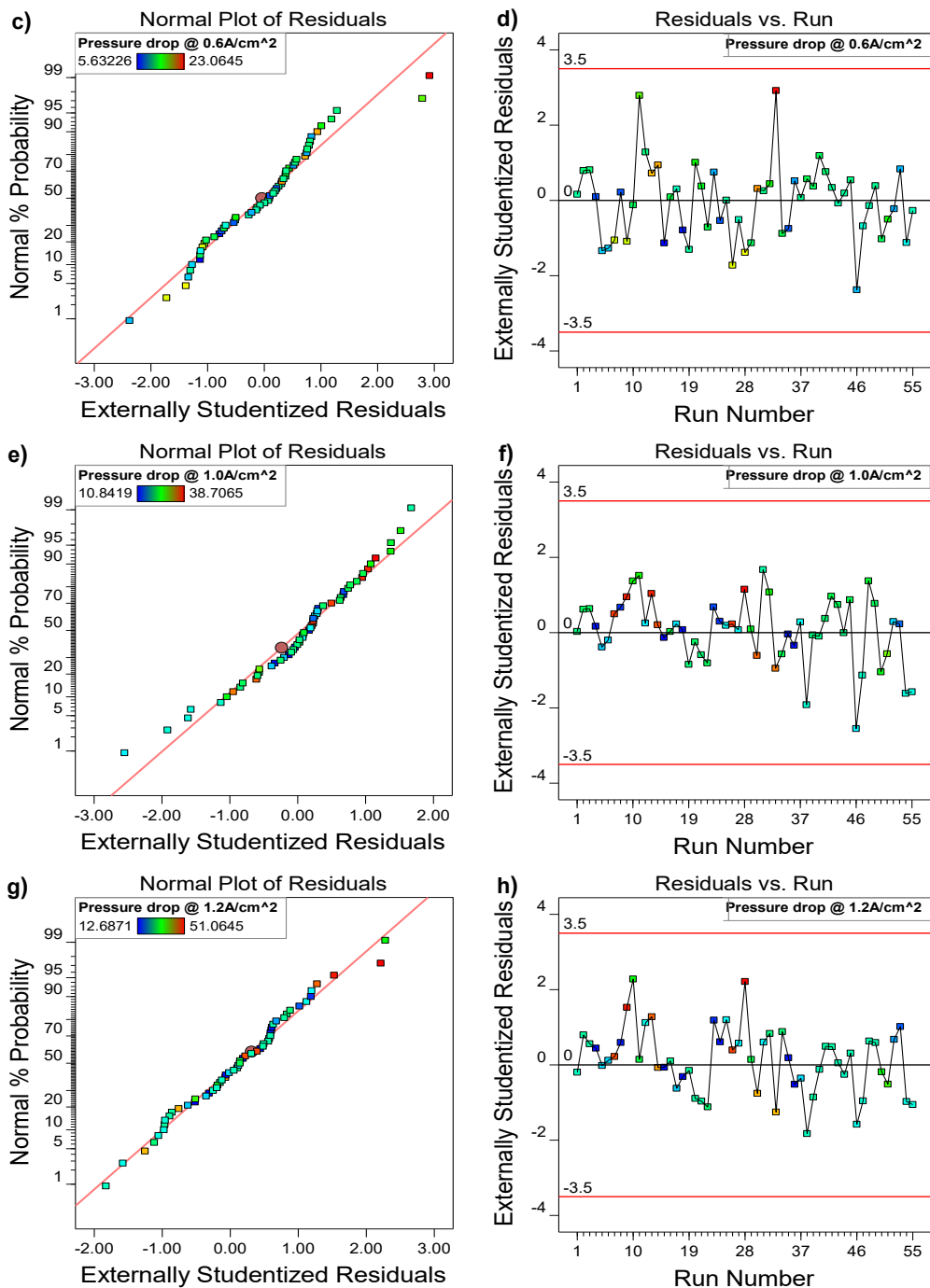
Figure A.5: Normal plot of Residuals and Residuals vs. run order for pressure drop response quadratic regression model at the current densities of 0.2 A/cm^2, 0.6 A/cm^2, 1.0 A/cm^2, 1.2 A/cm^2.

g)

h)
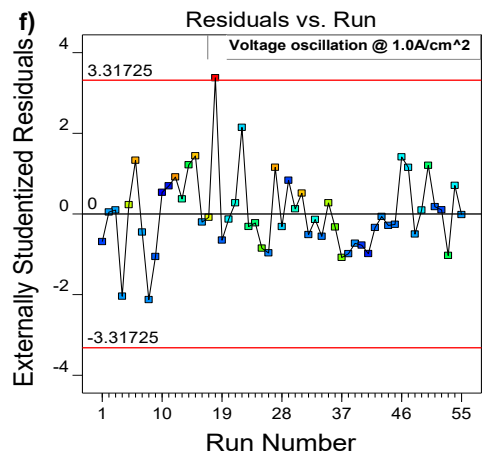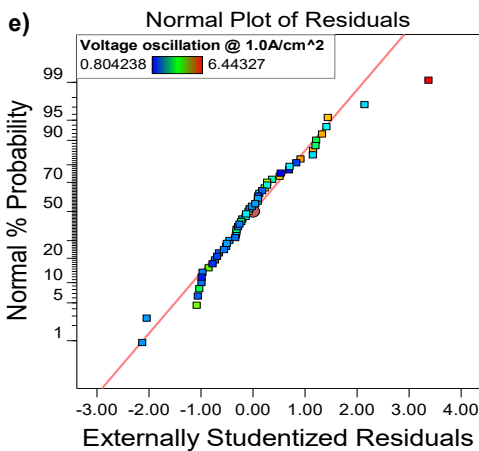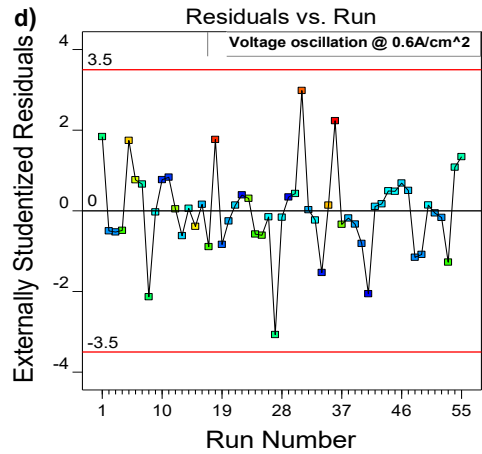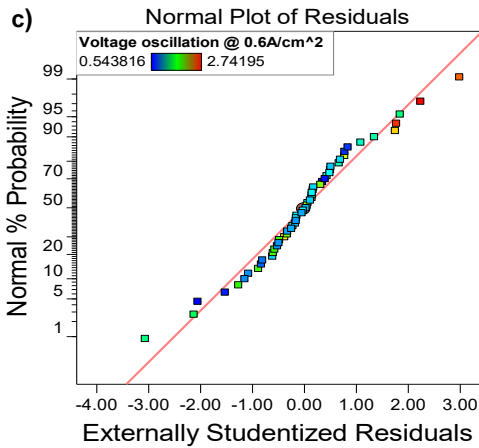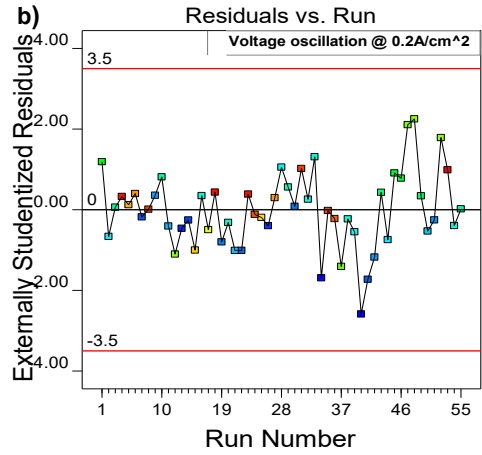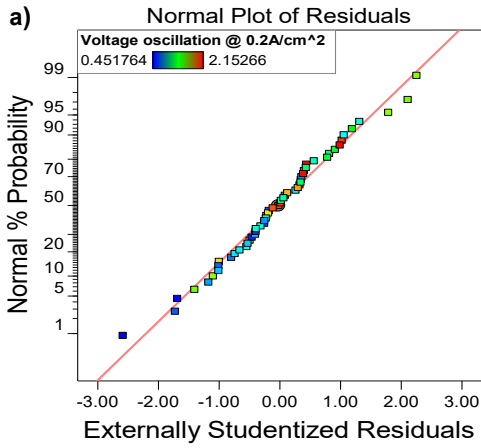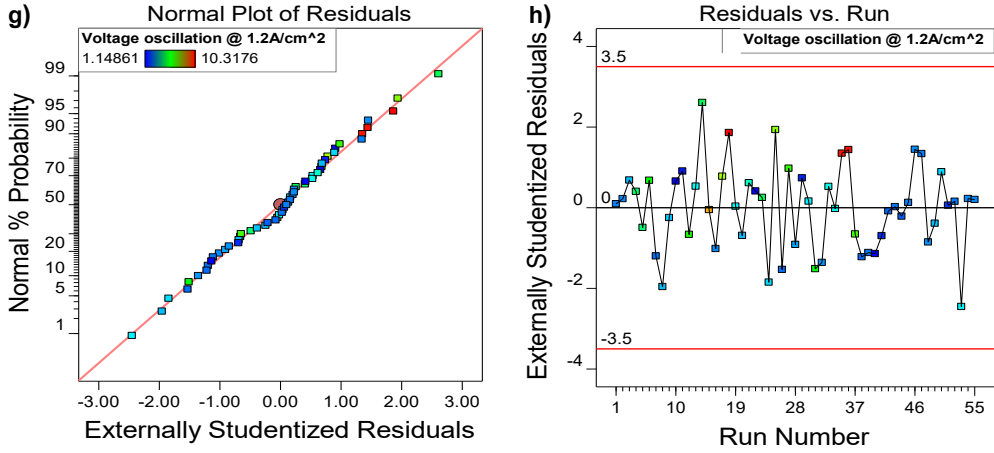
Figure A.6: Normal plot of Residuals and Residuals vs. run order for voltage oscillation response quadratic regression model at the current densities of 0.2 A/cm^2, 0.6 A/cm^2, 1.0 A/cm^2, 1.2 A/cm^2.

A.11 The validation of the dynamic regression models in chapter 6

a)

b)
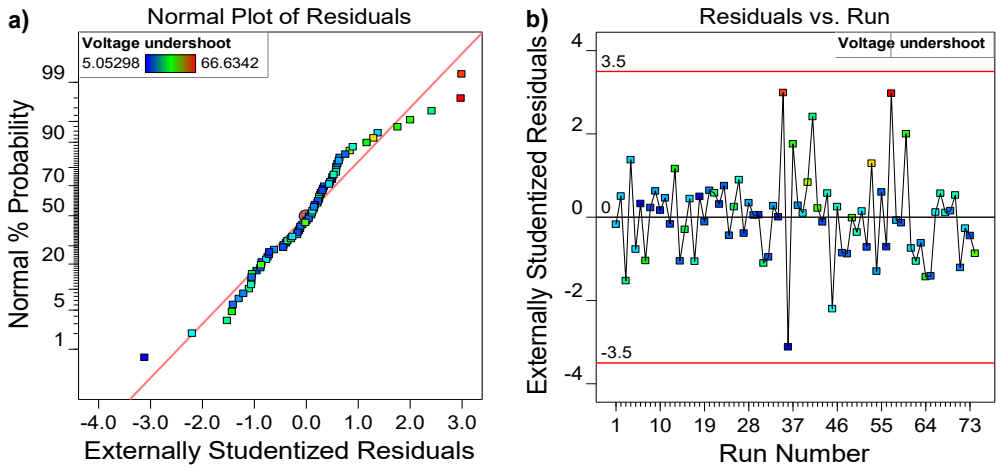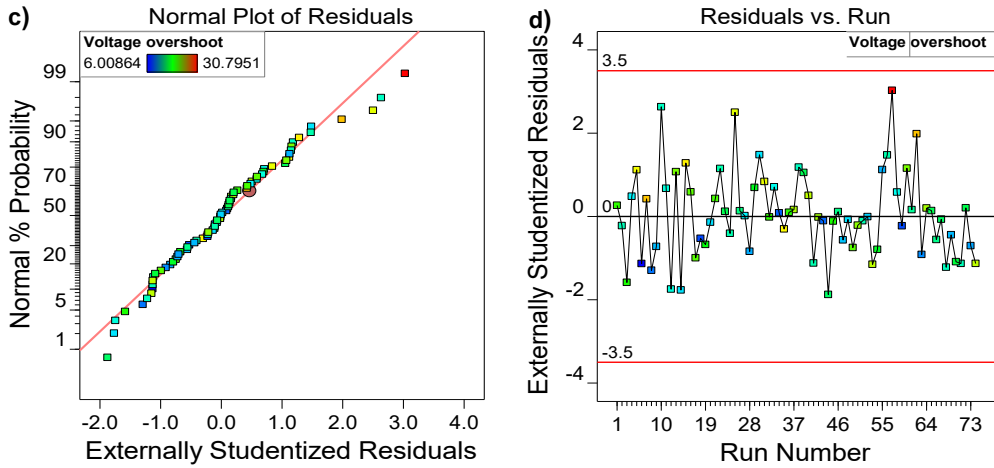
Figure A.7: Normal plot of Residuals and Residuals vs. run for voltage undershoot regression models a) and b) and overshoot regression models c) and d).

A.12 The experimental results of test No.1 to test No.2 in chapter 6

The cell voltage response and cathodic pressure drop response of test No. 1 to test No. 4 are illustrated in Figure A.8. The red line is the cell voltage, the black line represents the current density, and the green line is the pressure drop.
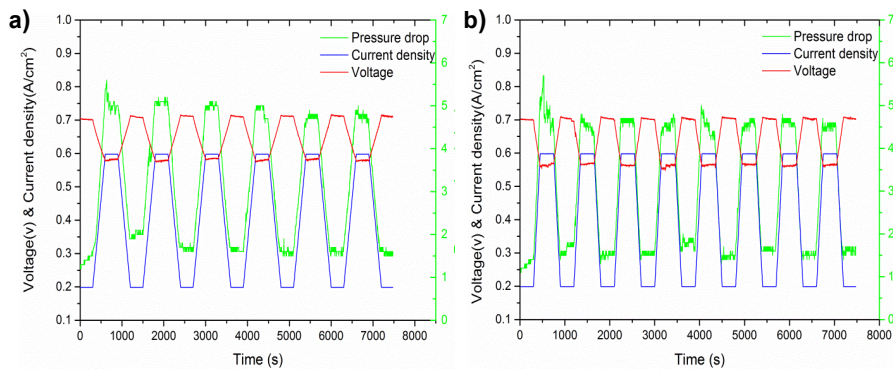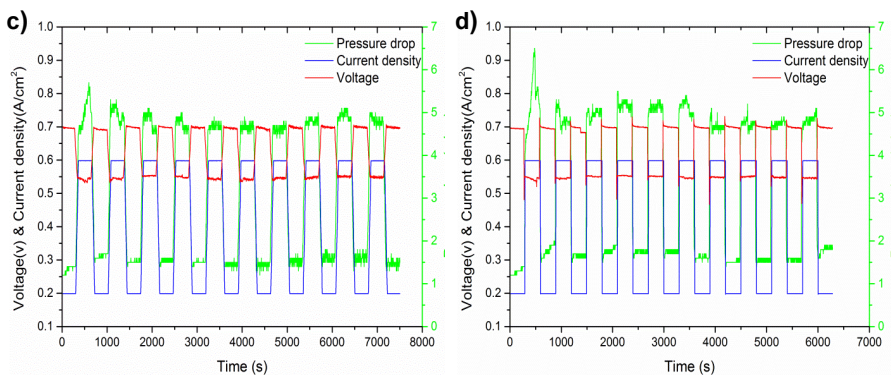
Figure A.8: The results of voltage response and cathodic pressure drop response in a) test No. 1, b) test No. 2, c) test No. 3, d) test No. 4.

A.13 The factors that are not selected in Pareto Chart in chapter 5

An example of the factors that exceed the t-value limit but are still not considered as the significant factors is shown in Figure A.9. In Figure A.9 g), four factors exceed the t-value limit but are not selected, which are factor 5 (abCDEG), factor 6 (CDF), factor 8 (CFG) and factor 9 (EFG). The factors from numbers 10 to 21 that are below the t-value limit are considered not significant. In Figure A.9 h), factor 2 (ab) and factor 3 (a) are below the t-value limit are considered not significant.
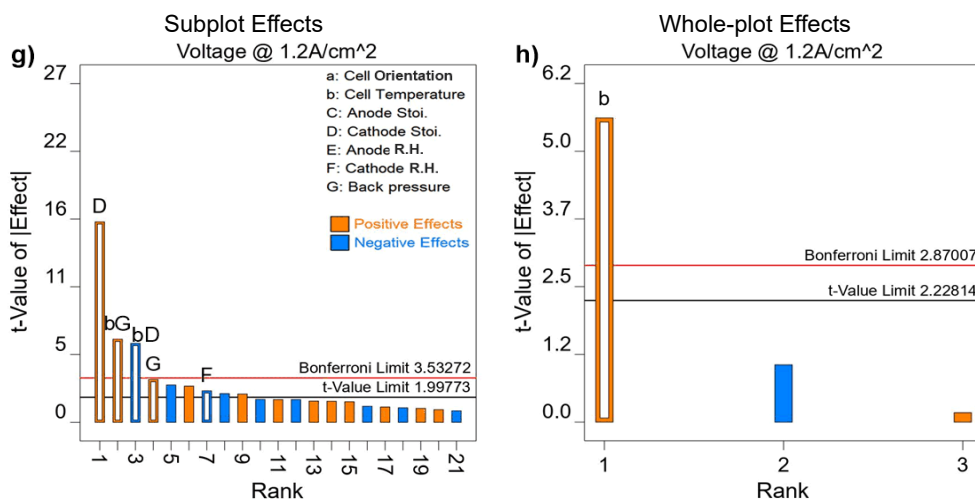
Figure A.9: The Pareto chart of the voltage response at current density of 1.2 A/cm^2.

Reference

[1]   OECD, Energy, OECD Green Growth Studies, 2012. https://doi.org/doi.org/10.1787/9789264115118-en.

[2]   IEA, Key World Energy Statistics 2020, Int. Energy Agency. 33 (2020) 4649. https://www.iea.org/reports/key-world-energy-statistics-2020.

[3]   Y. Liu, W. Lehnert, H. Janßen, R.C. Samsun, D. Stolten, A review of high-temperature polymer electrolyte membrane fuel-cell (HT-PEMFC)-based auxiliary power units for diesel-powered road vehicles, J. Power Sources. 311 (2016) 91–102. https://doi.org/10.1016/j.jpowsour.2016.02.033.

[4]   Y. Wang, K.S. Chen, J. Mishler, S.C. Cho, X.C. Adroher, A review of polymer electrolyte membrane fuel cells: Technology, applications, and needs on fundamental research, Appl. Energy. 88 (2011) 981–1007. https://doi.org/10.1016/j.apenergy.2010.09.030.

[5]   B. Emonts, L. Blum, T. Grube, W. Lehnert, J. Mergel, M. Müller, R. Peters, Technical Advancement of Fuel-Cell Research and Development, in: Fuel Cell Sci. Eng. Mater. Process. Syst. Technol., 2012: pp. 1–42. https://doi.org/10.1002/9783527650248.ch1.

[6]   S. Bhatt, B. Guptaa, V. Sethib, M. Pandeyb, Polymer Exchange Membrane (PEM) Fuel Cell: A Review, Int. J. Curr. Eng. Technol. 2 (2012) 219–226. http://inpressco.com/wp-content/uploads/2012/03/Paper13219-226.pdf.

[7]   W. Dönitz, Fuel cells for mobile applications, status, requirements and future application potential, Int. J. Hydrogen Energy. 23 (1998) 611–615. https://doi.org/10.1016/s0360-3199(97)00075-x.

[8]   M.W. Ellis, M.R. Von Spakovsky, D.J. Nelson, Fuel Cell Systems: Efficient, Flexible Energy Conversion for the 21st Century, Proc. IEEE. 89 (2001) 1808–1817. https://doi.org/10.1109/5.975914.

[9]   O.Z. Sharaf, M.F. Orhan, An overview of fuel cell technology: Fundamentals and applications, Renew. Sustain. Energy Rev. 32 (2014) 810–853. https://doi.org/10.1016/j.rser.2014.01.012.

[10]   F. Barbir, Chapter One - Introduction, in: F. Barbir (Ed.), PEM Fuel Cells, Second Edi, Academic Press, Boston, 2013: pp. 1–16. https://doi.org/10.1016/B978-0-12-387710-9.00001-1.

[11]   G. Wand, Fuel cell history, Part one, Fuel Cell Today, Arch. Artic. 6 (2006) 14.

[12]   J.M. Andújar, F. Segura, Fuel cells: History and updating. A walk along two centuries, Renew. Sustain. Energy Rev. 13 (2009) 2309–2322. https://doi.org/10.1016/j.rser.2009.03.015.

[13]   M.L. Perry, T.F. Fuller, A Historical Perspective of Fuel Cell Technology in the 20th Century, J. Electrochem. Soc. 149 (2002) S59. https://doi.org/10.1149/1.1488651.

[14]   N. Sazali, W.N.W. Salleh, A.S. Jamaludin, M.N.M. Razali, New perspectives on fuel cell technology: A brief review, Membranes (Basel). 10 (2020). https://doi.org/10.3390/membranes10050099.

[15]   M. Wei, S.J. Smith, M.D. Sohn, Analysis of Fuel Cell Markets in Japan and the US : Experience Curve Development and Cost Reduction Disaggregation, Lawrence Berkeley Natl. Lab. (2016).

[16]   D. Hart, F. Lehner, S. Jones, J. Lewis, The Fuel Cell Industry Review 2019,

E4tech. (2019) 1–52.

[17]   D. Hart, F. Lehner, S. Jones, J. Lewis, The Fuel Cell Industry Review 2015, E4tech. (2015) 1–52.

[18]   J. Larminie, A. Dicks, Fuel Cell Systems Explained, J. Wiley Chichester, UK, 2003.

[19]   W.G.C. Ryan O'hayre, Suk-Won Cha, Fuel Cell Fundamentals, John Wiley & Sons, 2016. https://doi.org/10.1017/CBO9781107415324.004.

[20]   F. Barbir, PEM Fuel Cells Theory and Practice, Academic Press, 2012.

[21]   S.P.S. Badwal, S.S. Giddey, C. Munnings, A.I. Bhatt, A.F. Hollenkamp, Emerging electrochemical energy conversion and storage technologies, Front. Chem. 2 (2014) 1–28. https://doi.org/10.3389/fchem.2014.00079.

[22]   F. Wang, C. Gao, S. Li, Impacts of power management on a PEMFC electric vehicle, Int. J. Hydrogen Energy. 39 (2014) 17336–17346. https://doi.org/10.1016/j.ijhydene.2014.08.052.

[23]   J. Zhang, PEM Fuel Cell Electrocatalysts and Catalyst Layers, Springer Science & Business Media, 2008.

[24]   M. V Williams, H.R. Kunz, J.M. Fenton, Analysis of Polarization Curves to Evaluate Polarization Sources in Hydrogen / Air PEM Fuel Cells, J. Electrochem. Soc. 152 (2005) A635–A644. https://doi.org/10.1149/1.1860034.

[25]   J.J. Giner-Sanz, E.M. Ortega, V. Pérez-Herranz, Hydrogen crossover and internal short-circuit currents experimental characterization and modelling in a proton exchange membrane fuel cell, Int. J. Hydrogen Energy. 39 (2014). https://doi.org/10.1016/j.ijhydene.2014.06.157.

[26]   S.S. Kocha, J.D. Yang, J.S. Yi, Characterization of Gas Crossover and Its Implications in PEM Fuel Cells, AIChE J. 52 (2006). https://doi.org/10.1002/aic.10780.

[27]   E. Padgett, G. Kleen, Automotive Fuel Cell Targets and Status, DOE Hydrog. Fuel Cells Progr. Rec. (2020) 5. https://www.hydrogen.energy.gov/pdfs/20005-automotive-fuel-cell-targets-status.pdf.

[28]   A. Wilson, G. Kleen, D. Papageorgopoulos, Fuel Cell System Cost - 2017, DOE Hydrog. Fuel Cells Progr. Rec. (2017) 12.

[29]   J. Wu, X. Zi, J.J. Martin, H. Wang, J. Zhang, J. Shen, S. Wu, W. Merida, A review of PEM fuel cell durability : Degradation mechanisms and mitigation strategies, J. Power Sources. 184 (2008) 104–119. https://doi.org/10.1016/j.jpowsour.2008.06.006.

[30]   J. Wang, System integration , durability and reliability of fuel cells : Challenges and solutions, Appl. Energy. 189 (2017) 460–479. https://doi.org/10.1016/j.apenergy.2016.12.083.

[31]   T. Van Nguyen, M.W. Knobbe, A liquid water management strategy for PEM fuel cell stacks, J. Power Sources. 114 (2003) 70–79. https://doi.org/10.1016/S0378-7753(02)00591-8.

[32]   B.S. Pivovar, An overview of electro-osmosis in fuel cell polymer electrolytes, Polmer. 47 (2006) 4194–4202. https://doi.org/10.1016/j.polymer.2006.02.071.

[33]   L. Alamos, The water content dependence of electro-osmotic drag in proton-conducting polymer electrolytes, Electrochim. Acta. 40 (1995) 297–302.

[34]   T.A. Zawodzinski, J. Electrochem, T.A. Zawodzinski, C. Derouin, S. Radzinski,

R.J. Sherman, V.T. Smith, T.E. Springer, S. Gottesfeld, Water Uptake by and Transport Through Nation | 117 Membranes, J. Electrochem. Soc. (1993).

[35]	S. Kim, M.M. Mench, Investigation of temperature-driven water transport in polymer electrolyte fuel cell : Thermo-osmosis in membranes, J. Memb. Sci. 328 (2009) 113–120. https://doi.org/10.1016/j.memsci.2008.11.043.

[36]	Z. Dunbar, R.I. Masel, Quantitative MRI study of water distribution during operation of a PEM fuel cell using Teflon® flow fields, J. Power Sources. 171 (2007) 678–687. https://doi.org/10.1016/j.jpowsour.2007.06.207.

[37]	K. Jiao, X. Li, Water transport in polymer electrolyte membrane fuel cells, Prog. Energy Combust. Sci. 37 (2011) 221–291. https://doi.org/10.1016/j.pecs.2010.06.002.

[38]	G. Park, Y. Sohn, T. Yang, Y. Yoon, W. Lee, C. Kim, Effect of PTFE contents in the gas diffusion media on the performance of PEMFC, J. Power Sources. 131 (2004) 182–187. https://doi.org/10.1016/j.jpowsour.2003.12.037.

[39]	A. Jayakumar, S.P. Sethu, M. Ramos, J. Robertson, A. Al-Jumaily, A technical review on gas diffusion, mechanism and medium of PEM fuel cell, Ionics (Kiel). 21 (2015) 1–18. https://doi.org/10.1007/s11581-014-1322-x.

[40]	S. Litster, D. Sinton, N. Djilali, Ex situ visualization of liquid water transport in PEM fuel cell gas diffusion layers, J. Power Sources. 154 (2006) 95–105. https://doi.org/10.1016/j.jpowsour.2005.03.199.

[41]	I. Manke, C. Hartnig, M. Grünerbel, W. Lehnert, N. Kardjilov, A. Haibel, A. Hilger, J. Banhart, H. Riesemeier, Investigation of water evolution and transport in fuel cells with high resolution synchrotron x-ray radiography, Appl. Phys. Lett. 90 (2007). https://doi.org/10.1063/1.2731440.

[42]	J. Le Canut, J.E. Soc, Detection of Membrane Drying , Fuel Cell Flooding, and Anode Catalyst Poisoning on PEMFC Stacks by Electrochemical Impedance Spectroscopy, J. Electrochem. Soc. 153 (2006) A857. https://doi.org/10.1149/1.2179200.

[43]	D.G. Sanchez, P.L. Garcia-ybarra, PEMFC operation failure under severe dehydration, Int. J. Hydrogen Energy. 37 (2012) 7279–7288. https://doi.org/10.1016/j.ijhydene.2011.11.059.

[44]	H. Li, Y. Tang, Z. Wang, Z. Shi, S. Wu, D. Song, J.J. Zhang, K. Fatih, J.J. Zhang, H. Wang, Z. Liu, R. Abouatallah, A. Mazza, A review of water flooding issues in the proton exchange membrane fuel cell, J. Power Sources. 178 (2008) 103–117. https://doi.org/10.1016/j.jpowsour.2007.12.068.

[45]	I.S. Hussaini, C. Wang, Visualization and quantification of cathode channel flooding in PEM fuel cells, 187 (2009) 444–451. https://doi.org/10.1016/j.jpowsour.2008.11.030.

[46]	M. Song, P. Pei, H. Zha, H. Xu, Water management of proton exchange membrane fuel cell based on control of hydrogen pressure drop, J. Power Sources. 267 (2014) 655–663. https://doi.org/10.1016/j.jpowsour.2014.05.094.

[47]	W. Schmittinger, A. Vahidi, A review of the main parameters influencing long-term performance and durability of PEM fuel cells, J. Power Sources. 180 (2008) 1–14. https://doi.org/10.1016/j.jpowsour.2008.01.070.

[48]	D. Liu, R. Lin, B. Feng, Z. Yang, Investigation of the effect of cathode stoichiometry of proton exchange membrane fuel cell using localized electrochemical impedance spectroscopy based on print circuit board, Int. J. Hydrogen Energy. (2019) 1–10. https://doi.org/10.1016/j.ijhydene.2019.01.095.

Reference

[49] M.F. Mathias, S.A. Grot, United States Patent, 2002.

[50] Y. Li, P. Pei, Z. Wu, P. Ren, X. Jia, D. Chen, Approaches to avoid flooding in association with pressure drop in proton exchange membrane fuel cells, Appl. Energy. 224 (2018) 42–51. https://doi.org/10.1016/j.apenergy.2018.04.071.

[51] P. Ren, P. Pei, Y. Li, Z. Wu, D. Chen, S. Huang, Diagnosis of water failures in proton exchange membrane fuel cell with zero-phase ohmic resistance and fixed-low-frequency impedance, Appl. Energy. 239 (2019) 785–792. https://doi.org/10.1016/j.apenergy.2019.01.235.

[52] H.P. Ma, H.M. Zhang, J. Hu, Y.H. Cai, B.L. Yi, Diagnostic tool to detect liquid water removal in the cathode channels of proton exchange membrane fuel cells, J. Power Sources. 162 (2006) 469–473. https://doi.org/10.1016/j.jpowsour.2006.06.055.

[53] W. He, G. Lin, T. Van Nguyen, Diagnostic Tool to Detect Electrode Flooding in Proton-Exchange-Membrane Fuel Cells, AIChE J. 49 (2003) 3221–3228. https://doi.org/https://doi.org/10.1002/aic.690491221.

[54] K. Jiao, J. Park, X. Li, Experimental investigations on liquid water removal from the gas diffusion layer by reactant flow in a PEM fuel cell, Appl. Energy. 87 (2010) 2770–2777. https://doi.org/10.1016/j.apenergy.2009.04.041.

[55] P. Pei, Y. Li, H. Xu, Z. Wu, A review on water fault diagnosis of PEMFC associated with the pressure drop, Appl. Energy. 173 (2016) 366–385. https://doi.org/10.1016/j.apenergy.2016.04.064.

[56] P. Pei, M. Ouyang, W. Feng, L. Lu, H. Huang, J. Zhang, Hydrogen pressure drop characteristics in a fuel cell stack, Int. J. Hydrogen Energy. 31 (2006) 371–377. https://doi.org/10.1016/j.ijhydene.2005.08.008.

[57] F. Barbir, H. Gorgun, X. Wang, Relationship between pressure drop and cell resistance as a diagnostic tool for PEM fuel cells, J. Power Sources. 141 (2005) 96–101. https://doi.org/10.1016/j.jpowsour.2004.08.055.

[58] Q.K. Dang, D. Henkensmeier, N.N. Krishnan, J.H. Jang, H. Kim, S.W. Nam, T. Lim, Nafion membranes with a porous surface, J. Memb. Sci. 460 (2014) 199–205. https://doi.org/10.1016/j.memsci.2014.03.003.

[59] T.J.P. Freire, E.R. Gonzalez, Effect of membrane characteristics and humidification conditions on the impedance response of polymer electrolyte fuel cells, J. Electroanal. Chem. 503 (2001) 57–68.

[60] S.H. Mirfarsi, M.J. Parnian, S. Rowshanzamir, Self-Humidifying Proton Exchange Membranes for Fuel Cell Applications : Advances and Challenges, Processes. 8 (2020) 1069.

[61] M. Watanabe, H. Uchida, Y. Seki, M. Emori, P. Stonehart, Self - Humidifying Polymer Electrolyte Membranes for Fuel Cells Self-Humidifying Polymer Electrolyte Membranes for Fuel Cells, J. Electrochem. Soc. 143 (1996) 3847.

[62] M. Kourasi, R.G.A. Wills, A.A. Shah, F.C. Walsh, Electrochimica Acta Heteropolyacids for fuel cell applications, Electrochim. Acta. 127 (2014) 454–466. https://doi.org/10.1016/j.electacta.2014.02.006.

[63] I. Mo, J. Won, S. Il, E. Sook, M. Soo, Experimental study on the self-humidification effect in proton exchange membrane fuel cells containing double gas diffusion backing layer, Appl. Energy. 145 (2015) 345–353. https://doi.org/10.1016/j.apenergy.2015.02.027.

[64] Z. Lu, M.M. Daino, C. Rath, S.G. Kandlikar, Water management studies in PEM fuel cells, part III: Dynamic breakthrough and intermittent drainage

characteristics from GDLs with and without MPLs, Int. J. Hydrogen Energy. 35 (2010) 4222–4233. https://doi.org/10.1016/j.ijhydene.2010.01.012.

[65]   D. Spernjak, A.K. Prasad, S.G. Advani, Experimental investigation of liquid water formation and transport in a transparent single-serpentine PEM fuel cell, J. Power Sources. 170 (2007) 334–344. https://doi.org/10.1016/j.jpowsour.2007.04.020.

[66]   J. Shi, J. Tian, C. Zhang, Z. Shan, A novel method for the preparation of a PEMFC water management layer, J. Power Sources. 164 (2007) 284–286. https://doi.org/10.1016/j.jpowsour.2006.09.095.

[67]   L. Daza, J. Soler, E. Hontan, Electrode permeability and flow-field configuration : influence on the performance of a PEMFC, J. Power Sources. 118 (2003) 172–178. https://doi.org/10.1016/S0378-7753(03)00081-8.

[68]   X. Li, I. Sabir, J. Park, A flow channel design procedure for PEM fuel cells with effective water removal, J. Power Sources. 163 (2007) 933–942. https://doi.org/10.1016/j.jpowsour.2006.10.015.

[69]   W. Yan, C. Yang, C. Soong, F. Chen, S. Mei, Experimental studies on optimal operating conditions for different flow field designs of PEM fuel cells, J. Power Sources. 160 (2006) 284–292. https://doi.org/10.1016/j.jpowsour.2006.01.031.

[70]   H. Heidary, M.J. Kermani, S.G. Advani, A.K. Prasad, Experimental investigation of in-line and staggered blockages in parallel flowfield channels of PEM fuel cells, Int. J. Hydrogen Energy. (2016) 1–9. https://doi.org/10.1016/j.ijhydene.2016.03.028.

[71]   A. Jo, S. Ahn, K. Oh, W. Kim, H. Ju, Effects of metal foam properties on flow and water distribution in polymer electrolyte fuel cells (PEFCs), Int. J. Hydrogen Energy. 43 (2018) 14034--14046. https://doi.org/10.1016/j.ijhydene.2018.01.134.

[72]   K. Lim, N. Vaz, J. Lee, H. Ju, Advantages and disadvantages of various cathode flow field designs for a polymer electrolyte membrane fuel cell, Int. J. Heat Mass Transf. 163 (2020) 120497. https://doi.org/10.1016/j.ijheatmasstransfer.2020.120497.

[73]   S. Flick, New Methodologies to Characterize PEMFC Performance Losses, University of British Columbia, 2015. https://doi.org/10.1017/CBO9781107415324.004.

[74]   U. Pasaogullari, C. Wang, K.S. Chen, Two-Phase Transport in Polymer Electrolyte Fuel Cells with Bilayer Cathode Gas Diffusion Media, J. Electrochem. Soc. 152 (2005) A1574. https://doi.org/10.1149/1.1938067.

[75]   A. Hakenjos, H. Muenter, U. Wittstadt, C. Hebling, A PEM fuel cell for combined measurement of current and temperature distribution, and flow field flooding, J. Power Sources. 131 (2004) 213–216. https://doi.org/10.1016/j.jpowsour.2003.11.081.

[76]   K. Tüber, D. Pócza, C. Hebling, Visualization of water buildup in the cathode of a transparent PEM fuel cell, J. Power Sources. 124 (2003) 403–414. https://doi.org/10.1016/S0378-7753(03)00797-3.

[77]   D. Natarajan, T. Van Nguyen, Current distribution in PEM fuel cells. Part 1: Oxygen and fuel flow rate effects, AIChE J. 51 (2005) 2587–2598. https://doi.org/10.1002/aic.10545.

[78]   F. Migliardini, T.M. Di Palma, M.F. Gaele, P. Corbo, Hydrogen purge and reactant feeding strategies in self-humidified PEM fuel cell systems, Int. J.

Hydrogen Energy. 42 (2017) 1758--1765. https://doi.org/10.1016/j.ijhydene.2016.06.196.

[79] M. Ji, Z. Wei, A review of water management in polymer electrolyte membrane fuel cells, Energies. 2 (2009) 1057–1106. https://doi.org/10.3390/en20401057.

[80] Q. Yan, H. Toghiani, J. Wu, Investigation of water transport through membrane in a PEM fuel cell by water balance experiments, J. Power Sources. 158 (2006) 316–325. https://doi.org/10.1016/j.jpowsour.2005.09.013.

[81] S. Bhatt, B. Gupta, V.K. Sethi, M. Pandey, Polymer Exchange Membrane (PEM) Fuel Cell : A Review, Int. J. Curr. Eng. Technol. 2 (2012) 219–226. https://doi.org/https://doi.org/10.1016/j.ijhydene.2010.05.017.

[82] W.L. Yu, S.J. Wu, S.W. Shiah, Parametric analysis of the proton exchange membrane fuel cell performance using design of experiments, Int. J. Hydrogen Energy. 33 (2008) 2311–2322. https://doi.org/10.1016/j.ijhydene.2008.02.040.

[83] H.H. Voss, D.P. Wilkinson, P.G. Pickup, M.C. Johnson, V. Basura, Anode water removal: A water management and diagnostic technique for solid polymer fuel cells, Electrochim. Acta. 40 (1995) 321–328. https://doi.org/https://doi.org/10.1016/0013-4686(94)00266-4.

[84] A. Mughal, X. Li, Experimental diagnostics of PEM fuel cells, Int. J. Environ. Stud. 63 (2006) 377–389. https://doi.org/10.1080/00207230600800670.

[85] E. Kimball, T. Whitaker, Y.G. Kevrekidis, J.B. Benziger, Drops, Slugs, and Flooding in Polymer Electrolyte Membrane Fuel Cells, AIChE J. 54 (2008) 1313--1332. https://doi.org/10.1002/aic.

[86] S. Chen, Y. Wu, Gravity effect on water discharged in PEM fuel cell cathode, Int. J. Hydrogen Energy. 35 (2010) 2888–2893. https://doi.org/10.1016/j.ijhydene.2009.05.111.

[87] H. Guo, X. Liu, J.F. Zhao, F. Ye, C.F. Ma, Effect of low gravity on water removal inside proton exchange membrane fuel cells (PEMFCs) with different flow channel configurations, Energy. 112 (2016) 926–934. https://doi.org/10.1016/j.energy.2016.07.006.

[88] M. Ashra, M. Shams, The effects of flow-field orientation on water management in PEM fuel cells with serpentine channels, 208 (2017) 1083–1096. https://doi.org/10.1016/j.apenergy.2017.09.044.

[89] Y. Shi, H. Janßen, W. Lehnert, A Transient Behavior Study of Polymer Electrolyte Fuel Cells with Cyclic Current Profiles, Energies. (2019) 1–13. https://doi.org/10.3390/en12122370.

[90] S. Um, C. Wang, K.S. Chen, Computational Fluid Dynamics Modeling of Proton Exchange Membrane Fuel Cells, J. Electrochem. Soc. 147 (2000) 4485–4493.

[91] W. Yan, C. Soong, F. Chen, H. Chu, Transient analysis of reactant gas transport and performance of PEM fuel cells, J. Power Sources. 143 (2005) 48–56. https://doi.org/10.1016/j.jpowsour.2004.11.058.

[92] J. Hamelin, K. Agbossou, A. Laperriâ, F. Laurencelle, T.K. Bose, Dynamic behavior of a PEM fuel cell stack for stationary applications, Int. J. Hydrogen Energy. 26 (2001) 625–629.

[93] S. Kim, S. Shimpalee, J.W. Van Zee, The effect of stoichiometry on dynamic behavior of a proton exchange membrane fuel cell (PEMFC) during load change, J. Power Sources. 135 (2004) 110–121. https://doi.org/10.1016/j.jpowsour.2004.03.060.

[94] Q. Shen, M. Hou, X. Yan, D. Liang, Z. Zang, L. Hao, Z. Shao, Z. Hou, P. Ming, B. Yi, The voltage characteristics of proton exchange membrane fuel cell (PEMFC) under steady and transient states, J. Power Sources. 179 (2008) 292–296. https://doi.org/10.1016/j.jpowsour.2007.12.049.

[95] Q. Yan, H. Toghiani, H. Causey, Steady state and dynamic performance of proton exchange membrane fuel cells (PEMFCs) under various operating conditions and load changes, J. Power Sources. 161 (2006) 492–502. https://doi.org/10.1016/j.jpowsour.2006.03.077.

[96] D. Liu, S. Case, Durability study of proton exchange membrane fuel cells under dynamic testing conditions with cyclic current profile, J. Power Sources. 162 (2006) 521–531. https://doi.org/10.1016/j.jpowsour.2006.07.007.

[97] R. Lin, B. Li, Y.P. Hou, J.M. Ma, Investigation of dynamic driving cycle effect on performance degradation and micro-structure change of PEM fuel cell, Int. J. Hydrogen Energy. 34 (2009) 2369–2376. https://doi.org/10.1016/j.ijhydene.2008.10.054.

[98] R. Lin, F. Xiong, W.C. Tang, L. Técher, J.M. Zhang, J.X. Ma, Investigation of dynamic driving cycle effect on the degradation of proton exchange membrane fuel cell by segmented cell technology, J. Power Sources. 260 (2014) 150–158. https://doi.org/10.1016/j.jpowsour.2014.03.003.

[99] R. Banerjee, S.G. Kandlikar, Two-phase flow and thermal transients in proton exchange membrane fuel cells - A critical review, Int. J. Hydrogen Energy. 40 (2015) 3990–4010. https://doi.org/10.1016/j.ijhydene.2015.01.126.

[100] R. Banerjee, S.G. Kandlikar, Experimental investigation of two-phase flow pressure drop transients in polymer electrolyte membrane fuel cell reactant channels and their impact on the cell performance, J. Power Sources. 268 (2014) 194–203. https://doi.org/10.1016/j.jpowsour.2014.05.123.

[101] R. Banerjee, S.G. Kandlikar, Two-phase pressure drop response during load transients in a PEMFC, Int. J. Hydrogen Energy. 39 (2014) 19079–19086. https://doi.org/10.1016/j.ijhydene.2014.09.102.

[102] R. Banerjee, S.G. Kandlikar, Two-phase pressure drop characteristics during low temperature transients in PEMFCs, ASME 2014. (2016) 1–6.

[103] Y. Wang, D. Fernanda, R. Diaz, K.S. Chen, Z. Wang, X.C. Adroher, Materials, technological status, and fundamentals of PEM fuel cells–A review, Mater. Today. 32 (2020) 178–203. https://doi.org/10.1016/j.mattod.2019.06.005.

[104] Y. Wang, C. Wang, Transient analysis of polymer electrolyte fuel cells, Electrochim. Acta. 50 (2005) 1307–1315. https://doi.org/10.1016/j.electacta.2004.08.022.

[105] Z. Wahid, N. Nadir, Improvement of one factor at a time through design of experiments, World Appl. Sci. J. 21 (2013) 56–61. https://doi.org/10.5829/idosi.wasj.2013.21.mae.99919.

[106] B. Wahdame, D. Candusso, X. François, F. Harel, J.M. Kauffmann, G. Coquery, Design of experiment techniques for fuel cell characterisation and development, Int. J. Hydrogen Energy. 34 (2009) 967–980. https://doi.org/10.1016/j.ijhydene.2008.10.066.

[107] M. Tanco, E. Viles, L. Pozueta, Comparing different approaches for design of experiments (DoE), Lect. Notes Electr. Eng. 39 LNEE (2009) 611–621. https://doi.org/10.1007/978-90-481-2311-7_52.

[108] J.F. Box, R.A. Fisher and the design of experiments, 1922--1926, Am. Stat. 34

Reference

(1980) 1–7.

[109] G.E. Box, K.B. Wilson, On the experimental attainment of optimum conditions, J. R. Stat. Soc. Ser. B. XIII (1951) 1–38. https://doi.org/10.1111/j.2517-6161.1951.tb00067.x.

[110] D.C. Montgomery, Design and analysis of experiments, John Wiley and sons, 2017.

[111] M.J. Anderson, P.J. Whitcomb, Chapter 3: Two-Level Factorial Design, in: DOE Simpl. Pract. Tools Eff. Exp., CRC press, 2017: pp. 37–67.

[112] Y. Rahim, Characterization of High Temperature Polymer Electrolyte Fuel Cells, RWTH AACHEN UNIVERSITY, 2018. https://doi.org/10.18154/RWTH-2018-229149.

[113] T.P. Ryan, Modern Experimental Design, John Wiley and sons, 2007.

[114] R.R. Barton, Pre-Experiment Planning for Designed Experiments : Graphical Methods, J. Qual. Technol. 29 (1997) 307–316. https://doi.org/10.1080/00224065.1997.11979772.

[115] K.Y. Ronald E. Walpole, Raymond H. Myers, Sharon L. Myers, Probability & Statistics for Engineers & Scientists, 2010.

[116] Kevin Dunn, Process Improvement Using Data, Exp. Improv. Hamilton, Ontario, Canada. Creat. Commons Attrib. 4 (2019) 325–404. http://learnche.org/Pid.

[117] P. Atanassova, P. Contact, Y.S. Csmp, D. Kountz, J. Schwartz, L. Wang, D. Fuel, D.O.E. Project, O. Reg, VII.C.5 Development of High-Performance , Low-Pt Cathodes Containing New Catalysts and Layer Structure, FY 2005 Prog. Rep. (2005) 833–837.

[118] H.S. Lee, H.J. Kim, S.G. Kim, S.H. Ahn, Evaluation of graphite composite bipolar plate for PEM (proton exchange membrane) fuel cell: Electrical,mechanical,and molding properties, J. Mater. Process. Technol. 187–188 (2007) 425–428. https://doi.org/10.1016/j.jmatprotec.2006.11.213.

[119] M.F. Torchio, M.G. Santarelli, A. Nicali, Experimental analysis of the CHP performance of a PEMFC stack by a 24 factorial design, J. Power Sources. 149 (2005) 33–43. https://doi.org/10.1016/j.jpowsour.2005.01.060.

[120] R.C. Dante, J.L. Escamilla, V. Madrigal, T. Theuss, J. De Dios Calderón, O. Solorza, R. Rivera, Fractional factorial design of experiments for PEM fuel cell performances improvement, Int. J. Hydrogen Energy. 28 (2003) 343–348. https://doi.org/10.1016/S0360-3199(02)00069-1.

[121] B. Wahdame, D. Candusso, J.M. Kauffmann, Study of gas pressure and flow rate influences on a 500 W PEM fuel cell, thanks to the experimental design methodology, J. Power Sources. 156 (2006) 92–99. https://doi.org/10.1016/j.jpowsour.2005.08.036.

[122] B. Jones, C.J. Nachtsheim, Split-plot designs: What, why, and how, J. Qual. Technol. 41 (2009) 340–361. https://doi.org/10.1080/00224065.2009.11917790.

[123] S. Flick, M. Schwager, E. McCarthy, W. Mérida, Designed experiments to characterize PEMFC material properties and performance, Appl. Energy. 129 (2014) 135–146. https://doi.org/10.1016/j.apenergy.2014.05.009.

[124] M. Mäkelä, Experimental design and response surface methodology in energy applications: A tutorial review, Energy Convers. Manag. 151 (2017) 630–640. https://doi.org/10.1016/j.enconman.2017.09.021.

[125] J.G. Carton, A.G. Olabi, Design of experiment study of the parameters that

affect performance of three flow plate configurations of a proton exchange membrane fuel cell, Energy. 35 (2010) 2796–2806. https://doi.org/10.1016/j.energy.2010.02.044.

[126] E.E. Kahveci, I. Taymaz, Experimental investigation on water and heat management in a PEM fuel cell using response surface methodology, Int. J. Hydrogen Energy. 39 (2014) 10655–10663. https://doi.org/10.1016/j.ijhydene.2014.04.195.

[127] M. Hasheminasab, M.J. Kermani, S.S. Nourazar, M.H. Khodsiani, A novel experimental based statistical study for water management in proton exchange membrane fuel cells, Appl. Energy. 264 (2020). https://doi.org/10.1016/j.apenergy.2020.114713.

[128] M. Pestrak, Y. Li, S.W. Case, D.A. Dillard, M.W. Ellis, Y.H. Lai, C.S. Gittleman, The effect of mechanical fatigue on the lifetimes of membrane electrode assemblies, J. Fuel Cell Sci. Technol. 7 (2010) 0410091–04100910. https://doi.org/10.1115/1.4000629.

[129] R. Schweiss, Benefits of Membrane Electrode Assemblies with Asymmetrical GDL Configurations for PEM Fuel Cells, Fuel Cells. 16 (2016) 100–106. https://doi.org/10.1002/fuce.201500133.

[130] C. Tötzke, G. Gaiselmann, M. Osenberg, T. Arlt, H. Markötter, A. Hilger, A. Kupsch, B.R. Möller, V. Schmidt, W. Lehnert, I. Manke, Influence of hydrophobic treatment on the structure of compressed gas diffusion layers, J. Power Sources. 324 (2016) 625–636. https://doi.org/10.1016/j.jpowsour.2016.05.118.

[131] J.H. Lin, W.H. Chen, Y.J. Su, T.H. Ko, Effect of gas diffusion layer compression on the performance in a proton exchange membrane fuel cell, Fuel. 87 (2008) 2420–2424. https://doi.org/10.1016/j.fuel.2008.03.001.

[132] S. Didari, A. Asadi, Y. Wang, T.A.L. Harris, Modeling of composite fibrous porous diffusion media, Int. J. Hydrogen Energy. 39 (2014) 9375–9386. https://doi.org/10.1016/j.ijhydene.2014.04.011.

[133] US Fuel Cell Council, Single Cell Test Protocol, 2006.

[134] Florida Solar Energy Center, Procedures For Performing PEM Single Cell Testing, Test Protoc. Cell Perform. Tests Performed Under DOE Contract. DE-FC36-06G016028. Vol. DOE\# DE-FC36-06G016028. US Dep. Energy, Arlington, Virginia. (2009).

[135] S. Cleghorn, P.S. Meas, S. Meas, Technical Data-PRIMEA Series MEAs, 2000.

[136] D. Qiu, L. Peng, X. Lai, M. Ni, W. Lehnert, Mechanical failure and mitigation strategies for the membrane in a proton exchange membrane fuel cell, Renew. Sustain. Energy Rev. 113 (2019) 109289. https://doi.org/10.1016/j.rser.2019.109289.

[137] D. Qiu, L. Peng, P. Liang, P. Yi, X. Lai, Mechanical degradation of proton exchange membrane along the MEA frame in proton exchange membrane fuel cells, Energy. 165 (2018) 210–222. https://doi.org/10.1016/j.energy.2018.09.136.

[138] D. Bograchev, M. Gueguen, J.C. Grandidier, S. Martemianov, Stress and plastic deformation of MEA in running fuel cell, Int. J. Hydrogen Energy. 33 (2008) 5703–5717. https://doi.org/10.1016/j.ijhydene.2008.06.066.

[139] X. Huang, R. Solasi, Y. Zou, M. Feshler, K. Reifsnider, D. Condit, S. Burlatsky, T. Madden, Mechanical Endurance of Polymer Electrolyte Membrane and PEM Fuel Cell Durability, J. Polym. Sci. Part B Polym. Phys. 44 (2006) 2346–2357.

https://doi.org/10.1002/polb.

[140] M. Krasij, M.J. Rajport Jr, Interfacial and edge seals for unitized electrode assemblies of fuel cell stack assembly, US Pat. No.6,743,542. 2 (2004) 20–25.

[141] Greenlight Innovation Corp., Emerald-FCATS Test Station, 2014.

[142] ISO 5725-1, Accuracy (trueness and precision) of measurement methods and results - Part 1: General principles and definitions, 1994. https://www.iso.org/obp/ui/#iso:std:iso:5725:-1:ed-1:v1:en.

[143] ISO 5725-2, Accuracy (trueness and precision) of measurement methods and results - Part 2: Basic method for the determination of repeatability and reproducibility of a standard measurement method, Switzerland, 1994. https://www.iso.org/obp/ui/#iso:std:iso:tr:22971:ed-1:v1:en.

[144] T. Luping, B. Schouenborg, Methodology of Inter-comparison Tests and Statistical Analysis of Test Results-Nordtest project No. 1483-99, SP Rapp. (2000).

[145] P.T. Wilrich, Critical values of Mandel's h and k, the Grubbs and the Cochran test statistic, AStA Adv. Stat. Anal. 97 (2013) 1–10. https://doi.org/10.1007/s10182-011-0185-y.

[146] G.B. Heyes, ASTM E691–87 Standard Practice for Conducting an Interlaboratory Study to Determine the Precision of a Test Method, J. Qual. Technol. 25 (2018) 313–314. https://doi.org/10.1080/00224065.1993.11979478.

[147] G. Box, J.S. Hunter, W. Hunter, Statistics Experimenters, John Wiley and sons, New York, 2009. https://doi.org/10.1080/00401706.1979.10489788.

[148] V. Czitrom, Guidelines for selecting factors and factor levels for an industrial designed experiment, Stat. Ind. 22 (2003) 3–32. https://doi.org/10.1016/S0169-7161(03)22003-4.

[149] S. Kaytakoğlu, L. Akyalçin, Optimization of parametric performance of a PEMFC, Int. J. Hydrogen Energy. 32 (2007) 4418–4423. https://doi.org/10.1016/j.ijhydene.2007.06.025.

[150] S.J. Wu, S.W. Shiah, W.L. Yu, Parametric analysis of proton exchange membrane fuel cell performance by using the Taguchi method and a neural network, Renew. Energy. 34 (2009) 135–144. https://doi.org/10.1016/j.renene.2008.03.006.

[151] J. Chen, Dominant frequency of pressure drop signal as a novel diagnostic tool for the water removal in proton exchange membrane fuel cell flow channel, J. Power Sources. 195 (2010) 1177–1181. https://doi.org/10.1016/j.jpowsour.2009.09.003.

[152] J. Wu, X. Zi Yuan, H. Wang, M. Blanco, J.J. Martin, J. Zhang, Diagnostic tools in PEM fuel cell research: Part II: Physical/chemical methods, Int. J. Hydrogen Energy. 33 (2008) 1747–1757. https://doi.org/https://doi.org/10.1016/j.ijhydene.2008.01.020.

[153] K. Jiao, B. Zhou, P. Quan, Liquid water transport in parallel serpentine channels with manifolds on cathode side of a PEM fuel cell stack, J. Power Sources. 154 (2006) 124–137. https://doi.org/https://doi.org/10.1016/j.jpowsour.2005.04.003.

[154] Y. Li, P. Pei, Z. Wu, H. Xu, D. Chen, S. Huang, Novel approach to determine cathode two-phase-flow pressure drop of proton exchange membrane fuel cell and its application on water management, Appl. Energy. 190 (2017) 713–724. https://doi.org/10.1016/j.apenergy.2017.01.010.

[155] Y. Tang, W. Yuan, M. Pan, Z. Li, G. Chen, Y. Li, Experimental investigation of dynamic performance and transient responses of a kW-class PEM fuel cell stack under various load changes, Appl. Energy. 87 (2010) 1410–1417. https://doi.org/10.1016/j.apenergy.2009.08.047.

[156] M. Ashrafi, M. Shams, The effects of flow-field orientation on water management in PEM fuel cells with serpentine channels, Appl. Energy. 208 (2017) 1083–1096. https://doi.org/10.1016/j.apenergy.2017.09.044.

[157] S.S. Hsieh, B.S. Her, Y.J. Huang, Effect of pressure drop in different flow fields on water accumulation and current distribution for a micro PEM fuel cell, Energy Convers. Manag. 52 (2011) 975–982. https://doi.org/10.1016/j.enconman.2010.08.025.

[158] A. Kawahara, P.Y. Chung, M. Kawaji, Investigation of two-phase flow pattern, void fraction and pressure drop in a microchannel, Int. J. Multiph. Flow. 28 (2002) 1411–1435. https://doi.org/10.1016/S0301-9322(02)00037-X.

Reference

List of Figures

List of Figures

List of Figures

List of Tables

List of Tables

Nomenclature

Abbreviations

LT-PEFC	low temperature polymer electrolyte fuel cell
Mtoe	megaton of oil equivalent
PEFC	polymer electrolyte fuel cell
CHP	combined heat and power system
AFC	Alkaline fuel cell
PAFC	Phosphoric acid fuel cell
MCFC	Molten carbonate fuel cell
SOFC	Solid oxide fuel cell
DMFC	Direct methanol fuel cell
PEM	proton exchange membrane
TPB	triple phase boundary
STP	standard temperature and pressure condition
LHV	lower heating value
HHV	higher heating value
OCV	open-circuit voltage
EOD	Electro-osmotic drag
BD	Back diffusion
TOD	thermal-osmotic drag
MPL	microporous layer
GDL	gas diffusion layer
CL	catalyst layer
HFR	High Frequency Resistance

Nomenclature

LFR		Low-frequency resistance
GDM		gas diffusion medium
MEA		membrane electrode assembly
CCM		catalyst-coated membrane
DoE		Design of Experiments
OFAT		One-Factor-at-A-Time Method
RSM		response surface methodology
ANOVA		Analysis of Variance
CCD		central composite design
BBD		Box Behnken design
PTFE		Polytetrafluorethylen
PFA		perfluoroalkoxy alkanes
R.H.		relative humidity
stoi.		stoichiometry ratio

Latin symbols

E	V	cell potential
$\Delta h_f{}^0$	kJ mol^{-1}	enthalpy change of a reaction under STP
n		moles of transferred electrons
F	96485C mol^{-1}	Faraday's constant
E_0	V	theoretical cell potential
$\Delta g_f{}^0$	kJ mol^{-1}	change in Gibbs free energy of the reaction under STP
Δs^0	kJ mol^{-1}K^{-1}	change in entropy of the reaction under STP
T	K	reaction temperature

168

R	8.314J mol^{-1}K^{-1}	universal gas constant
a_i		activity of each reactant or product, $a_i = \frac{P_i}{P^0}$
P_i	kPa	partial pressure of each reactant or product
P^0	101.325kPa	atmospheric pressure
e		experimental residual
X		design matrix
b		vector of coefficients
S_r		repeatability standard deviation
r		repeatability limit
S_R		reproducibility standard deviation
R		reproducibility limit
k_i		within-cell consistency statistics for i_{th} test cell
s_i	V	standard deviation for i_{th} test cell
h_i	V	between-cell consistency statistics for i_{th} test cell
d_i	V	deviation of the average value for i_{th} test cell
$s_{\bar{y}}$	V	standard deviation of the test cell averages
L		length of the flow channel
V_{AOM}	V	average overshoot magnitude
V_{AUM}	V	average undershoot magnitude
V_{OMi}	V	voltage overshoot magnitude of i_{th} cycle
V_{UMi}	V	voltage undershoot magnitude of i_{th} cycle
ΔP_{TopA}	mbar	top average pressure drop
ΔP_{BotA}	mbar	bottom average pressure drop

Greek symbols

σ_r^2	repeatability variance
σ_R^2	reproducibility variance
σ_W^2	within-cell variance
σ_B^2	between-cell variance
ε	model residual
λ	stoichiometry ratio

Acknowledgments

Acknowledgments

Schriften des Forschungszentrums Jülich
Reihe Energie & Umwelt / Energy & Environment

Band / Volume 553
Field assisted sintering of yttria ceramics for plasma etching applications
M. Kindelmann (2021), VI, 122, XXX pp
ISBN: 978-3-95806-579-6

Band / Volume 554
Characterisation of the effect of redox potential on the emission of greenhouse gases using wireless sensing techniques
J. Wang (2021), XIV, 104 pp
ISBN: 978-3-95806-581-9

Band / Volume 555
Stability assessment of variably saturated hillslopes using coupled hydromechanical models
S. Moradi (2021), xxxii, 123 pp
ISBN: 978-3-95806-583-3

Band / Volume 556
Catalytic-doping of Silicon Alloys for the Use in Silicon Heterojunction Solar Cells
Y. Liu (2021), 126 pp
ISBN: 978-3-95806-591-8

Band / Volume 557
Formation of highly oxygenated organic molecules from α-pinene photochemistry
S. Kang (2021), xvii, 156 pp
ISBN: 978-3-95806-596-3

Band / Volume 558
Synthese von Cr_2AlC MAX-Phasen Kompositen und Bestimmung ihrer oxidativen Eigenschaften
T. Go (2021), ii, 119 pp
ISBN: 978-3-95806-598-7

Band / Volume 559
Distribution of Relaxation Times for Analysis of Solid Oxide Fuel Cell Stacks
K. Fitzek (2021), 237 pp
ISBN: 978-3-95806-599-4

Band / Volume 560
Machine Learning in Modeling of the Dynamics of Polymer Electrolyte Fuel Cells
W. Zou (2021), vii, 139 pp
ISBN: 978-3-95806-601-4

Schriften des Forschungszentrums Jülich
Reihe Energie & Umwelt / Energy & Environment

Band / Volume 561
Introduction Strategies for Hydrogen Infrastructure
S. Cerniauskas (2021), viii, 179 pp
ISBN: 978-3-95806-602-1

Band / Volume 562
Noble Metal Coated Porous Transport Layers for Polymer Electrolyte Membrane Water Electrolysis
C. Liu (2021), 139 pp
ISBN: 978-3-95806-603-8

Band / Volume 563
Modeling and Diagnosis of the Stratospheric Circulation
E. J. Charlesworth (2021), v, 103, A2 pp
ISBN: 978-3-95806-605-2

Band / Volume 564
Potentialfeldmessungen zur Qualitätsbewertung von Bipolarplatten
M. Sietmann (2021), ix, 160 pp
ISBN: 978-3-95806-606-9

Band / Volume 565
Sequential and coupled inversion of time-lapse borehole GPR measurements for vadose zone model parameterization
Y. Yu (2022), XX, 121 pp
ISBN: 978-3-95806-607-6

Band / Volume 566
Cirrus clouds in the extratropical tropopause and lowermost stratosphere region
I. Bartolomé García (2022), iii, 155 pp
ISBN: 978-3-95806-610-6

Band / Volume 567
Stationary and Transient Behaviour of Polymer Electrolyte Fuel Cells
Y. Shi (2022), viii, 172 pp
ISBN: 978-3-95806-611-3

Weitere *Schriften des Verlags im Forschungszentrum Jülich* unter
http://wwwzb1.fz-juelich.de/verlagextern1/index.asp

JÜLICH
Forschungszentrum